Muon Neutrino Disappearance at T2K

Alexander Hyndman
Supervisor: Dr. Francesca Di Lodovico

Department of Physics,
Queen Mary,
University of London

A thesis submitted in accordance with the regulations
for the degree of Doctor of Philosophy
in the University of London

September 2011

Abstract

This thesis measures the muon neutrino oscillation at T2K using the first data of the experiment. It concentrates on developing an original selection at Super-Kamionde, the T2K far detector, that improves the performance of the current standard selection. A new, more precise measurement of the oscillation parameters $\sin^2 2\theta_{23}$ and Δm^2_{32} is performed using this new selection.

T2K is a long-baseline neutrino oscillation experiment located in Japan which began data taking in January 2010. It uses the world's most powerful accelerator generated beam of muon neutrinos intersected by two detectors. The near detector is located 280 m from the beam source while Super-Kamiokande lies 295 km away.

Super-Kamiokande is a 50 kt water Cherenkov detector which measures the neutrino beam after oscillation. The determination of the oscillation parameters comes from looking at the disappearance of muon neutrinos from the beam. For this purpose event selection at Super-Kamiokande is optimised for neutrino flavour identification and energy reconstruction, specifically, selecting muon neutrino charged-current quasi-elastic events, primarily with single muon-like Cherenkov rings produced by the outgoing muon. This thesis evaluates two new methods of enhancing the selection to obtain a higher sensitivity from the data, firstly by exploring a multi-variate analysis approach to charged-current quasi-elastic selection, and secondly through the exploration of an additional charged-current single charged pion channel. Out of these only the multivariate based selection produced an improvement in the sensitivity to oscillation with respect to the standard selection.

A first analysis of the data collected until March 11$^{\text{th}}$ 2011 using the above described improvement is presented in this thesis. A value of $2.68^{+0.12}_{-0.18} \times 10^{-3}$ eV^2 was recorded for Δm^2_{32} and $0.999^{+0.001}_{-0.009}$ for $\sin^2 2\theta_{23}$.

Acknowledgements

I would like to thank my supervisor Francesca and all those that have helped and supported me at Queen Mary and in the T2K collaboration. Special thanks to Ryan Terri whose guidance and wisdom has been invaluable.

Contents

List of Figures

List of Tables

Chapter 1

Introduction

Of all the known elementary particles neutrinos are thought to be the most abundant in the universe, yet relatively little is known about them. Predicted by the Standard Model of particle physics to be massless, left-handed and observable in three forms (electron, muon and tau), over the last few decades it has been shown that neutrinos do not only have masses, albeit very small, but are capable of oscillating between the three constituent flavour states controlled by a set of oscillation parameters. The T2K experiment is the first in a new generation of neutrino beam based experiments designed to precisely measure these parameters.

The T2K experiment operates by looking for an energy dependent change in the flavour composition of a muon-neutrino beam over a distance of 295 km. It is the role of the far detector, Super-Kamiokande, to measure the flavour composition of the beam at this distance from the source and thus determine the oscillation. This thesis is concerned with the measurement of the oscillation parameters θ_{23} and Δm^2_{32} using the first data collected by T2K. The study presented here assesses two principal proposed enhancements to the way detected neutrino interactions are selected at Super-Kamiokande, with the intention of improving the sensitivity of the experiment to the oscillation driven by these two parameters, both in the near term running of the experiment as well as for the longer term.

Chapter 2 provides a brief history of the study of neutrinos and an overview of the physics of neutrino flavour oscillations and the interactions with matter that underlie the principles of neutrino detection. Chapter 3 is a summary of the experimental set-up of the T2K experiment with particular emphasis given to Super-Kamiokande, the detector which is the focus of this study. Chapter 4 covers the Monte Carlo simulation of the neutrino interactions at Super-Kamiokande and the expected detector response needed for optimisation of the analysis techniques and the analysis of the data itself. The collection and preliminary processing of data up to March 2011 is also discussed in this chapter. In chapter 5 the selection of neutrino interaction events at Super-Kamiokande used for the oscillation analysis are discussed as well as two proposed enhancements to the selection. In chapter 6 data up to March 2011 is examined in preparation for use with the chosen selections in the oscillation analysis which is presented in the second part of the chapter. A summary and conclusions are given in chapter 7.

Chapter 2

Neutrino Physics

The neutrino is a chargeless, spin 1/2 elementary particle. Denoted by the Greek symbol ν it comes in three flavours mirroring those of the charged leptons: electron neutrino (ν_e), muon neutrino (ν_μ) and tau neutrino (ν_τ). Their masses are at least 250,000 lighter than the electron mass and they are thought to be the most abundant particle in the universe being produced in vast quantities in stellar nuclear reactions.

This chapter begins with a brief history of the discovery of the neutrino and the experimental and theoretical progress made during the last century. Neutrino interactions with matter and the theory behind neutrino oscillations are then summarised. Finally the experimental approach to measuring the oscillation parameters θ_{23} and Δm^2_{32} is discussed in relation to long-baseline accelerator experiments.

2.1 A Brief History of Neutrino Physics

The history of the neutrino begins with its inception by Wolfgang Pauli in 1930 as a means to account for missing energy in β-decay [1]. Pauli proposed that in order to maintain energy conservation an additional neutral particle must be produced with the existing outgoing electron to carry away the remaining unobserved energy. Enrico Fermi worked Pauli's ideas into his model of β-decay [2]. However, calculations by Hans Bethe and Rudolf Peierls showed that the interaction cross section of the neutrino would be very low [3]. It was not until 22 years later in 1956 that the existence of the neutrino was experimentally verified by Fred Reines and Clyde Cowan, when they detected electron anti-neutrinos from a nuclear reactor at the Savannah River Plant [4]. The following year, Goldhaber *et al.* experimentally showed that neutrinos must have negative helicity (left-handed) [5].

The next important step in the history of neutrino physics was the confirmation of multi-flavours of neutrinos, which occurred with the discovery of the muon neutrino in 1962 by Lederman *et al.* at the Brookhaven National Laboratories [6]. In 1976 a group led by Martin Perl discovered the tau lepton at the Stanford Linear Accelerator Center [7]. The implication was a matching third generation neutrino, however it was not until 2000 that the tau neutrino was directly observed with the DONUT experiment at the Fermi National Accelerator Laboratory (FNAL) [8].

Naturally occurring neutrinos were observed for the first time in 1965 by Reines when he detected neutrinos produced by cosmic rays in the atmosphere in an experiment located in the Johannesburg gold mine, South Africa [9]. Around that time Ray Davis also set up his famous underground experiment to look for naturally produced neutrinos, this time from the Sun. The Homestake experiment was the first to show an apparent deficit in the number of solar neutrinos reaching the Earth compared to flux calculations done by theorist John Bahcall [10]. This deficit was later observed by SAGE [11], GALLEX [12] and the Kamiokande [13] experiments. In 1992 the Kamiokande experiment along with the IMB also observed an anomalous ratio in the flavour of atmospheric neutrinos [14] [15]. These experiments suggested that neutrino flavour changes could occur. Second generation experiments, in particular the Sudbury Neutrino Observatory (SNO) and Super-Kamiokande confirmed neutrino oscillations by measuring the flux from multiple neutrino flavours [16][17]. These confirmed Bahcall's prediction for the total solar flux and led to Maki, Nakagawa and Sakata's 1962 theory on neutrino vacuum oscillations [18] being accepted as the standard explanation of neutrino oscillations with the addition of the MSW effect (named after Mikheev, Smirnov and Wolfenstein) to account for the effects of matter on the oscillation [19][20].

In the years following this discovery, a number of experiments began to measure the mixing between the different flavours of neutrino using artificial neutrino sources. There were two main classes of experiment: firstly experiments using anti-neutrinos produced in nuclear reactors such as KamLAND which showed a depletion in neutrino flux dependent on distance from the reactor and neutrino energy, characteristic of neutrino oscillations [21], and secondly, experiments using a beam of neutrinos such as MINOS which measured the oscillation of muon neutrinos into tau neutrinos [22].

Beyond oscillation experiments other properties of neutrinos were explored and continue to be so with different forms of experiment. With the discovery of oscillation came the implication that neutrinos were massive. Experiments are being performed to probe the absolute magnitude of these neutrino masses, such experiments include KATRIN in Germany [23]. Another major branch of the field is the many neutrinoless double β-decay experiments which aim to determine whether neutrinos are their own anti-particle (Majorana particles) by searching for these rare signature processes [24]. These experiments can also provide insight into the neutrino masses.

2.2 Neutrino Interactions with Matter

Neutrinos interact via the weak force. It is through these interactions that neutrinos can be detected. The propagators of these interactions are the $W^{\pm}$ and Z bosons. Interactions mediated by $W^{\pm}$ are consequently referred to as charged current (CC) interactions while for the Z, neutral current (NC) interactions. Because neutrinos only interact via the weak force (and to an insignificant amount via gravity) their interaction cross-section is very low, although it increases dramatically with energy.

Charged current nucleon-scattering is broadly categorised into three types. The transition between these types is controlled by the amount of momentum transfer, Q^2. At lower energies, the charged-current quasi-elastic (CCQE) process dominates, defined as

$$\nu_l + n \rightarrow p + l^-, \tag{2.1}$$

where ν_l is the incoming neutrino, n a neutron, p a proton and l an outgoing lepton. Crucially here, the outgoing lepton is of the same flavour as the incoming neutrino. For T2K neutrinos at Super-Kamiokande this is essentially limited to electrons and muons due to insufficient energy for tau production which has a threshold of ~ 3.5 GeV [25].

As energy increases further, it becomes possible for the W boson to exchange enough momentum so that the target nucleon briefly exists in an excited resonant baryon state before prompt decay into usually a nucleon and pion final state. The lowest mass baryons relevant to this process are the $\Delta(1232)$ resonances whose common decay products are as follows:

$$\Delta^{++} \rightarrow p + \pi^{+}, \tag{2.2}$$

$$\Delta^{+} \rightarrow n + \pi^{+}, p + \pi^{0}, \tag{2.3}$$

$$\Delta^{0} \rightarrow n + \pi^{0}, p + \pi^{-}. \tag{2.4}$$

Interactions which result in a single positively charged pion (π^{+}) are known as CC1π^{+}. Final states with more pions can be produced with higher energy resonances. Resonant pion production becomes dominant at around 1.1 GeV.

The third main type of interaction occurs when the momentum transfer is sufficient to break up the nucleus forming hadronic showers via a process known as deep inelastic scattering (DIS) where the neutrino interacts directly with the quark substructure of the nucleon. This process becomes dominant at around 1.2 GeV and is the exclusive mechanism for neutrino interaction by 10 GeV.

For neutral current processes no charge is exchanged, with lepton number being conserved by a same flavour neutrino in the final state. Consequently no flavour information can be determined from the interaction. At lower energies just energy and momentum can be transferred to the nucleon, however resonance pion production becomes possible with increasing energy.

2.3 Neutrino Oscillations

The following is a summary of the currently accepted theory of neutrino oscillations developed from the original ideas of Maki, Nakagawa and Sakata [18] and Pontecorvo [26].

Neutrino oscillation is a quantum mechanical phenomenon which occurs due to a mismatch between the three neutrino flavour eigenstates $|\nu_e\rangle, |\nu_\mu\rangle$

and $|\nu_\tau\rangle$ and the three mass eigenstates $|\nu_1\rangle, |\nu_2\rangle$ and $|\nu_3\rangle$. When a neutrino is created via a weak interaction it is in a pure flavour state composed of a corresponding specific linear superposition of mass states. The mass states propagate at different speeds, thus with time the composition changes and consequently the neutrino exists as a superposition of different flavour states.

The relationship between flavour states and mass states is defined by the Maki-Nakagawa-Sakata (MNS) matrix sometimes referred to as the Pontecorvo-Maki-Nakagawa-Sakata (PMNS) matrix, whose elements are fixed by nature. The matrix is a 3 × 3 unitary matrix such that

$$|\nu_\alpha\rangle = \sum_i U^*_{\alpha i} |\nu_i\rangle \tag{2.5}$$

$$|\nu_i\rangle = \sum_\alpha U_{\alpha i} |\nu_\alpha\rangle \tag{2.6}$$

where α corresponds to the flavour states (e, μ, τ), i to the mass states $(1, 2, 3)$ and U the MNS matrix which is written as follows:

$$U = \begin{bmatrix} U_{e1} & U_{e2} & U_{e3} \\ U_{\mu 1} & U_{\mu 2} & U_{\mu 3} \\ U_{\tau 1} & U_{\tau 2} & U_{\tau 3} \end{bmatrix} \tag{2.7}$$

U^* is its complex conjugate. The MNS matrix can be parametrised in the following way:

$$U = \begin{bmatrix} 1 & 0 & 0 \\ 0 & c_{23} & s_{23} \\ 0 & -s_{23} & c_{23} \end{bmatrix} \times \begin{bmatrix} c_{13} & 0 & s_{13}e^{-i\delta} \\ 0 & 1 & 0 \\ -s_{13}e^{i\delta} & 0 & c_{13} \end{bmatrix} \times \begin{bmatrix} c_{12} & s_{12} & 0 \\ -s_{12} & c_{12} & 0 \\ 0 & 0 & 1 \end{bmatrix} \tag{2.8}$$

where c_{ij} and s_{ij} stand for $\cos\theta_{ij}$ and $\sin\theta_{ij}$ and δ is a CP violating phase. θ_{ij} is known as the mixing angle [27]. It can be expanded as follows:

$$U = \begin{bmatrix} c_{12}c_{13} & s_{12}c_{13} & s_{13}e^{-i\delta} \\ -s_{12}c_{23} - c_{12}s_{23}s_{13}e^{i\delta} & c_{12}c_{23} - s_{12}s_{23}s_{13}e^{i\delta} & s_{23}c_{13} \\ s_{12}s_{23} - c_{12}c_{23}s_{13}e^{i\delta} & -c_{12}s_{23} - s_{12}c_{23}s_{13}e^{i\delta} & c_{23}c_{13} \end{bmatrix} \tag{2.9}$$

Emission, propagation, and absorption of neutrinos should be treated as a single coherent quantum-mechanical process [28][29], however a description of oscillation can be achieved using a plane wave derivation where the neutrino is localised in space and travelling at a fixed velocity.

The plane wave derivation of neutrino oscillations begins with the application of the time-dependent Schrödinger equation to each mass state, such that, from equation 2.5

$$|\nu_\alpha(t)\rangle = \sum_i e^{-iE_i t} U^*_{\alpha i} |\nu_i(0)\rangle \tag{2.10}$$

where E_i is the energy and t is the time in the lab frame, using natural units (c and $\hbar = 1$) and under the assumption that all the mass components have the same momentum $\vec{p}$. Substituting equation 2.6 into the above gives the following expression of $|\nu_\alpha(t)\rangle$ represented as a superposition of different flavour states:

$$|\nu_\alpha(t)\rangle = \sum_\beta \left(\sum_i U^*_{\alpha i} e^{-iE_i t} U_{\beta i} \right) |\nu_\beta\rangle \tag{2.11}$$

where $\beta = e, \mu, \tau$. The coefficient of $|\nu_\beta\rangle$ is the amplitude of the transition $\nu_\alpha \rightarrow \nu_\beta$ as a function of time. The transition probability can be calculated from it as follows:

$$\begin{aligned} P_{\nu_\alpha \rightarrow \nu\beta}(t) = |A_{\nu_\alpha \rightarrow \nu\beta}|^2 &= \left| \sum_i U^*_{\alpha i} U_{\beta i} e^{-iE_i t} \right|^2 && (2.12) \\ &= \sum_{i,j} U_{\alpha i} U^*_{\beta j} U^*_{\alpha j} U_{\beta i} e^{-i(E_i - E_j)t} && (2.13) \end{aligned}$$

Because neutrinos are ultrarelativistic, the above can be simplified using the following approximations:

$$\begin{aligned} t &\approx L && (2.14) \\ E_i &\approx E + \frac{m_i^2}{2E} && (2.15) \end{aligned}$$

where L is the distance from the source and $E = |\vec{p}|$, such that

$$E_i - E_j \approx \frac{\Delta m^2_{ij}}{2E} \tag{2.16}$$

where the mass-squared difference term Δm_{ij}^2 is used in place of $m_i^2 - m_j^2$. Equation 2.13 now becomes

$$P_{\nu_\alpha \to \nu_\beta}(t) = \sum_{i,j} U_{\alpha i}^* U_{\beta i} U_{\alpha j} U_{\beta j}^* e^{-i\frac{\Delta m_{ij}^2 L}{2E}}. \tag{2.17}$$

This gives the probability of one flavour of neutrino ($|\nu_\alpha\rangle$) oscillating into another ($|\nu_\beta\rangle$) as a function of energy (E) and distance (L). The mass-squared difference terms (Δm_{ij}^2) control the phase of the oscillation while the elements of the mixing matrix U control the oscillation amplitude. This derivation however assumes only oscillations in a vacuum. The index of refraction for neutrinos in matter is not constant across all the flavours. For electron neutrinos there is an additional forward coherent scattering component coming from electrons, which is not applicable to muon and tau neutrinos. This effect is known as the MSW effect after Mikheev, Smirnov and Wolfenstein [19][20]. Matter effects are included in the oscillation probability equation (2.17) by the replacement of the mass-squared term Δm^2 and mixing angle θ in the mixing matrix U with an effective mass-squared term Δm_M^2 and an effective angle θ_M, where

$$\Delta m_M^2 = \Delta m^2 \sqrt{\sin^2 2\theta + (\cos 2\theta - \epsilon)^2} \tag{2.18}$$

$$\sin^2 2\theta_M^2 = \frac{\sin^2 2\theta}{\sin^2 2\theta + (\cos 2\theta - \epsilon)^2} \tag{2.19}$$

ϵ is a measure of the importance of the matter effects. It is defined as

$$\epsilon = \frac{2\sqrt{2} G_F N_e E}{\Delta m^2} \tag{2.20}$$

where N_e is the electron density of the matter and G_F is the Fermi coupling constant. However this effect is only significant over long distances and when N_e is high, for example for solar neutrinos. The effect over the 295 km baseline of the T2K experiment is negligible.

A large variety of experiments have been used to measure the oscillation parameters. This is in part due to the large differences in magnitude of the parameters which means that no single experiment can precisely determine them all. Instead, experiments tend to focus on sets of parameters. The

Parameters	Best Fit	3σ Range
$\Delta m^2_{21}[10^{-5}\text{eV}^2]$	$7.59^{+0.23}_{-0.18}$	7.03-8.27
$\lvert\Delta m^2_{31}\rvert\,[10^{-3}\text{eV}^2]$	$2.40^{+0.12}_{-0.11}$	2.07-2.75
$\sin^2\theta_{12}$	$0.318^{+0.019}_{-0.016}$	0.27-0.38
$\sin^2\theta_{23}$	$0.50^{+0.07}_{-0.06}$	0.36-0.67
$\sin^2\theta_{13}$	$0.013^{+0.013}_{-0.009}$	≤ 0.053

Table 2.1: *Best-fit values with 1σ errors and 3σ intervals for three-flavour neutrino oscillation parameters from global data including solar, atmospheric, reactor (KamLAND and CHOOZ) and accelerator (K2K and MINOS) experiments as of February '10 from study by Schwetz* et al. *[30].*

results of a study by Schwetz *et al.* [30] to produce the best fit values for the oscillation parameters using global experimental data are shown in table 2.1.

Missing from the list is the CP violating phase δ which has not been experimentally determined. In addition, given the current level of precision and that $\sin^2\theta_{13}$ is much smaller, Δm^2_{32} and Δm^2_{31} can be considered to have the same value. The sign of Δm^2_{31} is also unknown. A negative sign would indicate that $m_1 > m_3$. This situation is referred to as the inverted mass hierarchy. However, the sign of Δm^2_{31} does not affect the vacuum oscillation probability and only becomes apparent with the inclusion of matter effects.

2.4 Principles of Fixed-Baseline Accelerator Neutrino Oscillation Experiments

The goal of neutrino oscillation experiments is to test the theoretical model for oscillation and measure the seven parameters which control the phenomenon. The fixed baseline experiments approach this problem by fixing the oscillation distance (L in equation 2.17) and having as their free parameter the neutrino energy (E). By looking over a range of energies a fit can be made for the set of oscillation parameters to which the experiment is sensitive.

A fixed-baseline experiment usually consists of the following arrangement: a beam which produces the neutrinos and a neutrino detector to measure the oscillation over the fixed baseline. The detector is sensitive to both neutrino energy and flavour. A change in flavour specific flux relative to total neutrino flux is measured as a function of energy over the baseline of the experiment to give the values of the oscillation parameters.

The term long-baseline is attached to beam based experiments that have a baseline between 100 and 1000 km. These experiments use a muon neutrino beam as their source and are classified into two types: appearance and disappearance experiments. Appearance experiments measure a probability of oscillation from one flavour to another by directly observing the new flavour while disappearance experiments measure the survival probability of one flavour of neutrino. Long-baseline experiments often add an additional detector close to the beam which characterises the outgoing neutrino flux and can also be used to provide additional supporting measurements such as cross sections. Before T2K, there were two previous long baseline experiments: K2K where the beam was produced at the KEK labs in Japan and sent to the same far detector as T2K, Super-Kamiokande, and MINOS where a beam from Fermilab in the USA was sent to a far detector in Minnesota. Both of these experiments were primarily disappearance searches looking for an oscillation caused muon neutrino deficit in their far detector. OPERA in the Gran Sasso Laboratories is a currently running tau neutrino appearance experiment using a beam from CERN.

The choice of baseline is governed primarily by physics, though political, geographical and financial constraints may also have to be considered. In terms of measuring Δm^2_{32}, θ_{23} or θ_{13} it is often desirable to have the L/E peak of the experiment coincide with an oscillation maximum to provide high statistics in the region of interest, though a broad-band beam covering two oscillation maxima can be used if energy resolution is sufficiently good. There are constraints on the usable neutrino energy range derived from the need for accurate flavour tagging, energy reconstruction and a high interaction cross-section. For muon and electron neutrinos CCQE interactions offer the best energy reconstruction due to two body kinematics and the outgoing lepton can be used to tag flavour, as discussed in section 2.2. The total neutrino interaction cross-section also peaks in the CCQE dominated region. Therefore, for a T2K like experiment, the optimum energy region is around 1 GeV. Given the value of Δm^2_{13} in table 2.1 (*N.B.* $\Delta m^2_{13} \approx \Delta m^2_{32}$) this puts the optimum baseline at around 500 km for the first oscillation maximum.

It is desirable for the beam of such experiments to be as pure in flavour as possible. Accelerator based experiments almost always use a muon neutrino beam generated primarily from the decay of pions in flight. The pions come from accelerated protons colliding with a fixed target (usually carbon) and are focused into a decay volume via magnetic focusing horns. Kaons are also produced in these collisions and their decay results in a small electron neutrino background.

For the neutrino detectors there are three main requirements: to be able to identify the flavour of an interacted neutrino, to be able to reconstruct its energy and to capture a large number of these interactions. For this last criterion a large density and volume are required. In addition these large detectors are usually located deep underground to reduce background interactions coming from cosmic rays.

2.5 Muon Neutrino Disappearance Measurement

A muon neutrino disappearance measurement refers to a reduction in expected muon neutrino flux, in the case of fixed-baseline experiments, coming from the beam source. Under the standard theory of neutrino oscillation this L/E dependent disappearance is controlled predominantly by the mixing parameters θ_{23} and Δm^2_{32}. Because $\Delta m^2_{32} \gg \Delta m^2_{21}$, it is possible to ignore the ν_e component and treat the short range oscillation as a two flavour problem. In such a case the mixing matrix U becomes

$$U = \begin{bmatrix} \cos\theta & \sin\theta \\ -\sin\theta & \cos\theta \end{bmatrix} \tag{2.21}$$

and using equation 2.17 the oscillation probability becomes

$$P(\nu_\mu \rightarrow \nu_\tau) = \sin^2 2\theta \sin^2\left(\frac{\Delta m^2 L}{2E}\right). \tag{2.22}$$

From an experimental viewpoint it is more convenient to work in units of eV^2 for the mass difference term and GeV and km for the neutrino energy and oscillation distance respectively. The oscillation probability is then expressed as follows:

$$P(\nu_\mu \to \nu_\tau) = \sin^2 2\theta \sin^2 \left(\frac{1.27 \Delta m^2 (\mathrm{eV}^2) L(\mathrm{km})}{E(\mathrm{GeV})} \right) \tag{2.23}$$

This is the equation that is commonly used in the analysis of muon neutrino disappearance.

The earliest measurements of θ_{23} and Δm^2_{32} came from atmospheric neutrinos recorded by Super-Kamiokande, where the deficit of muon neutrinos compared to electron neutrinos coming from cosmic-ray interactions in the Earth's atmosphere, known as the atmospheric neutrino problem, allowed the parameters to be measured for a large range of L/E values. The analysis of atmospheric neutrinos contributes to precise global fits of the parameters.

The first accelerator based measurement came from K2K which ran from June 1999 to November 2004. However its results have been largely superseded by the MINOS experiment which began neutrino beam running in February 2005 with the benefit of a greater neutrino flux. The latest measurement from the MINOS collaboration gives Δm^2_{32} a value of $(2.32^{+0.12}_{-0.08}) \times 10^{-3}$ eV^2 and $\sin^2 2\theta_{23}$ a value greater than 0.90 at the 90% confidence limit [31]. These fit results are shown in figure 2.1 which also shows the confidence interval contours and the results from the Super-Kamiokande atmospheric analyses.

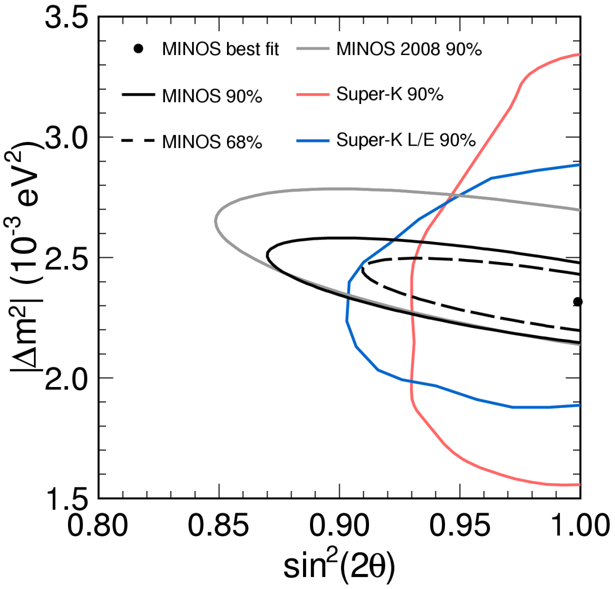

Figure 2.1: *ν_μ disappearance oscillation parameter measurement confidence interval contours for MINOS and Super-Kamiokande atmospheric neutrino analyses as of March 2011 [31].*

Chapter 3

The T2K Experiment

T2K (Tokai to Kamioka) is a second generation long baseline neutrino oscillation experiment with the purpose of investigating the mixing of muon neutrinos with the other neutrino species. It is both an appearance and a disappearance experiment, the principal goal of which is to measure the appearance of electron neutrinos ($\nu_\mu \to \nu_e$) and the associated mixing parameter θ_{13}. A secondary physics goal is the precise measurement of muon neutrino disappearance ($\nu_\mu \to \nu_\tau$) and the parameters θ_{23} and Δm^2_{32}, which is possible during the lower intensity running of the first few years. This chapter provides a technical overview of the experiment. Unless otherwise stated all information reported comes from the official T2K experiment description [32].

T2K has a baseline of 295 km and a peak neutrino energy of around 0.6 GeV giving it an L/E value of 492 km/GeV. It is therefore placed in the desirable CCQE dominated interaction region and at the first oscillation minimum for muon neutrino disappearance, hence maximizing sensitivity to the associated oscillation parameters.

Like its first generation predecessors MINOS and K2K, T2K uses a conventional muon neutrino beam and both a near and far detector. T2K, however, makes two key improvements compared to its predecessors. The first is simply a large increase in the intensity of the muon neutrino beam, made possible by a new high-power proton storage ring. This higher statistics running is required to improve on the current sensitivity of θ_{13} in a 5 year time scale. The second is that the angle between the far detector and the beam axis is set at 2.5 degrees. This off-axis alignment has the advantage of increasing the purity of the muon neutrino beam and also narrowing the energy spectrum as shown in figure 3.1. The narrower energy spectrum provides a reduced high energy tail which is the source of background processes that can cloud the signal, particularly for the electron neutrino appearance search.

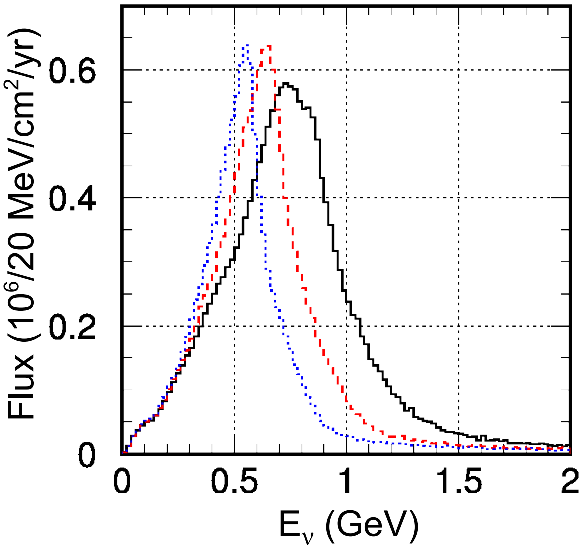

Figure 3.1: *Beam energy spectra for different off-axis angles: black-solid line is 2 degrees, red-dashed line is 2.5 degrees, and blue-dotted line is 3 degrees. As the off-axis angle increases, the energy peak narrows and moves lower in energy [33].*

T2K is a Japanese based experiment (figure 3.2). The neutrino beam source and the near detectors are situated in the coastal village of Tokai at the KEK and JAEA joint managed J-PARC (Japanese Proton Accelerator Research Centre) facility, north east of Tokyo in the Ibaraki Prefecture. The far detector, Super-Kamiokande, is located in the Kamioka mine situated in the Gifu prefecture near the town of Kamioka. The collaboration currently has around 500 members from 59 institutes and 12 countries.

The experiment was first proposed in 2003 and construction began for the beam line in 2004. Commissioning of the beam and the near detectors started in 2009 with first physics data in January 2010. Super-Kamiokande began operations in 1996, but was upgraded in 2003 to 2004. Stable running has continued since then, apart from an electronics upgrade in 2008. The

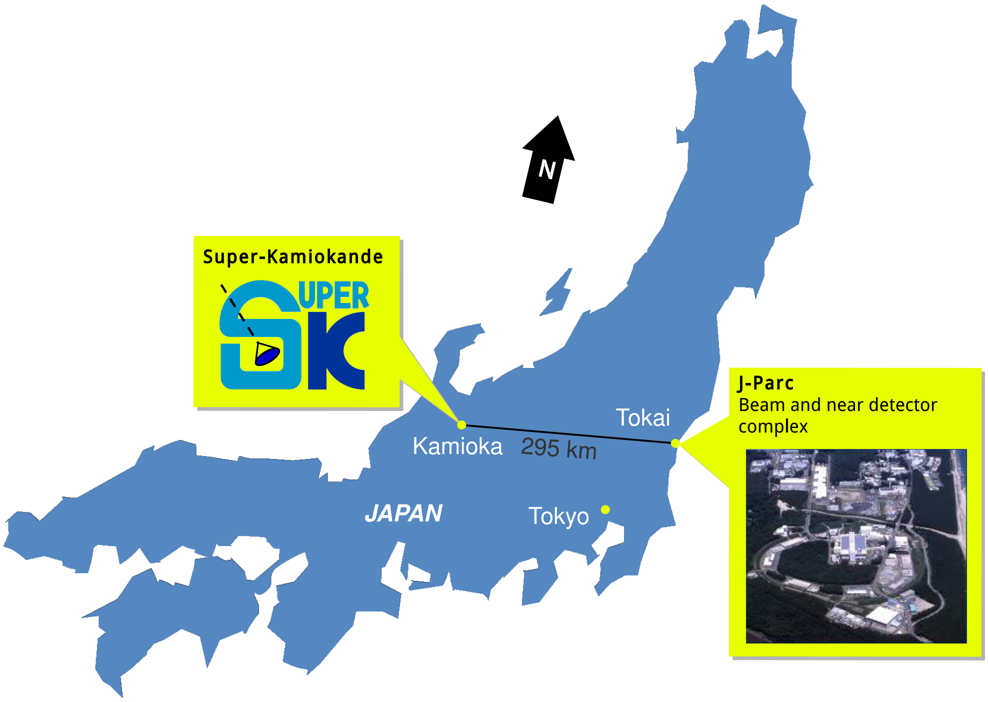

Figure 3.2: *Map of Japan showing the location of the two sites used in the T2K experiment. A baseline of 295 km separates them.*

first phase of T2K will last a nominal five years with an intended precision of $10^{-4}\,\mathrm{eV}^2$ for Δm^2_{23}, 0.01 for $\sin^2 2\theta_{23}$ and with a twenty fold increase in sensitivity on the current best limit of θ_{13} (from the CHOOZ experiment).

3.1 The Neutrino Beam

The T2K neutrino beam is predominantly composed of muon neutrinos produced from the decay of pions in flight. These are in turn produced by the collision of accelerated protons with a carbon target.

Three accelerators located in the J-PARC complex provide the protons that are extracted for collision with the carbon target. The first, a linear accelerator (LINAC), accelerates an H^- beam which is then converted to a proton beam before entering a rapid-cycling synchrotron (RCS). About 5% of the protons are then injected into the main ring (MR) where they reach 30 GeV at $\sim$ 0.3 Hz (as of 2010) in spills of eight bunches. Prior to June 2010 spills contained six bunches. The bunches are then fast extracted for the neutrino beamline in a single turn by a set of kicker magnets.

The neutrino beamline is divided into two parts (figure 3.3). The primary beamline accepts protons from the MR and directs them in an approximately westerly direction towards the Super-Kamiokande detector with an angle of 3.64 degrees with respect to the horizontal. At the start of the secondary neutrino beamline, the protons are focused onto a graphite target, a 91.4 cm long, 2.6 cm diameter rod. Protons impinge on the target in spills of around 5 μs in width and in bunches of a few nanoseconds. Hadronic interactions of the protons on carbon produce showers of charged pions with a minor contamination of kaons. These mesons are focussed into a beam by three magnetic horns, the first of which encases the target station. The negative polarity of the horns selects the π^+ components and projects them into a 96 m decay tunnel where they decay by $\pi^+ \rightarrow \mu^+\nu_\mu$ ($>$ 99% of the time). The high momentum of the accelerated pions boosts the decay, and consequently the muon neutrinos, in the beam direction. To reduce nuclear absorption of the pions, the entire secondary beamline is enclosed in helium gas at 1 atm. Positioned at the end of the decay volume is a 75 t graphite and iron beam dump which absorbs all particles except neutrinos and muons above a momentum threshold of 5

GeV/c. These muons are produced in the two body decay of the pions along with the neutrinos and can be used to measure the beam intensity and direction. They are detected by the Muon Monitor (MuMon) which lies behind the beam dump and consists of two types of detector arrays: a set of ionization chambers and a set of silicon PIN photodiodes. Information about the muons is compared to the beam simulation code JNUBEAM (see section 4.1) to infer the neutrino beam properties. The muon monitor was designed to measure the neutrino beam direction with a precision < 0.25 mrad and the bunch stability of the beam intensity to better than 3%.

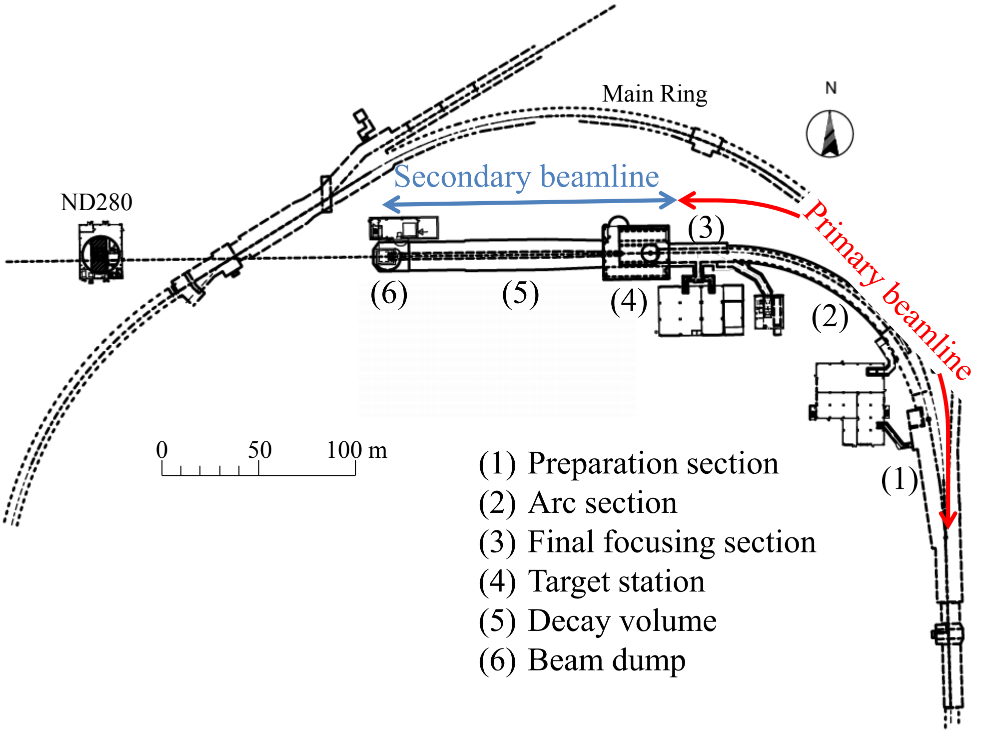

Figure 3.3: *Schematic of the primary and secondary beamlines from above. The near detector complex is marked on the left at a distance of 280 m from the target station [32].*

The neutrino beamline produces a beam of muon neutrinos with a purity greater than 99%. There is a small contamination from muon anti-neutrinos from π^- decays and electron neutrinos from kaons. The angle of the beam with respect to Super-Kamiokande is tunable in the range of about 2 to 2.5

degrees. To maximise sensitivity to the oscillation, the beam is set to an angle of 2.515 ± 0.040 degrees.

3.2 Time Synchronisation

Time synchronisation between JPARC and Super-Kamiokande is required to align the trigger window used by the detector with the beam spills created at JPARC and is achieved with the use of a GPS system.

Both sites use the same arrangement which consists of a custom electronics board (local time clock) which uses as its time base a commercial rubidium clock. This is then referenced to GPS time using input from two commercial GPS receivers. This system provides synchronisation between the two sites on the order of around 50 ns.

3.3 The Near Detector Complex

The near detector complex of T2K (figure 3.4) sits around 280 m from the target station in a 19 m diameter pit and consists of two detectors: INGRID (Interactive Neutrino GRID) and ND280 (Near Detector 280 m). INGRID lies directly on the axis of the beam while ND280 is positioned 2.5 degrees off-axis, between the target station and Super-Kamiokande. Together the detectors measure the energy spectrum, flavour content and interaction rates of the unoscillated neutrino beam which is used to more accurately predict the neutrino interactions at Super-Kamiokande.

3.3.1 INGRID

The INGRID detector lies on the beam axis with the purpose of directly monitoring the neutrino beam direction and intensity via neutrino interactions in iron. This complements the bunch-by-bunch monitoring of the hadron beam by the MuMon detector and measurements of the proton beam axis.

INGRID is formed from sixteen identical modules each around 1.3 m square and made up of 7.1 t of sandwiched iron and scintillator. The INGRID modules are arranged in a horizontal line of seven modules and a vertical line of seven modules forming a transverse cross with respect to the beam, with the two

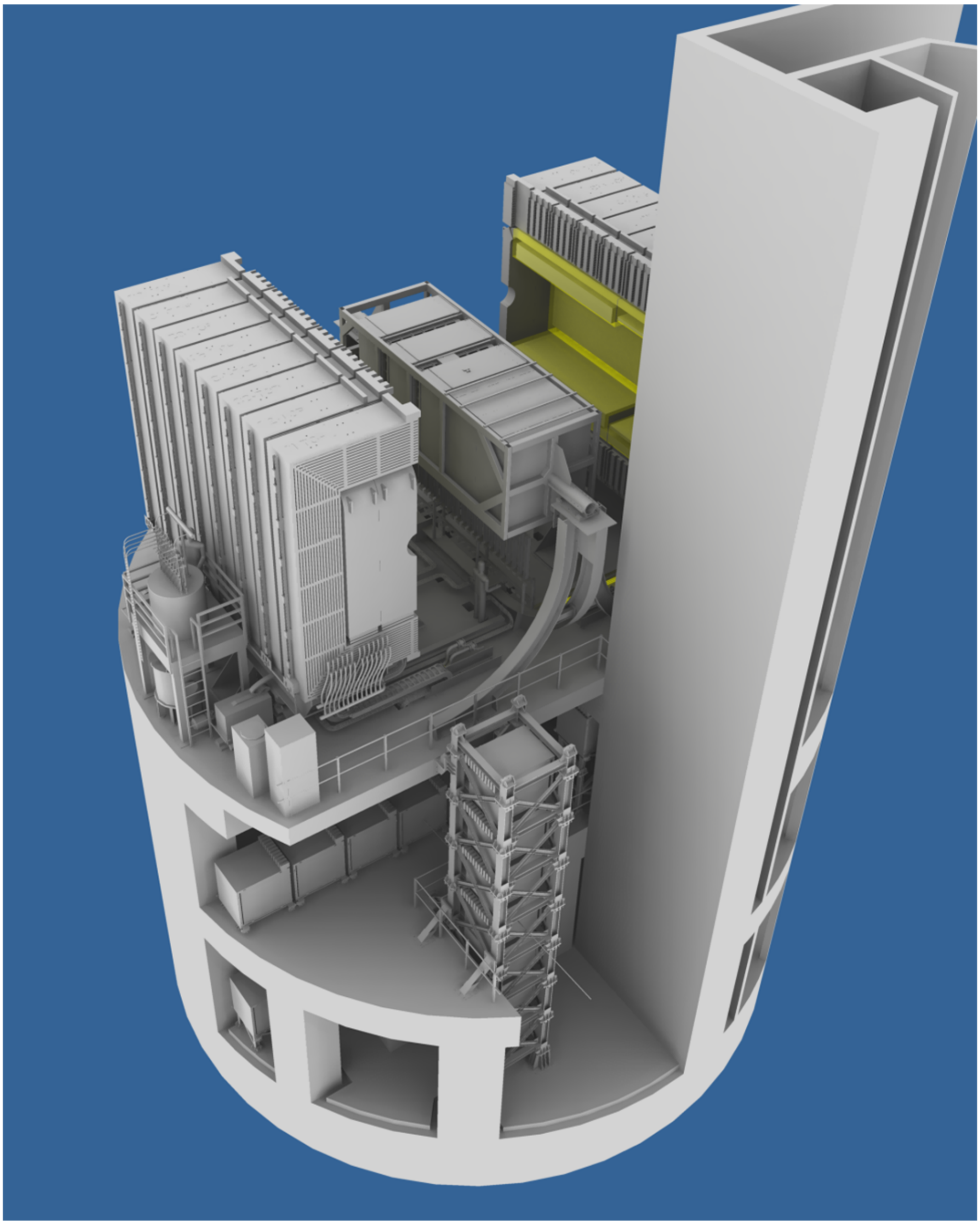

Figure 3.4: *3D render of the ND280 detector complex. The off-axis detector with the open magnet are located on the upper level. The horizontal INGRID modules are located on the level below with the vertical column of INGRID modules located to the fore [32].*

central modules lying on the beam axis. Two further modules are located off-axis in the upper half of the cross to check the cylindrical symmetry of the beam, as shown in figure 3.5. The detector was installed and commissioned in the pit in summer 2009 with the first neutrino event candidate observed in November of that year.

INGRID can measure the beam centre with a precision better than 28 cm corresponding to 1 mrad or a shift of around 2% in the peak of the neutrino energy spectrum.

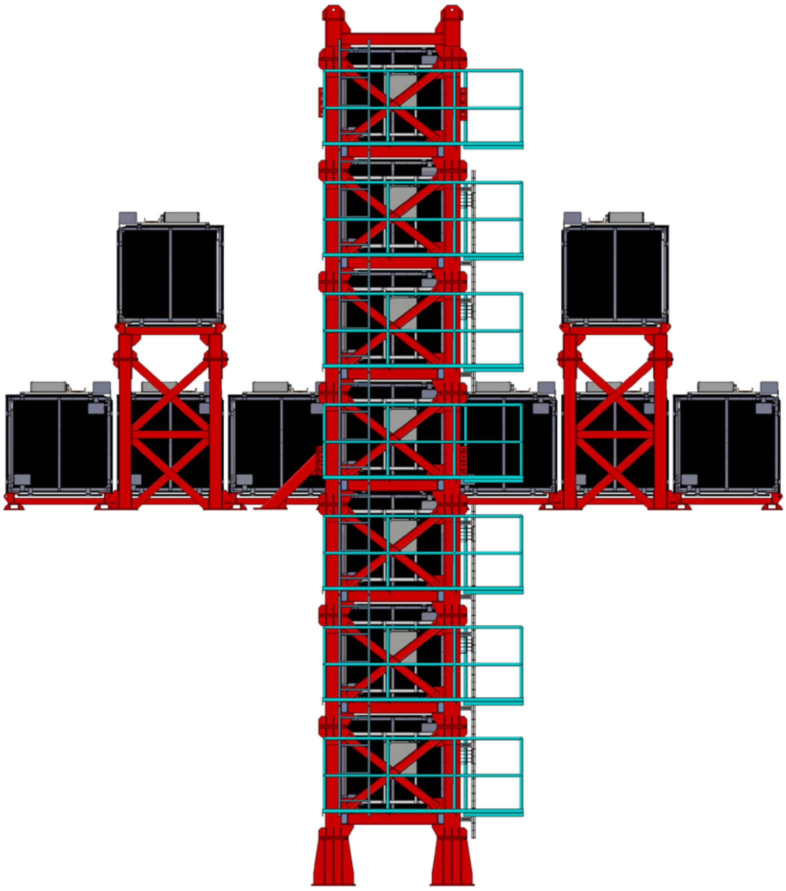

Figure 3.5: *Downstream view of the INGRID detector from [32].*

3.3.2 ND280

ND280 is a fine-grained off-axis tracking detector which measures the flux, energy spectrum and electron neutrino contamination in the direction of Super-Kamiokande. It also provides cross-section measurements for interactions relevant to the disappearance and appearance searches at Super-Kamiokande.

As shown in figure 3.6, ND280 consists of a central fixed basket containing a π^0 detector (P0D), a tracker consisting of three time projection chambers (TPCs) and two fine grained detectors (FGDs), and an electromagnetic calorimeter (ECal). The basket is surrounded by further electromagnetic calorimeters. Encasing this inner detector is an iron yoke magnet taken from the UA1 experiment at CERN. The magnet is additionally instrumented with scintillator to track out-going muons. The external dimensions of the magnet are $5.6 \times 6.1 \times 7.6$ m^3, while the inner detectors occupy a space of $3.5 \times 3.6 \times 7$ m^3. The convention for the ND280 co-ordinate system puts z in the beam direction x in the horizontal and y vertical.

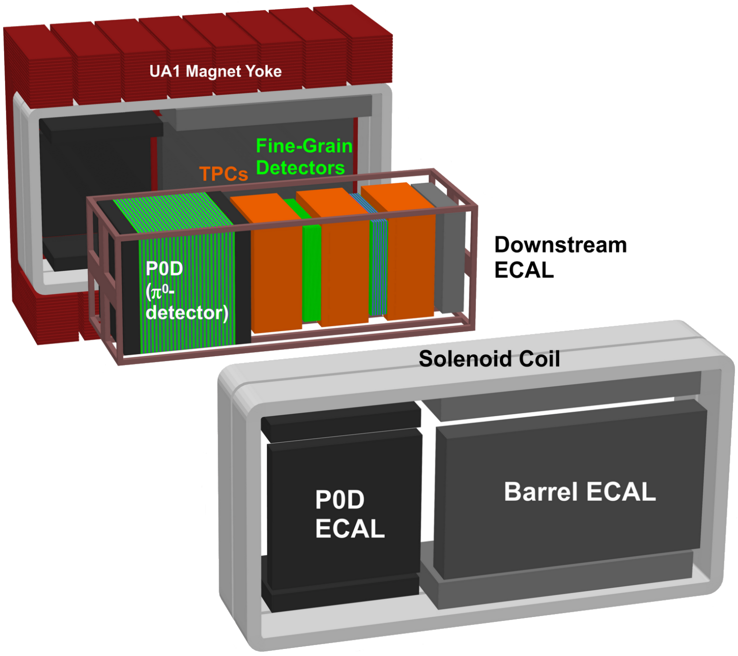

Figure 3.6: *An exploded view of the ND280 detector. The beam propagates from left to right. Image taken from [32].*

Neutral current π^0 interactions on water form the dominant background to the ν_e appearance search at Super-Kamiokande, but are poorly understood at the T2K energy regime. The P0D's principal role is to measure various inclusive and exclusive π^0 cross-sections in the unoscillated T2K beam to allow for more accurate background subtraction at Super-Kamiokande. Further to that, the P0D will be able to complement the tracker by measuring the intrinsic electron neutrino beam flux via the CCQE channel which is an irreducible background at Super-Kamiokande.

The P0D is the most upstream ND280 sub-detector. It is composed of x and y planes of scintillator bars layered in various sections with brass and lead sheets. The central section contains water target bags which can be filled or emptied and as such the cross-sections on water can be calculated from the difference in interaction rates. The P0D has a mass of 16.1 t with water and 13.3 t when emptied. It was installed in the basket in late 2009.

The tracker lies in the next downstream section of the basket and consists of two FGDs interleaved with three TPCs. The principal goals of the tracker are to measure the muon neutrino and electron neutrino fluxes, energy spectra and various cross-sections relative to CCQE. It was installed in the basket between October 2009 and January 2010.

The FGDs form the bulk of the target mass for the tracker as well as providing high resolution tracking of charged particles near the interaction vertex. They are composed of alternating x-y planes of scintillator bars, with the second FGD also having layers of water target for measuring neutrino interactions on water as well as carbon. The outer dimensions of the FGDs are $2.30 \times 2.40 \times 0.37$ m^3 (width × height × depth in the beam direction) with a target mass of around 1.1 t each.

The TPCs that sandwich the FGDs provide the complementary function of being able to measure the momentum of charged particles from their curvature in the magnetic field and to provide particle identification by a dE/dx measurement. They consist of an active volume filled with an argon based drift gas. The volume is bisected by a y-z cathode plane which faces two sets of readout planes on either side of the detector. All the TPCs are identical in construction and have outer dimensions of $2.3 \times 2.4 \times 1.0$ m^3 (width × height × depth in the beam direction).

At the end of the basket and forming a surround to it are 13 electromagnetic calorimeter modules (ECals) which provide near hermetic coverage for outgoing particles from the basket detectors. The ECals complement the work of these inner detectors by measuring the energy and direction of photons as well as the detection of charged particles allowing for the full reconstruction of events.

There are three different types of ECal modules: the P0DECal around the P0D, the Barrel ECal around the tracker, and the DSECal behind the tracker. The Barrel and DSECal share the same basic structure, where layers of scintillator bars are arranged in alternating orthogonal directions and are interleaved with lead absorber planes. The P0DECal is similar with the exception that all bars are longitudinal. The number and thickness of the layers varies across the different ECal types. The downstream ECal module located in the basket was installed in October 2009. The remaining ECals were installed between July and October in 2010.

The magnet, which encases the above described detectors in all but the two end faces, provides a dipole field of up to 0.2 T which is used to curve the tracks of charged particles providing charge and momentum information and allowing for particle identification.

The 850 t magnet is divided into two vertically along the off-axis beam direction (z). Each half is composed of eight C-shaped steel flux return yokes which in turn are made of 16 steel plates. Each half of the magnet contains a set of two aluminium coils. Positioned within the air gaps that separate the steel plates in the yokes are 440 scintillator modules which form the Side Muon Range Detector (SMRD). The role of the SMRD is three fold. Firstly it can measure muons which leave the inner detectors at large angles and are therefore difficult to measure with the TPCs. Its other roles are to identify backgrounds coming from beam interactions in the yokes and the surrounding area as well as to provide triggers for incoming cosmic muons which can be used as a calibration source for the inner detectors. The SMRD was installed and commissioned between February 2009 and September 2009.

As the scintillator modules of the ND280 inner subdetectors are instrumented inside the magnetic field, traditional photomultiplier tubes cannot be used . Instead, specially designed multi-pixel photon counters (MPPCs) were manufactured by Hamamatsu Photonics for the purpose [34]. The MPPCs are a type of silicon photomultiplier constructed from 667 avalanche photodiode pixels arranged in a 1.3 mm square. The MPPCs are fitted into a protective shroud and attached via a mini-coaxial cable to the readout electronics. The wavelength-shifting fibres which run through the scintillator terminate against the light sensitive face of the photon counters.

A total of about 64,000 MPPCs were manufactured for T2K. Around 10,000 of these were assembled and tested at Queen Mary, a quarter of which contributed as a service task for this thesis.

3.4 Super-Kamiokande

Super-Kamiokande (SK) is a 50 kt water Cherenkov detector and forms the far detector for the T2K experiment [35]. It is located in a zinc mine owned by the Kamioka mining company in Mount Ikeno in the Gifu prefecture of Japan. The detector occupies a cylindrical cavern 39 m in diameter and 42 m high. There is a 1 km overburden equivalent to 2700 m of water which reduces the cosmic ray background rate by around five orders of magnitude compared to at the Earth's surface.

The role of the detector for the T2K experiment is to measure the neutrino charged-current interaction energy spectrum and look for effects of neutrino oscillation as regards both muon neutrino disappearance from the beam and electron neutrino appearance. Super-Kamiokande will also measure neutral current interactions to provide normalisation for event rates.

Super-Kamiokande began operation in 1996. Since then it has undergone four data collecting phases. The current phase, SK-IV, which featured upgraded readout electronics began in 2008 and will continue for the running of the T2K experiment.

3.4.1 Principles of Neutrino Detection at Super-Kamiokande

Super-Kamiokande detects neutrino interactions by the Cherenkov radiation emitted by outgoing charged particles. Cherenkov radiation is created when a charged particle travels faster than the speed of light in the medium; for a wavelength dependent refractive index $n(\lambda)$ this speed is given by c/n, where

c is the speed of light in a vacuum. Super-Kamiokande's detection medium is ultra-pure water and has a refractive index of 1.33 for wavelengths relevant to the experiment.

The Cherenkov photons emitted by a charged particle with velocity v with respect to the medium produce a cone with an axis centred on the particle's direction of motion and with an opening angle (θ_c) defined by the velocity of the particle, such that:

$$\cos\theta_c = \frac{1}{n\beta} \tag{3.1}$$

where $\beta = v/c$, as illustrated in figure 3.7. For an ultra-relativistic particle ($\beta \approx 1$) the opening angle (θ_c) is approximately 42 degrees in water. The number of Cherenkov photons (N) emitted per unit wavelength (λ) per unit distance (x) travelled by a charged particle is given by

$$\frac{d^2N}{dxd\lambda} = \frac{2\pi\alpha}{\lambda^2}\left(1 - \frac{1}{n^2\beta^2}\right) = \frac{2\pi\alpha}{\lambda^2}\sin^2\theta_c, \tag{3.2}$$

where α is the fine structure constant. The photon production rate at Super-Kamiokande is therefore about $dN/dx \approx 3400/\mathrm{cm}$ for the region between 300 and 500 nm, where the detector is most sensitive.

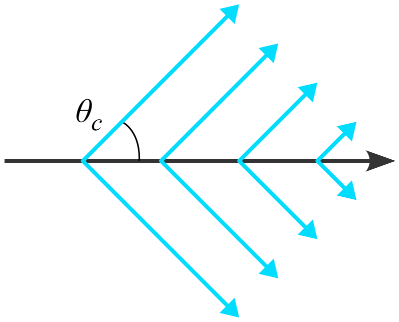

Figure 3.7: *Opening angle of Cherenkov radiation emitted by a charged particle travelling from left to right.*

Super-Kamiokande detects Cherenkov photons with photomultiplier tubes (PMTs). For a charged particle to be detected it must be above the Cherenkov threshold for long enough that there are sufficient photons produced to be detected above electronic noise. The number of photons deposited, hit time and pattern allow for the reconstruction of the position, direction and type of the original charged particle. From this it is possible to learn about the neutrino interaction that produced it. Super-Kamiokande is sensitive to neutrinos with energies between 4 MeV and 1 TeV; T2K operates in Super-Kamiokande's high energy regime which corresponds to events with energy greater than 30 MeV.

3.4.2 Detector Overview

Super-Kamiokande is composed of an inner and outer detector separated by a cylindrical stainless steel support structure (figure 3.8). The inner detector (ID) is the primary component. The role of the ID is to measure Cherenkov radiation produced by neutrino interactions within its fiducial volume.

The ID has an internal diameter of 33.8 m, a height of 36.2 m and contains 32.5 kt of the 50 kt ultra-pure water that makes up the target mass of Super-Kamiokande. The inner wall of the ID is lined with 11,129 inward facing PMTs providing a 40% photocathode coverage. The PMTs are hemispherical in shape with a 50 cm diameter. Surrounding the PMTs is black plastic sheeting (polyethylene telephthalate) designed to absorb light, minimising back scattering and transmission to the Outer Detector.

The Outer Detector (OD) is the water filled region enclosing the ID on all sides, from the outward face of the steel vessel to the cavern wall, a distance of approximately 2 m. The OD is more sparsely instrumented than the ID with 1,885 PMTs arranged only on the outer face of the steel structure. In addition, the OD PMTs are smaller than the ones found in the ID having a diameter of 20 cm. To compensate for this sparse instrumentation, the walls of the OD are lined with Tyvek, a highly reflective covering.

Originally used as an active veto for cosmic rays and other backgrounds, the OD's principal role for the T2K experiment is to ensure the full containment of neutrino interaction events in the ID by excluding events where there is activity in the OD.

A 50 cm dead space exists between the two detectors which is occupied by the services. Plastic sheeting prevents any light leaking between the two.

The ultra-pure water in the tank is maintained by constantly cycling it

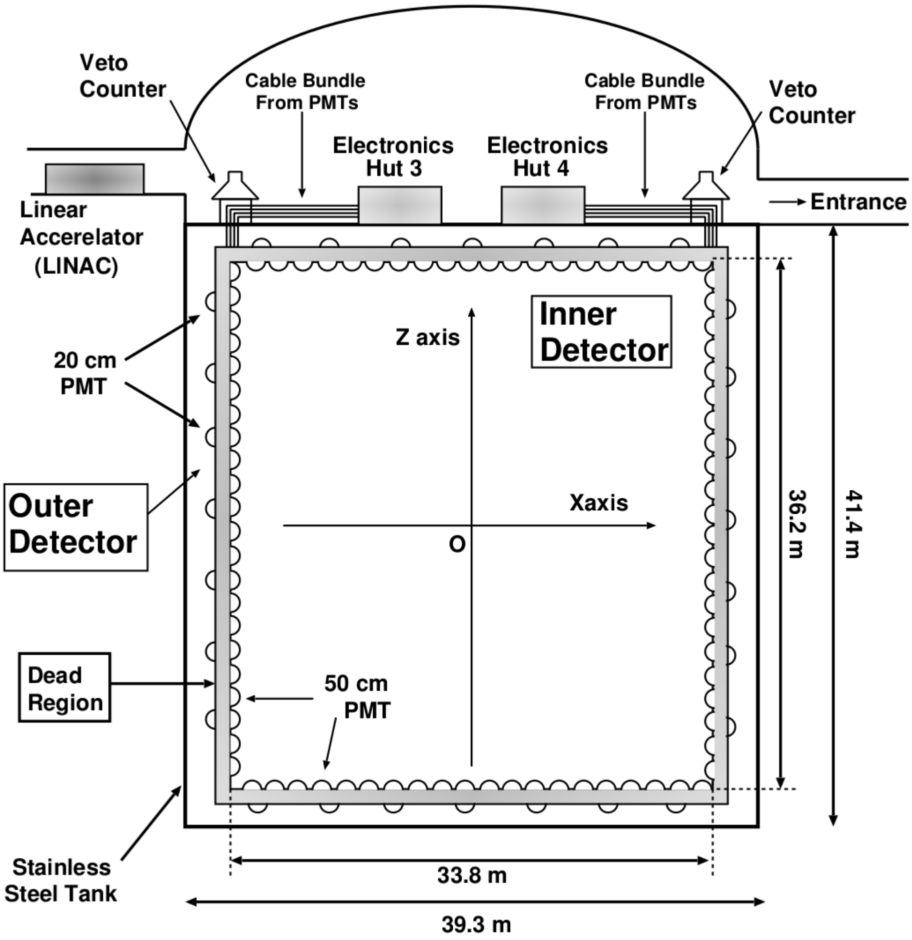

Figure 3.8: *Schematic cross-section of the Super-Kamiokande detector.*

through a purification system at a rate of around 35 tonnes/hour. This removes particulates from the water as well as killing bacteria and extracting any dissolved gas. The reason for this is to maintain a consistent transparency and therefore attenuation length for the light in the tank. The water is also cooled to a constant temperature of around 12°C.

3.4.3 The Photomultiplier Tubes

ID-PMTs

Figure 3.9 shows the structure of the ID-PMTs. The exposed part, which is sensitive to light, is made of an evacuated 52 cm diameter glass hemisphere. The inner surface of which is coated in a thin bi-alkali layer which acts as the photocathode, converting photons into photoelectrons (p.e.). The peak quantum efficiency of this process is around 21% at $\sim$ 380 nm (as shown in figure 3.10). The photoelectrons are then accelerated under an approximate 800 V potential to the first dynode which has a collection efficiency of over 70%. Each ID-PMT contains 11 dynodes resulting in a gain of around 10^7 over the initial photoelectron. In total a voltage of about 2000 V is applied. When the output for the PMT exceeds the -1mV threshold (corresponding to 1/4 p.e. equivalent input) a hit is registered by the readout electronics.

OD-PMTs

The OD-PMTs are similar in construction to the ID-PMTs but have only a 20 cm diameter. Because of the sparse instrumentation in the OD, the PMTs are also covered by a wavelength shifting plate. This absorbs light in the ultraviolet spectrum and re-emits blue wavelength light to which the PMTs are most sensitive. As a result, collection efficiency is increased by around 60%.

3.4.4 Data Acquisition

Data acquisition (DAQ) is handled by four electronics huts which sit in the cavity above the detector. Hit charge and timing information from the PMTs is collected by online PCs. The DAQ system has a buffer of a few seconds in

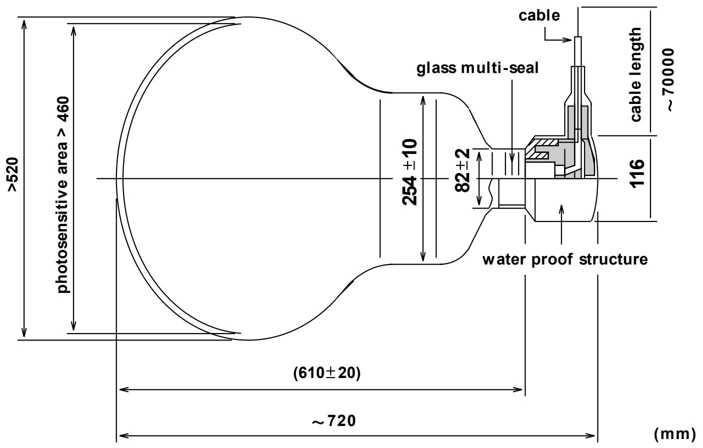

Figure 3.9: *Schematic profile of an ID-PMT. Reproduced from [35].*

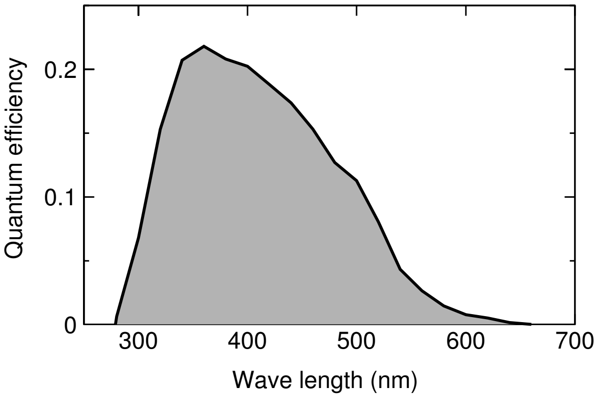

Figure 3.10: *Photocathode quantum efficiency for the PMTs. Reproduced from [35].*

which time software triggers can be applied to select data for offline storage and analysis. T2K uses a beam coincidence trigger. All hits that lie within 1 ms window centred on the spill arrival time at Super-Kamiokande are recorded. This is done on a spill by spill basis.

The spill arrival time is calculated by taking the arrival time of the first bunch of protons impinging on the target at JPARC and adding the time of flight of the neutrinos to Super-Kamiokande which is calculated to be 985 μs for the 295 km distance to the detector. To be used as a software trigger, the spill timing information needs to be sent to Super-Kamiokande from JPARC and then validated in less than 1 s. This information is sent via a dedicated network with a round trip time for the spill timing information of usually around $30-50$ ms. GPS time synchronisation ensures that JPARC and Super-Kamiokande work from the same clock (see section 3.2).

Chapter 4

Monte Carlo Simulation and Experimental Data

Monte Carlo (MC) simulation is used throughout the experiment. For the neutrino beam it is used to model the energy spectrum, composition by neutrino type, and profile of the beam for extrapolation to the near and far detectors. Both these detectors also use Monte Carlo simulations to model neutrino interactions in order to better understand detector responses and to optimise analysis techniques.

Simulation of the experimental geometry and material composition are required for accurately modelling the real life behaviour of particles and their interactions within the experiment. The Super-Kamiokande detector had already been fully simulated prior to the start of T2K; the neutrino beam line and near detector complex however needed to be fully modelled. A further service task in support of this thesis was contributing to the evaluation and refinement of the downstream ECal geometry for the ND280 software.

4.1 Beam Simulation

JNUBEAM is the Monte Carlo simulation package used for the beam. It is based on the GEANT3 simulation tool [36] which models the propagation of particles through matter. The geometry of the secondary beamline is modelled in JNUBEAM including the magnetic fields provided by the horns.

Beam simulation begins with FLUKA 2008 [37], a general purpose particle physics Monte Carlo tool that models the interaction of the 30 GeV protons from the beamline with the carbon target and the subsequent hadronic showering. Information about the particles which leave the target and their decay products is passed onto JNUBEAM. JNUBEAM handles the propagation through the decay volume and the decay into neutrinos. The neutrino flavour, energy, parent particle information and probability of intersection with either the near or far detectors are stored. From this the neutrino flux is calculated.

Measurements from other experiments are used to tune the parameters of JNUBEAM . In particular the NA61/SHINE experiment at CERN [38] provides direct measurements of kaon and pion production from a 30 GeV proton beam impinging on a graphite target, mirroring the T2K arrangement.

4.2 Super-Kamiokande Simulation

Monte Carlo simulation at Super-Kamiokande is used to produce artificial data from the flux predictions created by JNUBEAM. This output represents data for many times the exposure that the experiment will run over. The simulation is split into two parts. NEUT models the neutrino interactions, while SKDETSIM handles the propagation of particles through the detector as well as detector response.

NEUT [39] is the neutrino interaction generator that has been in use and development by the Super-Kamiokande and previously the Kamiokande collaboration for over 20 years. Designed for use with a water target, NEUT models primary neutrino interactions with both free protons and oxygen nuclei for a given flux and energy spectrum. Interactions of secondary generated particles such as pions, kaons and scattered nucleons within the nucleus are also simulated. A list of final state particles and underlying interaction are passed onto SKDETSIM.

SKDETSIM, like JNUBEAM, is based on the GEANT3 simulation tool [36]. It propagates particles across the detector. For hadronic interactions in water an additional package called CALOR [40] is used in the 1 GeV region, with custom routines covering the sub 500 MeV pions. Laser calibration sources and cosmic ray muon data are used to tune the simulation for absorp-

	No. of Events Generated	Years Equivalent Unoscillated
ν_μ	979723	439.13
$\bar{\nu}_\mu$	489718	449.82
Intrinsic ν_e	979486	21761.39

Table 4.1: *Summary of Super-Kamiokande 10a Monte Carlo Simulation files. 1 nominal year* $= 1.66 \times 10^{21}$ *POT. Normalisation from [41].*

tion and scattering by both the water and with the ID walls. The long running period of Super-Kamiokande has allowed the development of SKDETSIM to the level where it is possible to model events to the few percent level.

4.2.1 10a MC Data

This study uses the 10a Monte Carlo production created from the 10a beam flux files with version 10a of the Super-Kamiokande software and version 5.0.6 of NEUT [41]. This is the standard simulation for the 2010 and 2011 run period, with the accelerator energy, beam profile and focusing horn currents set up to match the physics run conditions .

The number of events generated for each neutrino type is shown in table 4.1. Three types are considered: muon neutrino, anti-muon neutrino and electron neutrinos intrinsic to the beam. This study looks at a nominal running period of five years as well as the data collecting period of run 1 and 2 (see section 4.3). Run time is often expressed in terms of POT (protons on target), which is the number of protons delivered to the target station associated with good spill data. A nominal 5 year run period is defined by 8.33×10^{21} POT while run 1 and 2 accumulated 1.45×10^{20} POT of good spills at Super-Kamiokande. Normalisation of the Monte Carlo data is from the work of Albert and Terri [41].

The Monte Carlo generated events are produced using an unoscillated beam flux. Oscillation is considered with an energy dependent weighting. The Monte Carlo is weighted using the following values for the oscillation parameters and a three flavour oscillation equation:

$$
\begin{aligned}
\sin^2 2\theta_{12} &= 0.8074, \\
\sin^2 2\theta_{23} &= 1.0, \\
\sin^2 2\theta_{13} &= 0.1, \\
\Delta m^2_{12} &= 7.6 \times 10^{-5}\ \text{eV}^2, \\
\Delta m^2_{32} &= 2.4 \times 10^{-3}\ \text{eV}^2, \\
\delta &= 0.
\end{aligned}
$$

These values are consistent with global fits such as that given in table 2.1 [30].

Figure 4.1 shows how each simulated neutrino type contributes to the expected energy spectrum of the events generated in the ID's fiducial volume. The vast majority come from the muon neutrino simulation.

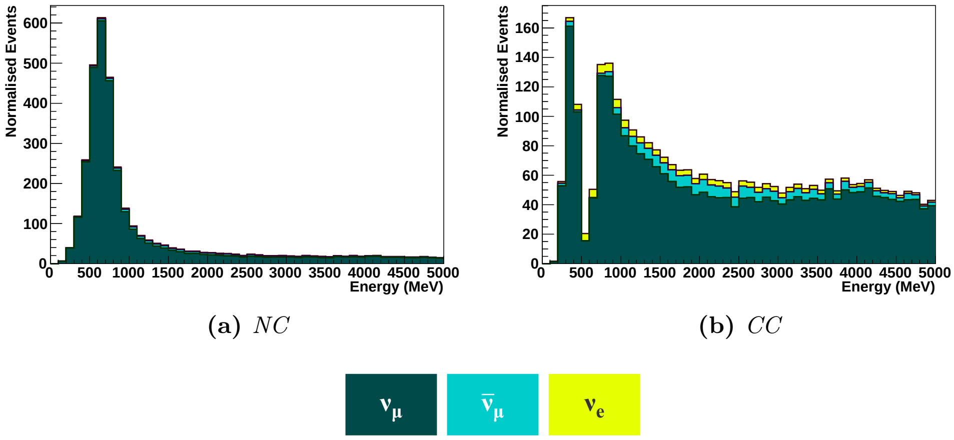

(a) *NC*

(b) *CC*

Figure 4.1: *Contribution of the different MC neutrino source types to the energy spectrum of simulated events in Super-Kamiokande's fiducial volume. 4.1a shows the breakdown of the neutral current (NC) spectrum while 4.1b shows the charged current (CC) spectrum. Oscillation is applied to the CC events with the assumption that* $\Delta m^2_{32} = 2.4 \times 10^{-3}$ eV^2 *and* $\sin^2 2\theta_{23} = 1$. *The plots are normalised to a nominal 5 year running period* (8.33×10^{21} *POT.*

4.3 Data

Physics data taking began in January 2010. This thesis examines data taken up to the 11th of March 2011, when data taking was suspended following the Tōhoku earthquake and tsunami. The data collected in this period is split into two runs separated by the 2010 summer shut-down (figure 4.2).

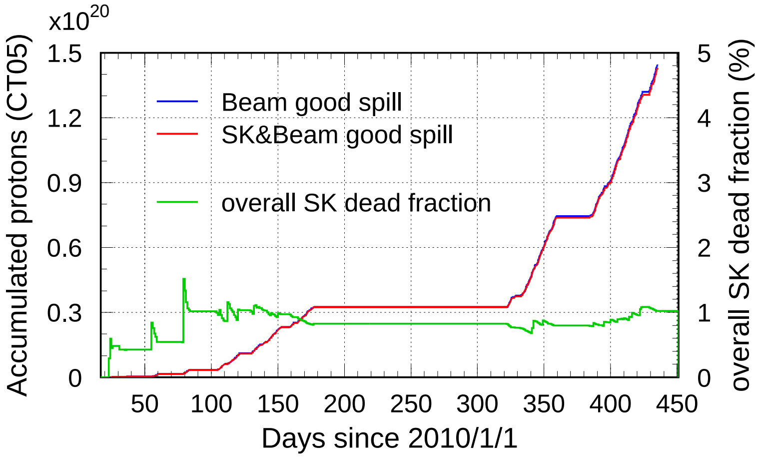

Figure 4.2: *Beam performance and SK livetime for run 1-2. Blue line shows delivered number of POT as a function of time while the red line shows accumulated POT for good beam spills combined with SK livetime. A total of* 1.45×10^{20} *POT have been delivered up to March 2011, with the summer 2010 shutdown occupying the stable part in the central region of the timeline. Reproduced from [42].*

Run 1 refers to data collected between January and June 2010. In this period the beam delivered 3.35×10^{19} POT in spills of 6 bunches. Super-Kamiokande had a livetime of 99% and accumulated good spill data of 3.23×10^{19} POT.

Run 2 ran from November 2010 to March 2011. For this run the number of bunches per spill was increased to 8. Delivered POT stand at a total of 1.45×10^{20}.

4.3.1 Good Spill Selection at Super-Kamiokande

Good beam spills are flagged as bad by Super-Kamiokande if any of the following conditions is met:

1. the DAQ program is not running;
2. the current subrun (corresponding to about one minute of data-taking) is declared bad, usually because of PMT malfunction or blasting taking place in the mine;
3. either the DAQ system or the GPS has raised an error flag;
4. pedestal data are being taken, or the TDC chips are being reset;
5. there is cosmic-ray related activity in the detector immediately before the spill.

The total loss of spills from these conditions is less than 1% [43][42].

4.4 Event Classification at Super-Kamiokande

For data, a beam event is classified as a peak in ID-PMT hits that exceeds 47 hits in 200 ns and which lies within $-5 \rightarrow +35$ μs of the calculated spill arrival time. For Monte Carlo no such timing cut is required as only beam events are simulated. Beam events are further classified [43].

4.4.1 Fully Contained Events

Fully contained (FC) events are those where the event occurs in and is fully confined to the ID. These are the beam events that are needed for analysis as all information provided by the Cherenkov radiation is contained within the ID.

To exclude events that are not fully contained PMT hit clusters are searched for in the OD. If the largest found cluster has more than 15 hits then the event is excluded. This classification is applied to both data and Monte Carlo.

Two further cuts are applied to the data to complete the fully contained criteria. The first is a low energy event cut. This cut removes events where the total charge of the ID-PMT hits is less then 200 photoelectrons in a 300 ns window and also events where a single PMT has more than half the total charge. These events are generally caused by radioactivity near the PMT. This cut removes 0.33% of beam events from the fully contained sample.

The second cut is a flasher cut. The purpose of the cut is to remove events caused by light produced by a spontaneous discharge from the internal dynode of a PMT, *i.e.* events that are an artefact of the detector. Two methods are used to remove such events. Firstly, typical flasher events have a broader PMT hit timing distribution than neutrino events, so events are removed that have a minimum of more than 20 ID-PMT hits in a 100 ns time window in the region +300 to +800 ns from the timing window centre. The second method for the removal of flasher events relies on the fact that such events produce similar repeating spatial hit patterns. A likelihood is calculated based on charge pattern and integrated charge distribution. A cut is then made optimised on atmospheric running. The loss of beam events from this cut is around 1%.

It is unnecessary to apply the low energy and flasher cuts to the Monte Carlo simulation due to the negligible effect on beam event efficiency as further selection cuts are applied.

Figure 4.3a shows the timing of all the events that lie within the $\pm 500\mu s$ beam timing window for run 1 and 2 data. The fully contained events are highlighted and all but two of these lie at the expected beam spill arrival time which is consistent with expectation [42]. The OD and low energy event rates can be seen to be constant throughout the timing window indicating that the data acquisition and event selection are unbiased with regards to this timing. Figure 4.3b shows the timing distribution in the region of the spill arrival time for the fully contained events. Although there is a small +100 ns shift in the overall position of the events due to an unknown cause, the distribution of the events otherwise closely matches the bunch structure of the beam as expected.

4.4.2 Event Reconstruction

Both Monte Carlo generated data and physics run data pass through the T2K reconstruction software. It is after reconstruction that it is possible to apply cuts to the reconstructed event variables in order to obtain samples for

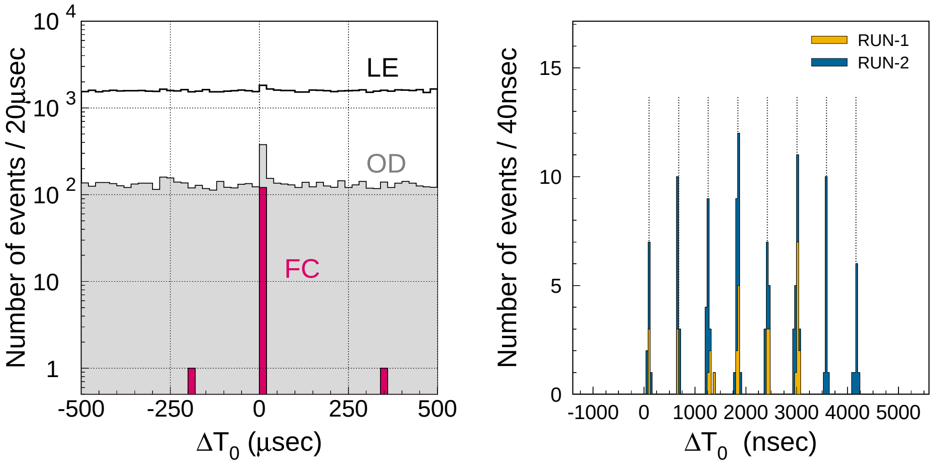

(a) *1 ms timing window* **(b)** *FC events*

Figure 4.3: *Event timings relative to the spill arrival time* ($\Delta T_0 = 0$) *for run 1-2 good SK and beam spill data. 4.3a shows all the events in the 1 ms beam timing window broken down by type: outer-detector events (OD), fully contained events (FC), and low energy events (LE). Two off-timing FC events are observed which is consistent with expectations. 4.3b shows the timing of the FC events separated into run 1 and 2 and corrected for photon travel length in the ID. The 8 dotted vertical lines represent the bunch centre positions. Observed event timings are consistent with the beam timing structure. Run 1 had 6 bunches per spill while run 2 used the full 8. Plots from [42].*

analysis. There are five stages to the reconstruction process.

Interaction Vertex

The interaction vertex is the point in the detector where the neutrino interaction occurs. Roughly calculating this point is the first stage of reconstruction, and is achieved using the timing information from each hit PMT. The initial track direction is also estimated by searching for a sharp edge in the PMT hit pattern.

Ring Counting

Charged particles from the neutrino interaction produce cones of Cherenkov light which consequently produce circular patterns on the detector wall. Because the charged particles lose energy as they propagate, they will eventually drop below the Cherenkov threshold so the shape produced will have a hollow centre. This is referred to as a Cherenkov ring. The next stage or reconstruction uses an algorithm employing a Hough transform [44][45] of the PMT charge distribution to search for these Cherenkov rings.

Particle Identification

The third stage of reconstruction separates the rings into two classes: electron-like and muon-like (figure 4.4). Electrons produce fuzzy rings due to electromagnetic showering as they propagate. A ring candidate is compared to a Monte Carlo generated ring pattern to see how electron-like it is. Muons do not scatter and produce Cherenkov rings with a well defined shape. Analytically generated ring patterns are used as a comparison for muon rings.

Momentum Reconstruction

The momentum of the ring producing particles is calculated from the observed charge assigned to each ring. Monte Carlo simulation and detector calibration is used to model the relationship between this observed charge and particle momentum.

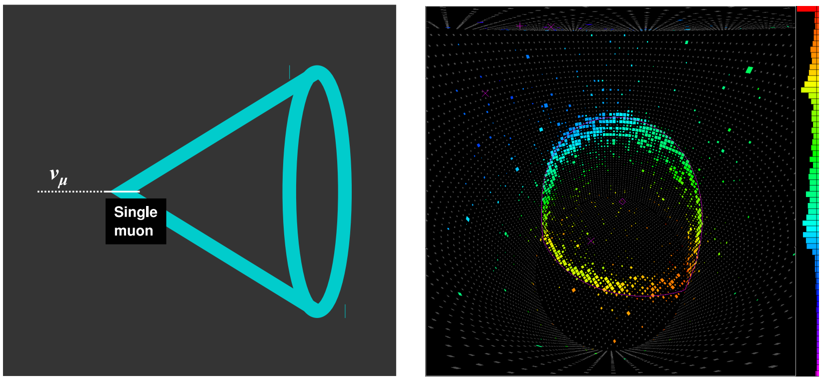

(a) *Muon-like ring formation* **(b)** *Single ring muon event*

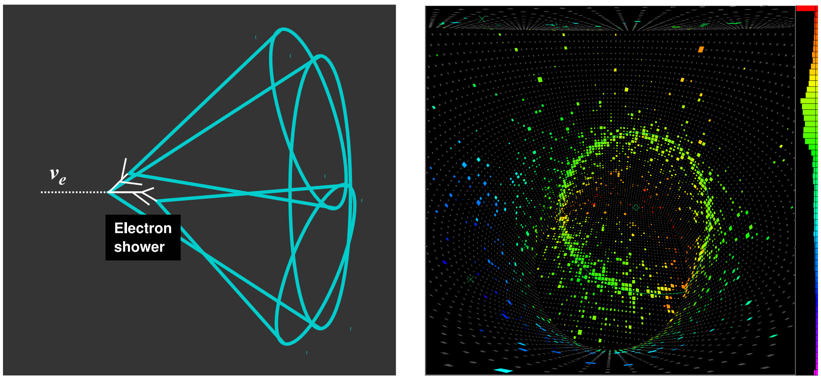

(c) *Electron-like ring formation* **(d)** *Single ring electron event*

Figure 4.4: *Illustration of ring patterns for an above Cherenkov threshold muon and electron. 4.4a shows how a neutrino interaction producing a single muon will create a well defined Cherenkov ring at the detector wall, while 4.4c shows how in the case of an outgoing electron from a neutrino interaction a more diffuse ring is formed due to electron showering. 4.4b and 4.4d show examples of ID-PMT hit patterns created by a single ring muon event and a single ring electron event respectively. The colour scale corresponds to the arrival time of light at the PMTs (blue being the earliest, red the latest). The histograms to the right of the event displays are the charge vs. time distributions. Images taken from [46].*

Decay Electrons

Finally, electrons from muon decays are searched for by looking for activity in the tank after the main neutrino interaction. This activity can be used to reconstruct the vertex and timing of the decay electrons.

4.4.3 Fully Contained Fiducial Volume Events

The ability of the inner detector to accurately reconstruct events diminishes with increased proximity to the ID wall. As such, observed FC events undergo a further cut before being used for physics analysis. This cut is the fiducial volume (FV) cut and it excludes events that have their reconstructed vertex within 2 m of the wall. This gives the fiducial volume a mass of 22.5 kt. A visible energy cut is included within the FV cut. Visible energy (E_{vis}) is the sum of the energy assuming that all rings are produced by electrons. Events with $E_{vis} < 30$ MeV are excluded.

Figure 4.5 shows the true neutrino energy spectrum and interaction mode of the surviving events generated from MC simulation for the case where neutrino oscillations are considered and for when they are not, while figure 4.6 shows a comparison of the oscillated and unoscillated spectra for charged current events only. The figures illustrate the large deformation of the energy spectrum and diminution of the sample size with oscillation as well as showing how CCQE is the most dominant charged current interaction mode in the region of maximum oscillation (around $400 \rightarrow 800$ MeV).

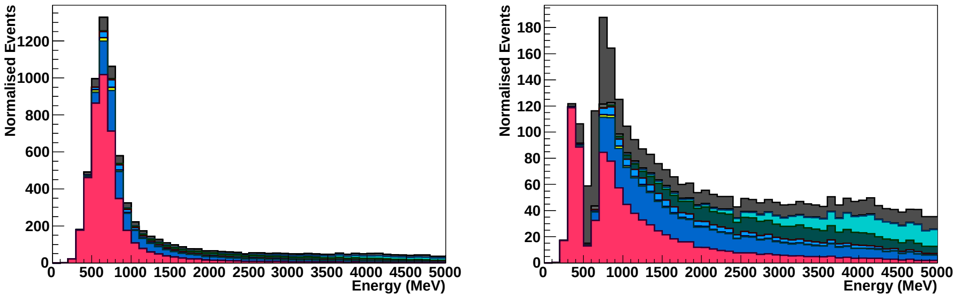

(a) *Without Oscillation* **(b)** *With Oscillation*

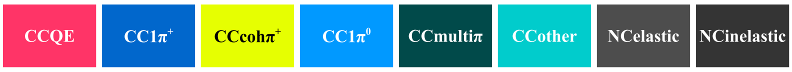

(c) *Interaction Mode Key*

Figure 4.5: *True neutrino energy spectra for FCFV events. 4.5a shows an unoscillated spectum while 4.5b shows the effects of neutrino oscillation on the event rate. Both plots are generated using the 10a muon neutrino MC data normalised to 5 years of running (*8.33×10^{21} *POT). The energy spectra are broken down by interaction mode.*

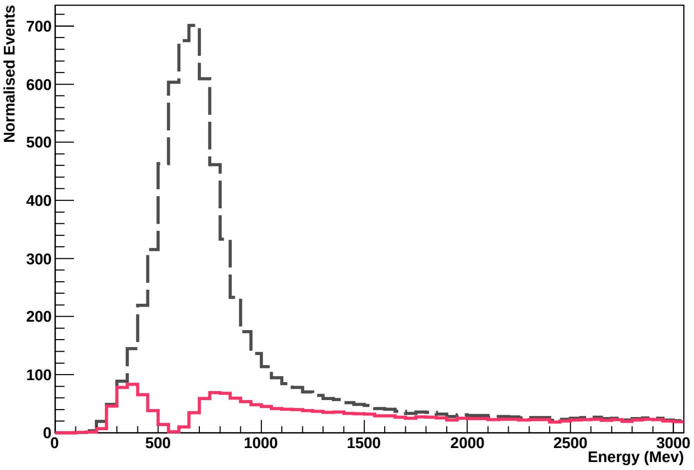

Figure 4.6: *Oscillated and unoscillated true neutrino energy spectra for FCFV charged current events. Oscillated spectrum shown with a solid pink line. Unoscillated spectrum shown with a dashed grey line. Plot is generated using the 10a muon neutrino MC data normalised to 5 years of running (*8.33×10^{21} *POT).*

Chapter 5

Event Selection at Super-Kamiokande

The trigger and selection methods described in chapter 4, in addition to the detector design, which minimises background rates, ensure that the events put forward for analysis are estimated to be at least 99.9% neutrino beam induced events [42]. This chapter looks at the methods of selecting the muon flavour component from these beam events using the reconstructed quantities extracted from the Cherenkov radiation reaching the ID-PMTs in a way which allows for the measurement of the oscillation parameters.

The proposed selections are evaluated with the use of Monte Carlo simulation; data is not examined until the selections are finalised in order to remove any bias from the process. Only the muon neutrino Monte Carlo is considered at this stage due to the low contribution of the other sources and the increased processing time and complexity associated with their inclusion.

5.1 Selection Strategy

The goal of the event selection is to maximise the sensitivity of the analysis to oscillation. As discussed in section 2.2, neutrino interactions can occur via two mechanisms: neutral current and charged current. Final state particles of the neutral current interaction reveal no information about the flavour of the parent neutrino. Although neutral current interactions can be used to measure the absolute flux of neutrinos, in terms of looking for the effects of oscillation it is the charged current interactions that should form the basis of a selection. Four further factors influence the sensitivity of a selection to oscillations:

1. **Size** A large selection size increases the statistical reliability of the data and measurement.
2. **Energy resolution** Energy resolution refers to the ability of the experiment to reconstruct the true energy of the incoming neutrinos that generated the events. With low energy resolution the reconstructed energy of an event could represent a large range of true energies. This reduces the sensitivity of the sample to oscillation as the oscillation is energy dependent, thus high energy resolution is desired.
3. **Detector and reconstruction systematics** This systematic uncertainty is related to how well the detector is modelled in Monte Carlo and as a consequence how well the effect of cuts on reconstructed variables is understood . Different selections use different variables and therefore have different systematic uncertainties.
4. **Cross-section systematics** Experimentally measured interaction cross-sections form the basis of the Monte Carlo simulation of neutrino interactions. However, some cross-sections are more well known than others. A selection which keeps a high proportion of neutrino interactions with poorly understood cross-sections will have a large systematic uncertainty. It is one of the main roles of the ND280 detector to measure cross-sections relevant to the Super-Kamiokande selections in order to reduce this uncertainty.

Interdependencies exist between these factors and it is therefore important to consider this interplay when attempting to maximise sensitivity.

For the study presented here sensitivity is calculated using a χ^2 map of the oscillation parameter space (Δm^2_{32} against $\sin^2 2\theta_{23}$), where Monte Carlo data is used to create an expectation of the reconstructed energy spectrum for a range of hypothetical oscillation parameter values. The χ^2 statistic is a measure of the consistency of a spectrum generated from such a pair of oscillation parameters with a test spectrum generated from a default parameter pair. Large systematic errors, bad energy resolution and low statistics can make samples with different oscillation parameters appear similar and as such, given a reconstructed energy spectrum the confidence in the inference of the underlying oscillation parameters would be reduced. The χ^2 statistic is defined as follows:

$$\chi^2 = \sum^{N} \frac{(n_{exp} - n_{obs})^2}{n_{obs} + \sigma_{SK}^2 n_{obs}^2 + \sigma_{int}^2 n_{obs}^2} \tag{5.1}$$

where N is the number of bins for the reconstructed energy spectrum, n_{exp} is the number of events in each reconstructed energy bin for a given point in the parameter space, n_{obs} is the number of simulated events observed in the corresponding reconstructed energy bin for the default values of the parameter space, σ_{SK} is the fractional systematic uncertainty due to the detector and reconstruction and σ_{int} is the fractional systematic uncertainty stemming from the ability to model neutrino interactions accurately. The default oscillation parameters for n_{obs} are $\Delta m^2_{32} = 2.4 \times 10^{-3}\text{eV}^2$ and $\sin^2 2\theta_{23} = 1$. The lower the value of the χ^2 statistic the closer the samples' energy spectra are to each other. A good selection will have a χ^2 value that, starting from 0 for the default values, quickly diverges as the oscillation parameters move from the default parameter values.

5.2 Single Muon-Like Ring Selection

The single muon-like ring (1Rμ) was the selection used by the K2K experiment [47]and is the starting point for this study. The selection takes events where only one ring is reconstructed and where that ring is identified as muon-like. The muon-like requirement ensures a high proportion of flavour identifying muons, while the limitation of only observing a single ring removes the majority of the neutral current and high energy processes which cloud the signal region.

In early stage running as is the case with the data from runs 1 and 2, statistical errors dominate the analysis and therefore it is important to keep the sample size high. This requirement negatively impacts energy resolution as the sample consequently consists of a sizeable proportion of events from different interaction modes.

5.2.1 Energy Reconstruction

Monte Carlo simulation predicts that the majority of the events in the sample will come from CCQE interactions. As only one energy reconstruction method can be applied to each sample, all events have their energy reconstructed as CCQE.

CCQE interactions produce a proton and a muon in the final state. The energy of the neutrino can therefore be reconstructed using two body kinematics under the assumption that the nucleus which the neutrino interacts with is at rest. The inputs are 1) the reconstructed energy and 2) the angle with respect to the beam of the outgoing muon which is assumed to create the observed Cherenkov ring. The reconstructed energy (E_ν) is expressed as follows:

$$E_\nu = \frac{m_p^2 - m_\mu^2 - (m_n - V)^2 + 2(m_n - V)E_\mu}{2(m_n - V - E_\mu + p_\mu \cos\theta_{\mu\nu})} \tag{5.2}$$

where m_p, m_n and m_μ are the masses of a proton, neutron and muon respectively, V is the binding energy, p_μ is the reconstructed muon momentum, $\theta_{\mu\nu}$ is the reconstructed angle between the ring and the beam direction and E_μ is the reconstructed energy of the muon ($E_\mu = \sqrt{p_\mu^2 + m_\mu^2}$). V is 27 MeV.

Figure 5.1 compares the reconstructed energy spectrum of MC simulated events with the truth level information. The figure illustrates how the spectrum is smeared largely by high energy events having their energy reconstructed to lower values. This is particularly the case for non-CCQE interactions where unseen particles carry away energy.

It is desirable to produce variables to measure both the shift and the amount of smearing that the reconstruction causes to the true energy spectrum. These measures can be used to compare the reconstruction performance across samples. The sample is divided into bins of true energy. For each true energy bin the difference between truth and reconstruction ($E_{\nu rec.} - E_{\nu true}$) is plotted. A Gaussian curve is fitted to the peak of the distribution. The displacement of the peak from zero is the shift in the reconstruction *i.e.* if the

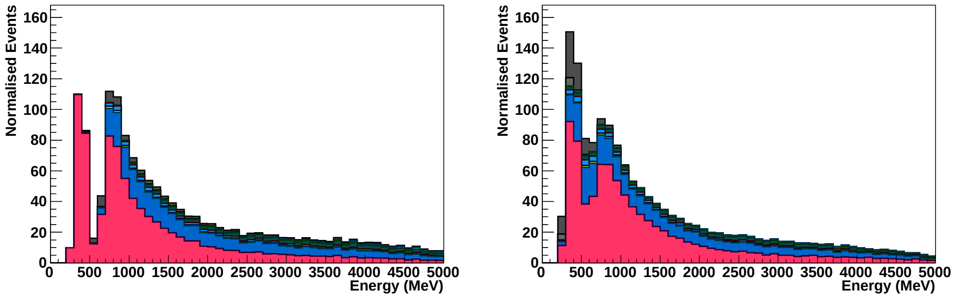

(a) *True Neutrino Energy* **(b)** *Reconstructed Neutrino Energy*

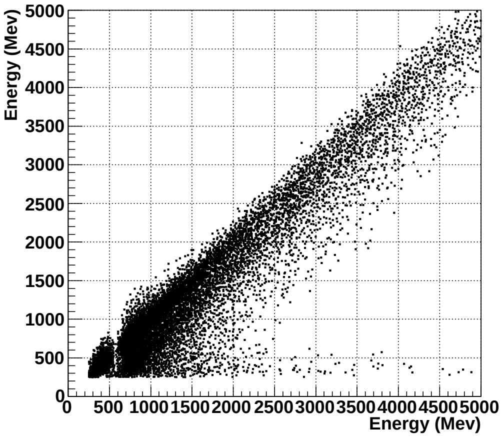

(c) *Reconstructed Vs. True Neutrino Energy*

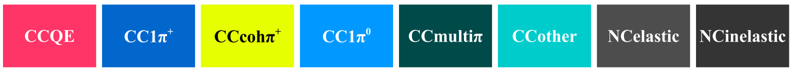

(d) *Interaction Mode Key*

Figure 5.1: *The effects of reconstruction on the neutrino energy spectrum for 1Rμ events. 5.1a shows the true energy spectrum, while 5.1b shows the reconstructed spectrum assuming CCQE (equation 5.2). 5.1c shows events plotted as a function of reconstructed and true neutrino energy. Plots are generated from oscillated 10a MC data with 5 year normalisation (8.33×10^{21} POT) and are broken down by interaction mode.*

peak of the Gaussian lies at zero no shift is observed. This shift is taken as a percentage of the mid point of the true energy bin evaluated to give a percentage shift. Because the shape of the energy difference distributions is often not Gaussian and varies across different energy regimes and samples, a root mean squared (RMS) approach is used to measure the width of the distribution and as such provide a measure of the resolution of the reconstruction. The energy resolution is defined as

$$\frac{RMS}{E_{\nu true}} = \sqrt{\frac{\sum\limits_i n_i \Delta x_i^2}{N E_{\nu true}^2}} \tag{5.3}$$

where n_i is the number of events in the i$^{\mathrm{th}}$ energy difference bin, Δx_i is the displacement of the centre of the i$^{\mathrm{th}}$ difference bin to the Gaussian peak, N is the total number of events ($N = \sum\limits_i n_i$) and $E_{\nu true}$ is the true neutrino energy of the bin for which the resolution is being evaluated.

Figures 5.2a and 5.2b show the percentage energy shift and resolution for the single muon-like ring sample respectively. When considering the consequence to event selection energy resolution is more important than energy shift. A bad resolution (*i.e.* a high value) means a loss of information, whereas a shift can just be considered as a multiplicative factor.

Figures 5.2c and 5.2d show the breakdown of the energy shift and resolution by interaction mode. The figures illustrate how CCQE interactions show the best reconstruction with the lowest energy shift and RMS. It is events from neutral current processes that show the worst reconstruction. With bad resolution and a high downward shift in energy with reconstruction, higher energy neutral current events are smeared into the disappearance region where they consequently reduce the sensitivity to oscillation.

5.2.2 Systematic Errors

During early running, as is the case with runs 1 and 2, sensitivity to oscillation is dominated by statistics, as such low systematic errors are not a strong requirement for the sample.

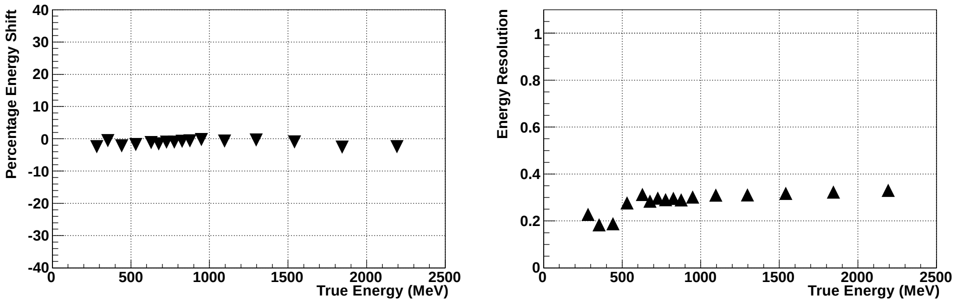

(a) *Percentage Energy Shift* **(b)** *Energy Resolution*

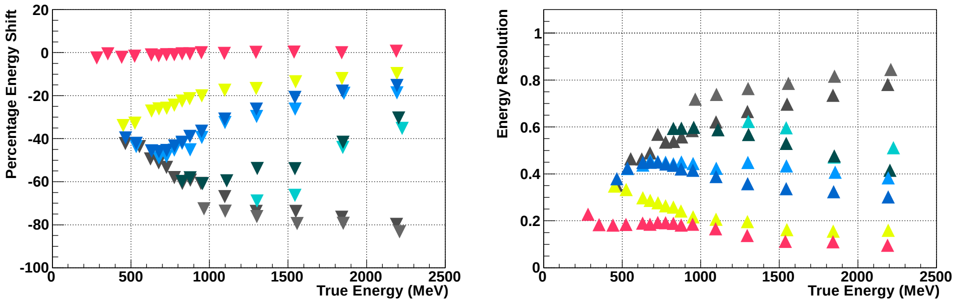

(c) *Percentage Energy Shift by Mode* **(d)** *Energy Resolution by Mode*

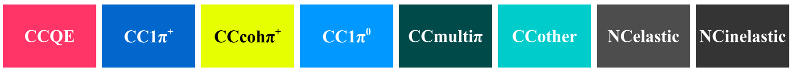

(e) *Interaction Mode Key*

Figure 5.2: *Energy resolution and peak energy shift as a function of true neutrino energy for 1Rμ events. 5.2a and 5.2b show energy shift and resolution for the full sample, while 5.2c and 5.2d are broken down by interaction mode. The figures are generated using oscillated 10a MC.*

Detector and Reconstruction Systematics

Super-Kamiokande's systematic errors for the single muon-like ring sample were evaluated by Kameda and Wendell [48] and Otani and Kameda [49]. Evaluation was conducted using Super-Kamiokande atmospheric data, including atmospheric neutrino samples, cosmic ray muons and decay-electrons as well as Monte Carlo simulation. A summary of the results is presented in table 5.1.

Cuts	Error	Total Error
Good spill	$\ll 1\%$	1%
FC	1%	1%
FV	1%	1%
1R	7.6% (CCQE), 19.9% (CCnonQE), 48.2% (NC)	9.3%
μ-like	0.3% (CC), 100% (NC)	6.3%
Total	7.7% (CCQE), 19.9% (CCnonQE), 111.0% (NC)	11.3%

Table 5.1: *Summary of systematic error estimation for 1Rμ events, taken from [48] and [49]. Errors are added in quadrature to produce the totals.*

For the ring counting and the particle ID systematic errors, uncertainty is given as a function of interaction mode. As with the energy resolution, it is the CCQE interaction mode which has the lowest uncertainty while the neutral current component has the highest.

Cross-section Systematics

For run 1 and 2 Perio *et al.* [50] provided cross-section errors based on a comparison of NEUT to external data. The uncertainty on the CCQE cross-section has a strong energy dependence as shown in figure 5.3. Cross-section uncertainty for other modes are calculated relative to the CCQE interaction and are presented in table 5.2.

As ND280 accumulates more data, accurate measurements of the cross-sections will be possible, consequently reducing the systematic uncertainty. For the nominal 5 year running period an uncertainty of 4% or better is expected across all energies for the CCQE mode with an uncertainty of about

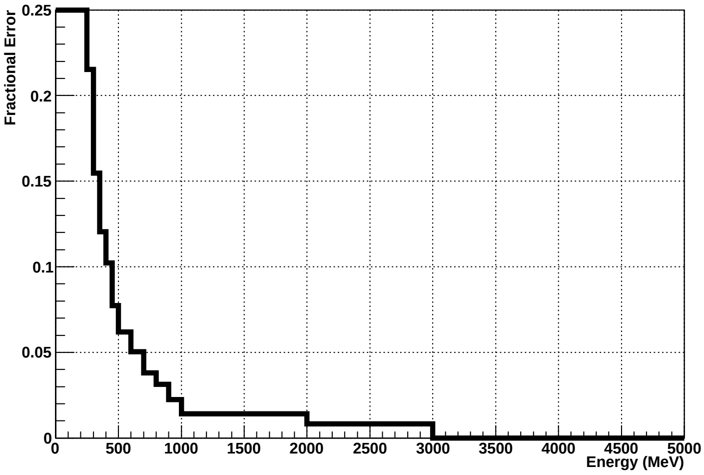

Figure 5.3: *Fractional systematic uncertainty on NEUT CCQE cross-section generated for runs 1 and 2 expressed as a function of true neutrino energy [50].*

Interaction Mode	Error
CC1π	30% (<2GeV), 20% (>2GeV)
CCcoh	100%
CCother	30% (<2GeV), 25% (>2GeV)
NC	36%

Table 5.2: *Fractional systematic uncertainties on NEUT cross-section models taken from [50] for runs 1 and 2. Here CC1π includes both CC1π^+ and CC1π^0 and energy dependence is to true neutrino energy.*

10% for the non-CCQE components as measured relative to the CCQE cross-section [51].

5.2.3 Sensitivity

Figure 5.4 shows the χ^2 sensitivity of the selection to the oscillation parameters for both a five year nominal running period and for run 1 and 2. As expected the sensitivity of the five year sample is much greater than that of the run 1 and 2 sample largely due to increased statistics.

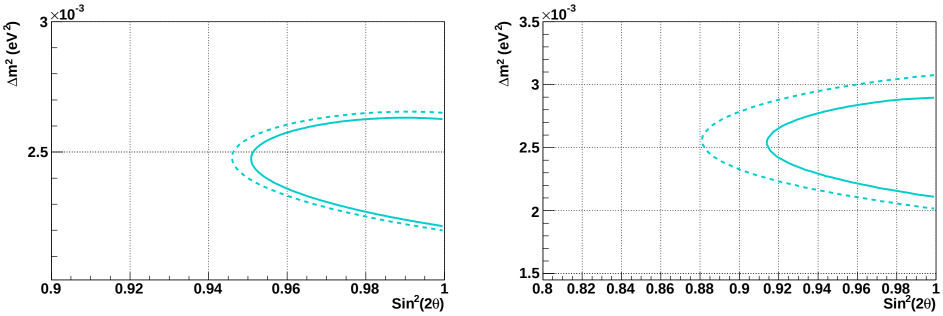

(a) *5 Years* **(b)** *Runs 1 and 2*

Figure 5.4: *Sensitivity of the 1Rμ sample to oscillation for a nominal 5 years of physics running (8.33×10^{21} POT) and for runs 1 and 2 (1.45×10^{20} POT) created using a χ^2 map. Contours define regions of parameter space with a stated maximum confidence of finding the test parameter values ($\Delta m^2_{23} = 2.4 \times 10^{-3} eV^2$ and $\sin^2 2\theta = 1$). The 68% (solid line) and 90% (dashed line) confidence regions are shown. Plots created using 10a MC with a two flavour oscillation assumption.*

5.3 Decay-Electron Enhancement

There are two main factors limiting the sensitivity of the single muon-like ring selection. Firstly, the energy resolution of the non-CCQE events is poor and reduces the overall energy resolution, and secondly, the cross-section errors on these events are also high, increasing the total systematic uncertainty for the sample. Using information about the reconstructed decay-electrons of the events (see section 4.4.2) is a possible way to improve sensitivity.

Figure 5.5 shows the single muon-like ring sample divided into the number of decay electrons observed for each event. The figure illustrates how for events with two decay electrons CCQE is not the majority event class. Most events in the two decay electron sub-sample (1Rμ2DE) come from the CC1π^+ interaction mode. As such reconstructing these events assuming CC1π^+ improves the energy resolution. Additionally the improved CCQE purity of the zero or one decay electron sub-sample means that the energy resolution improves for those events as well. Events with more than two decay-electrons can be discarded as they account for a very low percentage of the sample. The first proposed new selection is therefore formed from combining the zero or one decay-electron sample and two decay-electron sample, using a different energy reconstruction for each.

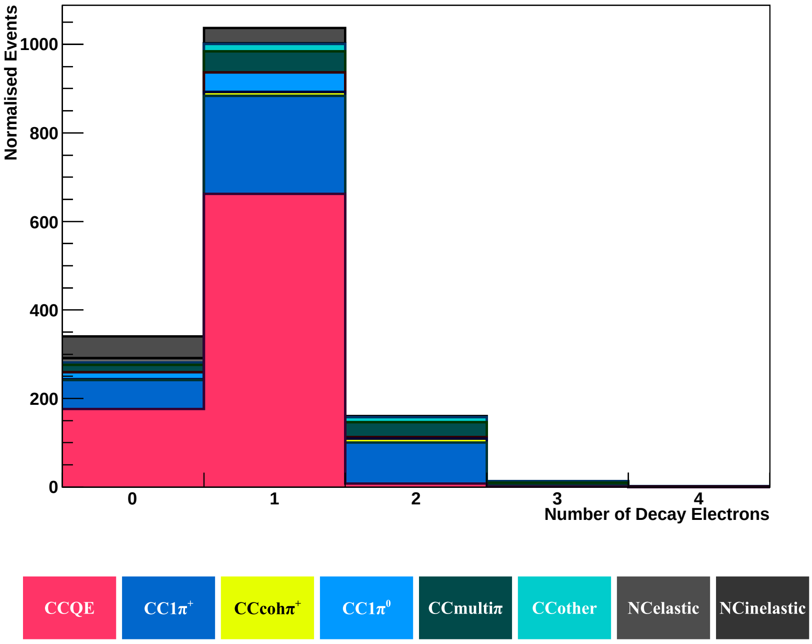

Figure 5.5: *1Rμ sample separated by number of reconstructed decay electrons and interaction mode. The figure is generated using oscillated 10a MC normalised to 5 years (8.33×10^{21} POT).*

5.3.1 Energy Reconstruction

For CC1π^+ events where only one ring is observed, the outgoing pion does not have enough energy to exceed the Cherenkov threshold. As a result, information about the pion is not available for use in energy reconstruction. Instead, a quasi-elastic style reconstruction can be applied similar to the CCQE reconstruction (equation 5.2) where the outgoing proton is replaced with the intermediate Δ resonance of the CC1π^+ interaction (see section 2.2). The reconstruction equation is then:

$$E_\nu = \frac{m_\Delta^2 - m_\mu^2 - (m_p - V)^2 + 2(m_p - V)E_\mu}{2(m_p - V - E_\mu + p_\mu \cos\theta_{\mu\nu})} \tag{5.4}$$

Figure 5.6 shows the true and reconstructed energy spectra of the two decay-electron sub-sample both for the case where the events are reconstructed using the standard CCQE reconstruction and for the CC1π^+ reconstruction case. The plots show that no oscillation dip is visible in this selection due to the CC1π^+ cross-section only becoming significant just after the point of maximum oscillation i.e. around 700 MeV. The sample however is still expected to suffer a large deformation in shape and statistics as a result of oscillation. Comparison of the energy spectra of the two reconstruction methods to the true neutrino energy spectrum shows that it is the CC1π^+ reconstruction that shows the best performance as would be expected.

Figure 5.7 shows the energy shift and resolution of the sample. Energy resolution for the events improves from CCQE reconstruction. The dominant CC1π^+ events show a reduction of over 50% in both resolution and absolute shift around the 800 → 1000 MeV region which is the peak of the true neutrino energy spectrum.

Figure 5.8 shows the true and reconstructed energy spectra of the zero or one decay-electron sub-sample while figure 5.9 shows the energy resolution and percentage energy shift of the sample. The figures illustrate the increased CCQE purity of this sample in comparison to the single muon-like ring parent sample (figure 5.1) and also show a slight improvement in the energy resolution and percentage energy shift due to this increased purity. This improvement is very small as only a few neutral current and other high energy non-CCQE events are removed by the decay-electron cut.

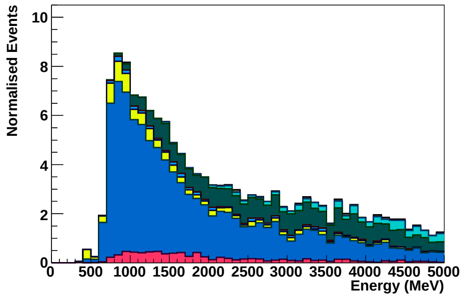

(a) *True Neutrino Energy*

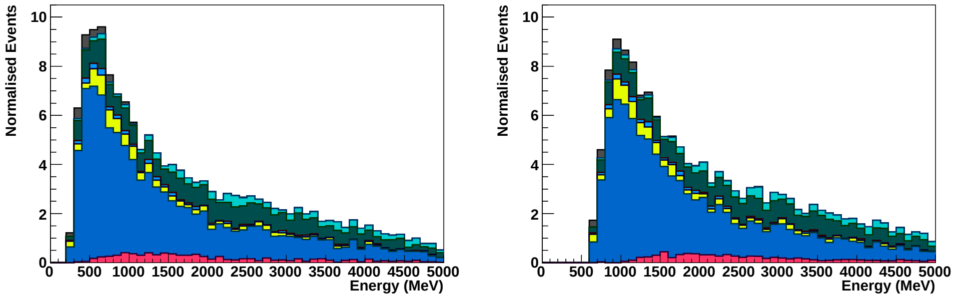

(b) *CCQE Reconstructed Neutrino Energy* **(c)** *CC1π^+ Rec. Neutrino Energy*

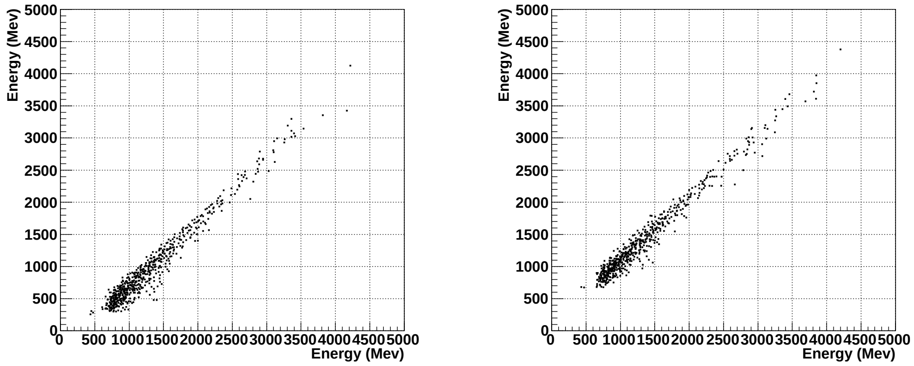

(d) *CCQE Rec. Vs. True Neutrino Energy* **(e)** *CC1π^+ Rec. Vs. True Neutrino Energy*

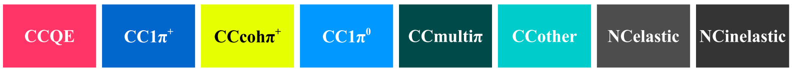

(f) *Interaction Mode Key*

Figure 5.6: *The effects of reconstruction on the neutrino energy spectrum for 1Rμ2DE events. 5.6a shows the true energy spectrum, while 5.6b shows the reconstructed spectrum assuming CCQE (equation 5.2) and 5.6c assuming CC1π^+ (equation 5.4). 5.6d and 5.6e show events plotted as a function of reconstructed and true neutrino energy for CCQE and CC1π^+ reconstruction respectively. Plots are generated from oscillated 10a MC data with 5 year normalisation (8.33×10^{21} POT) and are broken down by interaction mode.*

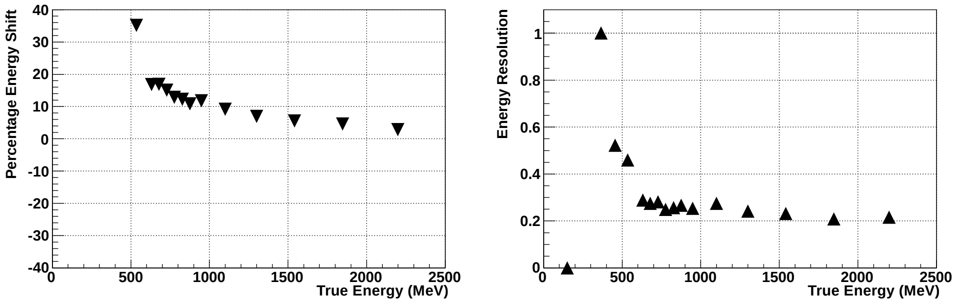

(a) *Percentage Energy Shift* **(b)** *Energy Resolution*

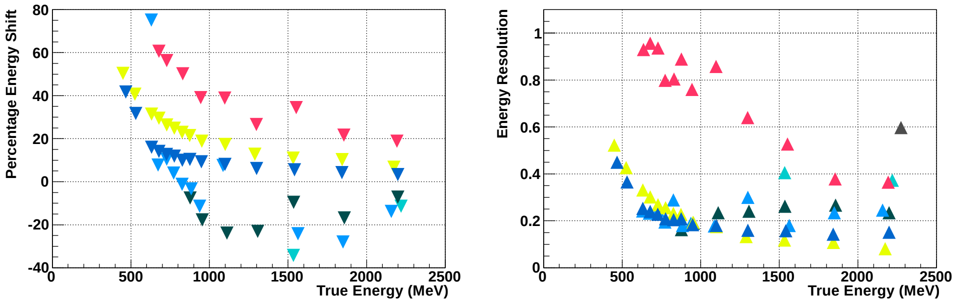

(c) *Percentage Energy Shift by Mode* **(d)** *Energy Resolution by Mode*

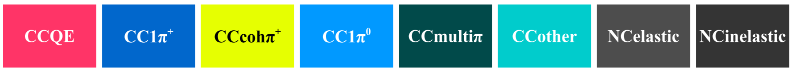

(e) *Interaction Mode Key*

Figure 5.7: *Energy resolution and peak energy shift as a function of true neutrino energy for 1Rμ2DE events. 5.7a and 5.7b show energy shift and resolution for the full sample, while 5.7c and 5.7d are broken down by interaction mode. The figures are generated using oscillated 10a MC.*

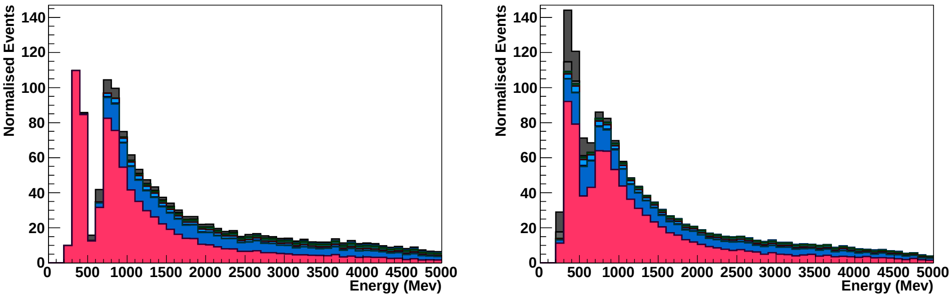

(a) *True Neutrino Energy* **(b)** *Reconstructed Neutrino Energy*

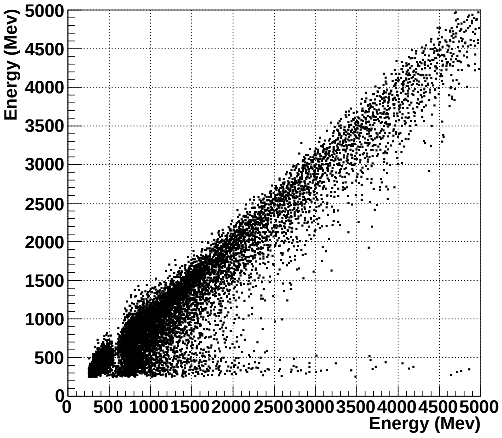

(c) *Reconstructed Vs. True Neutrino Energy*

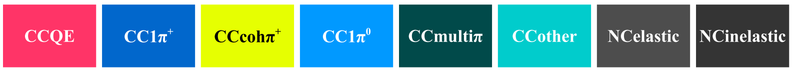

(d) *Interaction Mode Key*

Figure 5.8: *The effects of reconstruction on the neutrino energy spectrum for 1Rμ01DE events. 5.8a shows the true energy spectrum, while 5.8b shows the reconstructed spectrum assuming CCQE (equation 5.2). 5.8c shows events plotted as a function of reconstructed and true neutrino energy. Plots are generated from oscillated 10a MC data with 5 year normalisation (8.33 × 10^{21} POT) and are broken down by interaction mode.*

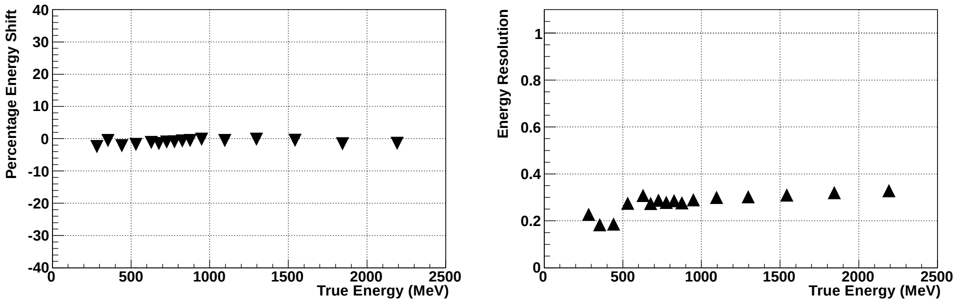

(a) *Percentage Energy Shift* **(b)** *Energy Resolution*

Figure 5.9: *Energy resolution and peak energy shift as a function of true neutrino energy for 1Rμ01DE events. The figures are generated using oscillated 10a MC.*

5.3.2 Systematic Errors

The systematics errors presented in section 5.2.2 for the single ring muon-like selection are still valid for both the decay-electron based sub-samples though the Super-Kamiokande systematic errors require re-weighting for the new interaction mode composition of each sample. An additional decay electron systematic is also required and is again obtained from the work of Kameda and Wendall [48]. The detector and reconstruction systematic values are shown in table 5.3.

Cuts	1Rμ	1Rμ01DE	1Rμ2DE
Good spill	1%	1%	1%
FC	1%	1%	1%
FV	1%	1%	1%
1R	9.3%	8.6%	18.6%
μ-like	6.3%	6.8%	1.6%
DE	-	1%	1%
Total	11.3%	11.1%	18.8%

Table 5.3: *Summary of detector and reconstruction systematic error estimation for decay-electron enhanced samples. Errors are added in quadrature to produce the totals.*

5.3.3 Sensitivity

Figure 5.10a shows the effects on sensitivity to oscillation that can be made using the decay electron enhancements to the single ring muon-like selection when a nominal five years of running are considered. The plot shows that the combined zero or one decay-electron sample and the two decay electron sample does in fact not improve the sensitivity to oscillation, although the zero or one decay-electron sample, when considered independently, does. The cause of this is the low sensitivity of the two decay-electron sample.

The reason for this low sensitivity is due to a few factors. First, the systematic error calculated on the cuts is higher than for other selections (18.8%) this is also true for the cross-section errors. In terms of the energy spectrum itself, the higher energy turn on of the CC1π^+ cross-section compared with the CCQE cross-section means that few events occupy the sub 600 MeV region, a region sensitive to oscillation, while additionally the CC1π^+ cross-section has a larger high energy tail which is invariant to oscillation.

Figure 5.10b shows the sensitivity of the selections when applied to a running period equivalent to run 1 and 2 data. In comparison to the five year sensitivity, the plot shows an overall reduction in sensitivity to oscillation, dominated by the lower statistics. The plot again shows how the combined sample has a reduced sensitivity when compared to its parent single muon-like ring sample. A tightening of the relative separations of the zero or one decay electron sample and the single muon-like ring sample can be seen. This is due to the dominance of lower statistics and the reduced importance of the systematic effects.

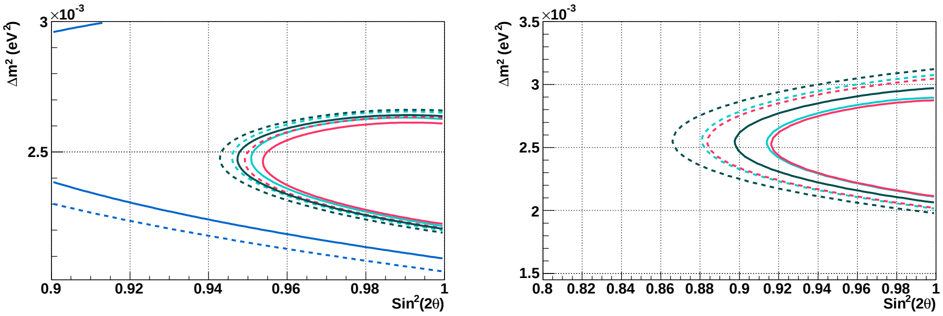

(a) *5 Years*

(b) *Runs 1 and 2*

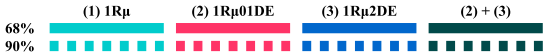

(c) *Confidence level key*

Figure 5.10: *Sensitivity of the decay electron enhanced 1Rμ sample to oscillation for a nominal 5 years of physics running (8.33×10^{21} POT) and for runs 1 and 2 (1.45×10^{20} POT) created using a χ^2 map. Contours define regions of parameter space with a stated maximum confidence of finding the test parameter values ($\Delta m^2_{23} = 2.4 \times 10^{-3}\,eV^2$ and $\sin^2 2\theta = 1$). Plots generated using 10a MC with a two flavour oscillation assumption.*

5.4 Multivariate Analysis Enhancement

Section 5.3.3 has shown how increasing the CCQE purity increases the sensitivity to oscillation. If the sensitivity is to be increased further then this is a possible route to explore. This section looks at the proposed method of using a non-linear multivariate approach to improve selection purity with the means of an artificial neural network (ANN). The neural network will take as its input a series of parameters which characterise the events and output a single response variable assigned to each event which represents the likelihood of that event being signal or background. Here signal is defined as CCQE and the background as all other interaction modes. A cut can then be made on this output variable to create the CCQE enhanced sample.

5.4.1 Multilayer Perceptron

For this study a multilayer perceptron (MLP) artificial neural network from ROOT's TMVA package [52] is used to separate signal and background. Artificial neural networks are formed from a collection of interconnected simulated neurons, objects which output a given numerical response to a specific set of input signals. In an MLP network, neurons are arranged in layers with each neuron in a given layer connected to all other neurons in the next layer with the exception of the last, as shown in figure 5.11. The MLP neural network in this study uses three layers. The first of these, the input layer, has n neurons which correspond to the n selected characterising input variables. Each neuron takes as its input one of the n variables normalised to $[-1, 1]$. The last layer, the output layer, has one neuron which gives as its output the response variable on which the cut is applied. In between these two is a hidden layer of neurons which connects the other two. This layer uses the TMVA default value of $n + 5$ neurons. The MLP neural network is a feed forward neural network in that information only passes in one direction *i.e.* from the input layer to the output layer.

Two factors control the response of the neural network to input: the weights given to the inter-neuron connections and the response of the neurons to input, described by the neuron response function ρ. The response function is inherent to the network and fixed at the start while the weights are calculated by training the network on Monte Carlo simulation events where the desired response of the network is known. This training method is known as back propagation.

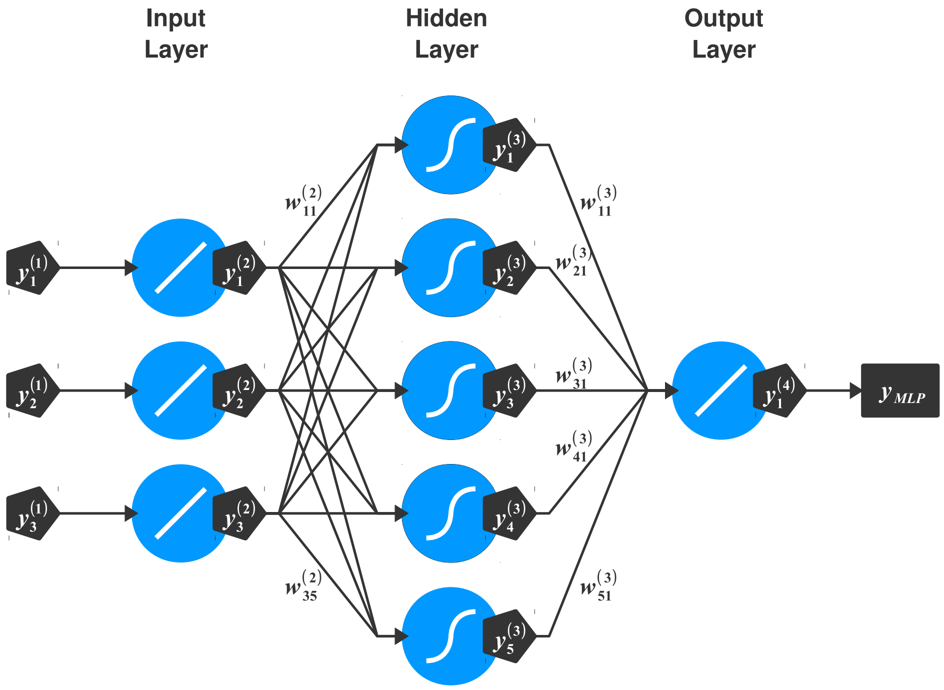

Figure 5.11: *Illustration of an MLP artificial neural network architecture. The blue circles represent the neurons arranged in three layers. Only neurons in the hidden layer have a non-linear response. Inputs to the neurons are marked by a y. Selected weights for the interconnections are shown with a w.*

The response function of a neuron maps the neuron's inputs to its output. The function consists of two parts convolved together, such that $\rho = \alpha \circ \kappa$ where α is known as the neuron activation function and κ as the synapse function. α and κ are defined for the j^{th} neuron in the l^{th} layer as follows:

$$\alpha(x) = \begin{cases} x & \text{for the first and last layer} \\ \tanh(x) & \text{for the hidden layer} \end{cases} \tag{5.5}$$

$$\kappa\left(y_1^{(l)}, \ldots, y_n^{(l)} \mid w_{1j}^{(l)}, \ldots w_{nj}^{(l)}\right) = \sum_{i=1}^{n^{(l)}} y_i^{(l)} w_{ij}^{(l)} \tag{5.6}$$

where $y_i^{(l)}$ is the i^{th} input to the neuron, $n^{(l)}$ is the total number of inputs and $w_{ij}^{(l)}$ is the weight of the connection between the i^{th} neuron of the $(l-1)^{th}$ layer and the neuron in question. In the case of the input layer, the weights are fixed at 1, meaning that the output is the same as the input. This is because the first layer exists only to feed input to the hidden layer. From equations 5.5 and 5.6 it can be shown that the output of the network (y_{MLP}) is given by

$$y_{MLP} = \sum_{j=i}^{n^{(3)}} y_j^{(3)} w_{j1}^{(3)} = \sum_{j=1}^{n^{(3)}} \tanh\left(\sum_{i=1}^{n^{(2)}} y_i^{(2)} w_{ij}^{(2)} \right) w_{j1}^{(3)}. \tag{5.7}$$

The set of weights in the network ($\mathbf{w}$) is randomly initialised. Training the network is done on an event by event basis such that the weights are updated with each event. To do this an error function E_a is defined for the a^{th} training event, such that

$$E_a(\mathbf{y}_a^{(1)} \mid \mathbf{w}^{(s)}) = \frac{1}{2}(y_{MLP,a} - \hat{y}_a)^2 \tag{5.8}$$

where $\mathbf{y}_a^{(1)} = \left(y_1^{(1)}, \ldots, y_n^{(1)}\right)$ is the vector containing values of the normalised input variables for the network, $\mathbf{w}^{(s)}$ is the set of weights for the current iteration, $y_{MLP,a}$ is the actual neural network output for the event a, while $\hat{y}_a$ is the desired output. For a true signal event the desired output is 1 and for a background event it is 0. The set of weights are adjusted by minimising the error function E using the method of steepest descent by moving a small distance in $\mathbf{w}$-space in the direction $-\nabla_{\mathbf{w}} E$ such that the new weights $\mathbf{w}^{(s+1)}$ are defined as follows:

$$\mathbf{w}^{(s+1)} = \mathbf{w}^{(s)} - \eta \nabla_{\mathbf{w}} E \tag{5.9}$$

where η is the learning rate which determines the step size of the minimisation. A value of 0.02 is used for this parameter.

The neural network is trained on half of the oscillated muon neutrino 10a Monte Carlo data that passes the zero or one decay-electron enhanced selection. The other half is used for testing. 500 training cycles are performed.

5.4.2 The Input Variables

Nine variables are used as the input to the neural network. The selection of these variables was optimised on their discriminating power. The signal to background separation of the variables is shown in figure 5.12. The variables are defined as follows:

1. **PID likelihood** The particle identification likelihood distribution generated during reconstruction which forms the basis of the muon-like cut.
2. **Cos$\boldsymbol{\theta_{ring}}$** The reconstructed angle of the ring with the neutrino beam direction.
3. **Ring counting likelihood** Distribution used in reconstruction to express the likelihood that an event is single-ring or multi-ring.
4. **$\boldsymbol{P_{ring}}$** The reconstructed momentum of the ring assuming a muon.
5. **$\boldsymbol{e}$ hits** The number of hit PMTs due to the decay-electron.
6. **$\boldsymbol{e}$ time** The timing of the decay-electron after the interaction.
7. **$\boldsymbol{e \to \nu}$ distance** Distance of the reconstructed decay-electron vertex to the neutrino interaction vertex.
8. **$\boldsymbol{e \to \mu_{stop}}$ distance** Distance of the reconstructed decay-electron vertex from the stopping point of a muon extrapolated from the ring direction (2) and momentum (4).
9. **$\boldsymbol{e}$ type** Events are divided into three types. The first is where no decay electron is observed, the second where the timing of the decay electron is too close to the neutrino interaction time that its vertex is not properly reconstructed and the third type refers to events with well reconstructed decay-electrons.

5.4.3 Optimizing the Cut

Figure 5.13 shows the separation of the CCQE from non-CCQE events as a function of the neural network response variable (y_{MLP}); Non-CCQE events

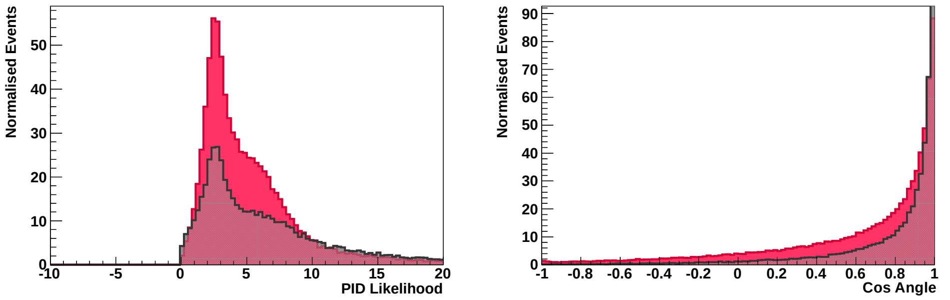

(a) *PID Likelihood* **(b)** $\cos\theta_{ring}$

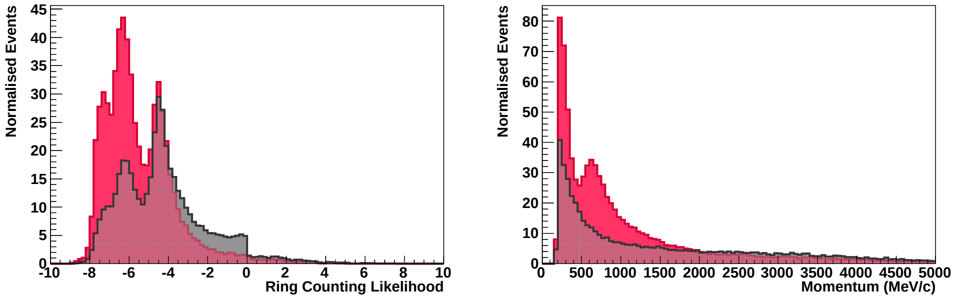

(c) *Ring counting likelihood* **(d)** P_{ring}

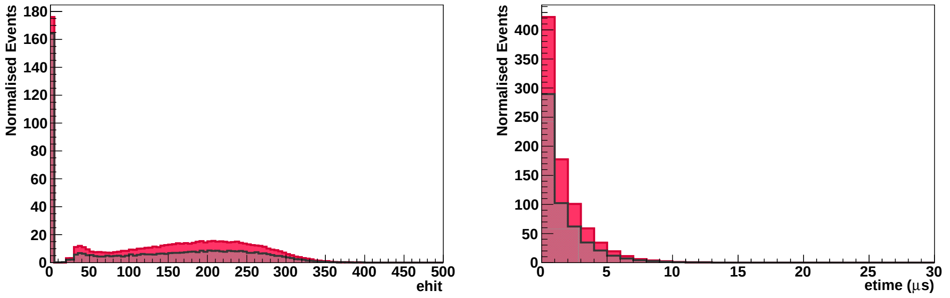

(e) *e hits* **(f)** *e time*

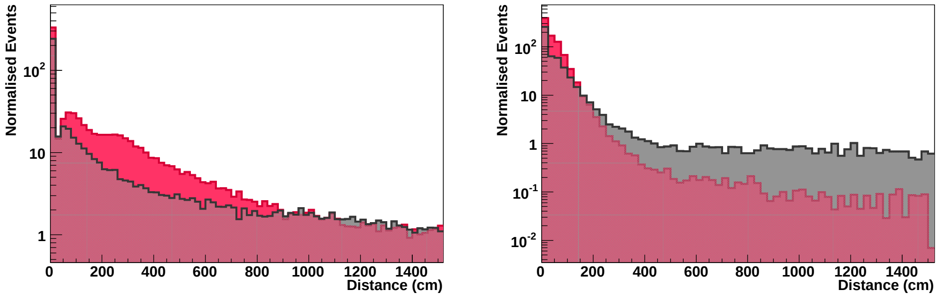

(g) $e \rightarrow \nu$ *distance* **(h)** $e \rightarrow \mu_{stop}$

Figure 5.12

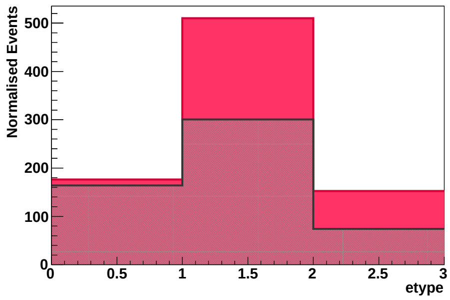

(i) *e type*

🟥 CCQE ▨ nonCCQE

Figure 5.12: *Signal and background distributions of the input variables to the MLP neural network for 1Rμ01DE events. Plots are generated from oscillated 10a MC data with 5 year normalisation (8.33×10^{21} POT).*

tend to have a negative value while CCQE events predominantly occupying the more positive half of the distribution.

The value on which a cut is made is based on consideration of the significance, where significance is defined as signal/$\sqrt{\text{background}}$. The significance of making a cut at each MLP response value is shown on figure 5.13. The point of maximum significance is chosen for the cut, corresponding to a value of 0.1, as illustrated.

5.4.4 Energy Resolution

Figures 5.14 and 5.15 show the energy spectra, resolution and percentage shift plots for the single muon-like ring sample with the additional zero or one decay-electron cut and MLP cut applied (1Rμ01DEMLP). It can be seen that for this MLP enhanced selection the energy resolution has slightly improved as a result of the increase in CCQE purity. This improvement is largely confined to the 500 → 1000 MeV region. The energy shift has remained largely the same.

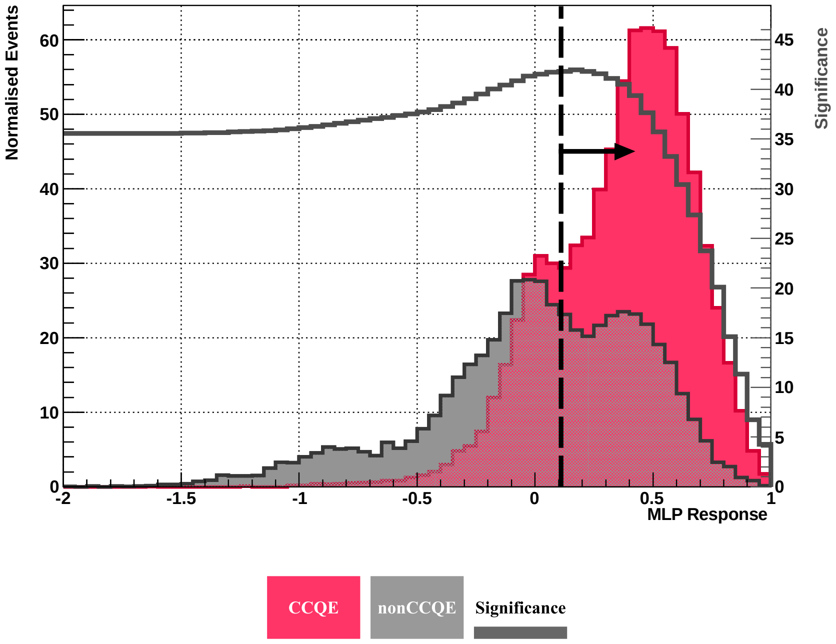

Figure 5.13: *MLP response for 1Rμ01DE events showing separation of CCQE and non-CCQE events. Significance of selection surving cut as a function of MLP response is also shown, where significance is defined as signal/$\sqrt{background}$. Plot is generated from oscillated 10a MC for a nominal running period of 5 years (8.33×10^{21} POT).*

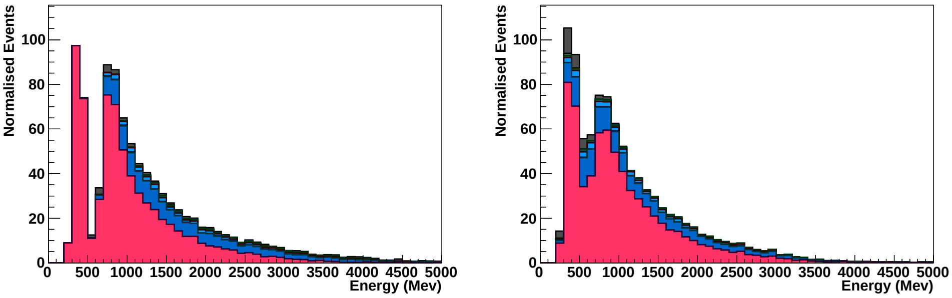

(a) *True Neutrino Energy* **(b)** *Reconstructed Neutrino Energy*

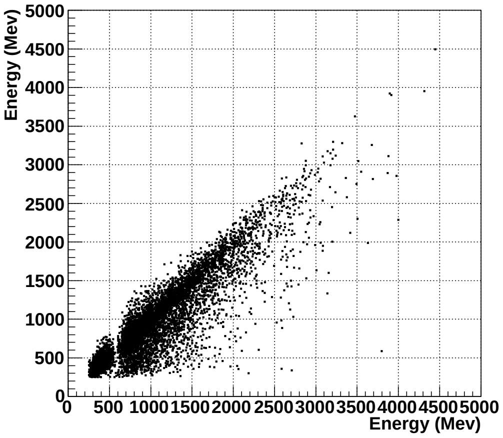

(c) *Reconstructed Vs. True Neutrino Energy*

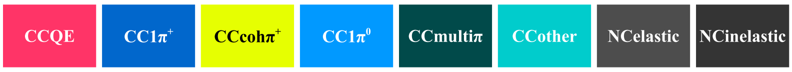

(d) *Interaction Mode Key*

Figure 5.14: *The effects of reconstruction on the neutrino energy spectrum for 1Rμ01DEMLP events. 5.14a shows the true energy spectrum, while 5.14b shows the reconstructed spectrum assuming CCQE (equation 5.2). 5.14c shows events plotted as a function of reconstructed and true neutrino energy. Plots are generated from oscillated 10a MC data with 5 year normalisation (8.33 × 10^{21} POT) and are broken down by interaction mode.*

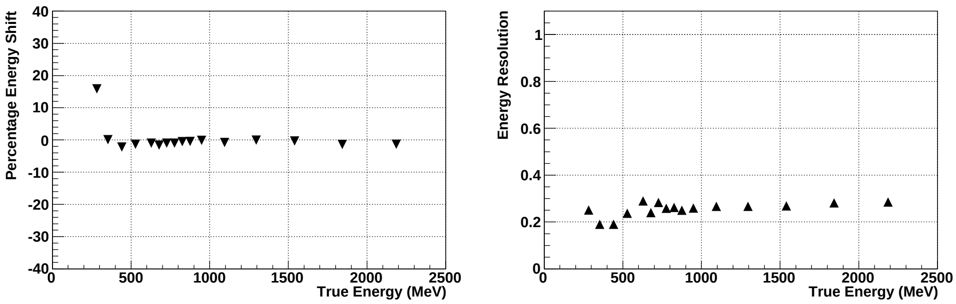

(a) *Percentage Energy Shift* **(b)** *Energy Resolution*

Figure 5.15: *Energy resolution and peak energy shift as a function of true neutrino energy for 1Rμ01DEMLP events. The figures are generated using oscillated 10a MC.*

5.4.5 Systematic Errors

As the MLP based selection is a subset of the zero or one decay-electron enhanced selection, the approach used in section 5.3.2 can equally be applied to this selection with the inclusion of a further systematic term coming from the MLP cut.

The MLP systematic term is derived by considering the systematic uncertainty on all the input variables of the events. This approach is implemented by smearing the values of the variables in the Monte Carlo simulation by the corresponding uncertainty and then evaluating the MLP response to the smeared input. The difference in the number of events passing the cut for smeared and unsmeared inputs is used to evaluate the systematic uncertainty (σ_{MLP}) *i.e.*:

$$\sigma_{MLP} = \frac{N_{smeared} - N_{unsmeared}}{N_{smeared}} \tag{5.10}$$

The uncertainty in each variable distribution is calculated independently of one another yet needs to be applied in a correlated manner where the correlation mimics the correlation of the initial variables. This is achieved using the Cholesky decomposition method [53].

A square symmetric positive-definite matrix (**C**) can be decomposed into a lower triangular matrix (**L**) and its transpose:

$$\mathbf{C} = \mathbf{L} \cdot \mathbf{L}^{\mathbf{T}} \tag{5.11}$$

For a system (S) with N dimensions a covariance matrix (**C**) can be generated and decomposed with the Cholesky method. If **u** is a N-dimensional vector of uncorrelated variables generated from a gaussian distribution with a mean of 0 and standard deviation of 1 then the vector **x** defined by:

$$\mathbf{x} = \mathbf{L} \cdot \mathbf{u} \tag{5.12}$$

has the same covariance properties as S_N. By modifying the standard deviation used in **u**, a vector **x** can be created which has the covariance properties required to smear the input variable values. As such, a set of uncorrelated systematic shifts can be applied in a correlated manner.

The uncertainties in the nine variable distributions are taken largely from studies using atmospheric neutrino data and cosmic stopping-muon data taken by Super-Kamiokande. The methods are detailed below. A summary of the values is given in table 5.4.

1. PID Likelihood

The PID likelihood is assigned an uncertainty of 0.8%. This systematic is from the uncertainty on the μ-like cut as evaluated by Kameda and Wendell [48] and discussed in section 5.2.2.

2. Cosθ_{ring}

The ring direction is evaluated with the same fitter as the interaction vertex. Kameda and Wendall [48] calculate a 5 cm systematic error on the vertex position. This can be used to make an estimate of the ring direction uncertainty. The reconstructed vertex is Gaussian smeared in Monte Carlo simulation by 5 cm and then the original angle is compared with the new one under the assumption that the detector wall intercept position remains constant. In this manner a systematic error of 0.1% is calculated.

3. Ring counting likelihood

The ring counting likelihood is assigned an 8.9% uncertainty derived from the single-ring cut systematic study by Kameda and Wendell [48].

4. P_{ring}

An uncertainty of 2.3% is assigned to the reconstructed ring momentum. The value is taken from a study on the energy scale error by Otani and Kameda using stopping-muon events [49].

5. e hits

No direct study of the systematic uncertainty for the e hit distribution has been performed by the Super-Kamiokande however, the decay-electron momentum spectrum was assigned a 2.0% systematic based on a study of stopping-muon data and Monte Carlo [35]. Given that the momentum depends on the number of PMTs fired, a 2.0% error is assigned as an estimate to the e hit distribution.

6. e time

Similar to e hit, no dedicated study has been performed by the Super-Kamiokande collaboration to evaluate the systematic uncertainty on the e time distribution. A systematic is estimated from a timing resolution study of the ID-PMTs carried out using a laser source [54]. The time resolution was calculated as being ~ 2.5 ns for 1 p.e./PMT. The e time distribution is on the order of 1 μs making the uncertainty $\ll 1\%$. An error of 1% is assigned as the estimate for the total uncertainty.

7. $e \rightarrow \nu$ distance

The fitted interaction vertex has a systematic error of 5 cm assigned to it [48]. The decay electron vertex is fitted with a different vertex fitter which only uses timing information of the PMT hits. From the study by Kameda and Wendell [48], 11 cm is given as the maximum difference between atmospheric neutrino data and Monte Carlo simulation for the separation of the two vertex fitters as applied to the same event. Therefore, 16 cm $(11 + 5)$ can be assigned as the systematic error in the position of the decay-electron vertex. Using these two errors, the uncertainty on the distance between the interaction vertex and the decay-electron can be estimated by Gaussian smearing the vertices of a Monte Carlo simulated sample by their error and then calculating the new distance. The percentage difference between the smeared and unsmeared distance is used to estimate the uncertainty. A value of 0.6% is assigned.

8. $e \rightarrow \mu_{stop}$ distance

For the systematic uncertainty in the distance between the muon stopping point and the decay-electron vertex a similar method as discussed for the interaction vertex to decay electron vertex distance can be used. This distance is dependent on two further inputs: the ring direction and the ring momentum, which have already been assigned an uncertainty. As before a Monte Carlo simulated sample is used with smearing applied to the vertices and the muon range inputs and a new muon stopping point to decay-electron vertex is calculated. Comparison with the unsmeared variable gives a systematic uncertainty of 1.6%.

9. e type

e type is a composite variable based on e time and the number of decay-electrons. The smeared e time distribution is used to create the smeared e type distribution.

Total Error

Using the Choleksy decomposition method and equation 5.10 an error of 2.2% is assigned to the MLP cut. When combined in quadrature with the other re-weighted cut based systematics a total error of 11.5% is generated as shown in table 5.5. The cross-section systematic uncertainties remain the same as discussed in 5.2.2 but weighted by the new interaction mode composition of the selection.

Variable	Systematic Uncertainty
1) PID	0.8%
2) Cosθ_{ring}	0.1%
3) Ring Counting	8.9%
4) P_μ	2.3%
5) e hits	2.0%
6) e time	1.0%
7) $e \rightarrow \nu$ distance	0.6%
8) $e \rightarrow \mu_{stop}$ distance	1.6%
9) e type	2.0%

Table 5.4: *Systematic uncertainties on MLP input parameters.*

Cuts	1Rμ	1Rμ01DE	1Rμ2DE	1Rμ01DEMLP
Good spill	1%	1%	1%	1%
FC	1%	1%	1%	1%
FV	1%	1%	1%	1%
1R	9.3%	8.6%	18.6%	7.4%
μ-like	6.3%	6.8%	1.6%	3.4%
DE	-	1%	1%	1%
MLP	-	-	-	2.2%
Total	11.3%	11.1%	18.8%	8.7%

Table 5.5: *Summary of detector and reconstruction systematic error estimation for the MLP enhanced selection compared to other selections. Errors are added in quadrature to produce the totals.*

5.4.6 Sensitivity

Figure 5.16b shows the sensitivity to oscillation of the MLP enhanced selection compared to both the zero or one decay-electron enhanced selection and the single muon-like ring selection. The MLP selection performs significantly better than the other two due mainly to the removal of the non-CCQE interaction modes which reduces the systematic uncertainty.

Figure 5.16a shows the sensitivity for the 5 year case. Here an improvement is still observed but due to the expected reduction in the non-CCQE cross-section errors the relative gain is diminished with respect to the other selections.

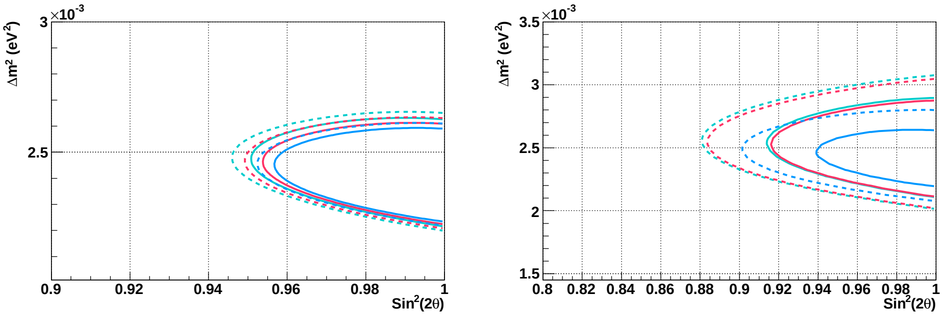

(a) *5 Years* **(b)** *Runs 1 and 2*

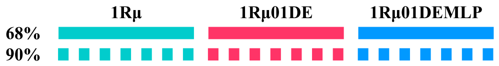

(c) *Confidence level*

Figure 5.16: *Sensitivity of the 1Rμ01DEMLP sample to oscillation for a nominal 5 years of physics running (8.33×10^{21} POT) and for runs 1 and 2 (1.45×10^{20} POT) created using a χ^2 map. Contours define regions of parameter space with a stated maximum confidence of finding the test parameter values ($\Delta m^2_{23} = 2.4 \times 10^{-3} eV^2$ and $\sin^2 2\theta = 1$). Plots generated using 10a MC with a two flavour oscillation assumption.*

5.5 Summary

Two newly proposed event selections have been evaluated: the MLP enhanced selection and the use of the two decay-electron sub-sample with the zero or one decay electron sub-sample. For both the period up to the end of run 2 and for the 5 year case, the MLP enhanced selection gives the best performance of all the studied selections, though this gain in sensitivity relative to the zero or one decay-electron enhanced selection is smaller when considered over the 5 year running period. The use of two decay-electron enhanced selection has been shown not to improve the sensitivity of the measurement for either running period.

Table 5.6 shows a summary of expected sample sizes for the discussed selections.

		5 Years		Run 1 and 2			
	Signal Mode	Signal Events	Total Events	Signal Events	Total Events	Sig. Eff.	Sig. Purity
True FV	CCQE	1165.5	6984.6	20.3	121.6	-	-
True FV	CC1π^+	843.6	6984.6	14.68	121.6	-	-
1Rμ	CCQE	846.3	1551.3	14.7	27.0	72.6%	54.6%
1Rμ01DE	CCQE	837.9	1377.0	14.6	24.0	71.9%	60.9%
1Rμ2DE	CC1π^+	91.8	160.2	1.6	2.8	10.9%	57.3%
1Rμ01DEMLP	CCQE	660.4	909.8	11.5	15.8	56.6%	72.6%

Table 5.6: *Summary of various sample statistics for both a nominal 5 year run (8.33×10^{21} POT) and for a period equivalent to runs 1 and 2 (1.45×10^{20} POT). True FV refers to events which have their true interaction vertex in the fiducial volume. Efficiency is calculated relative to the true FV sample. Statistics generated from muon neutrino 10a MC.*

Chapter 6

Analysis of Run 1-2 Data

A total of 88 events pass the fully contained fiducial volume pre-selection (section 4.4.3) for runs 1 and 2 data and can be used for physics analysis. This chapter presents key data distributions and, where applicable, comparison to Monte Carlo simulation. The second part of the chapter contains results for the measurement of the oscillation parameters Δm^2_{32} and $\sin^2 2\theta_{23}$ with this data.

6.1 Data to Monte Carlo Simulation Comparison

The following is a comparison of the 88 fully contained fiducial volume events with the 10a Monte Carlo prediction. For the most part plots are made using only muon neutrino Monte Carlo simulation, *i.e.* where only charged current muon neutrino interactions and neutral current tau and muon neutrino interactions are modelled. Electron neutrino interactions from oscillated muon neutrinos are not considered. For sample size comparisons neutrino interactions from intrinsic electron neutrino and anti-muon neutrino beam contamination are also considered. Events from intrinsic electron neutrinos are expected to account for less than 1% of the size of the samples put forward for physics analysis in chapter 5, *i.e* the single muon-like ring selection and samples based on it, while events from anti-muon neutrinos are expected to account for around 10% of the total of these samples. The Monte Carlo simulation is normalised to the number of delivered POT for runs 1 and 2 (1.43×10^{20} POT).

6.1.1 Single Muon-Like Ring Selection

A total of 33 events survive the single ring muon-like selection. Figure 6.1 shows plots taken from a T2K technical note by Otani and Kameda [49] which looks at the basic event reduction for the muon disappearance analysis. The distributions shown are for the reconstructed variables that are cut on to create the single muon-like ring sample, *i.e.* the number of reconstructed rings and the particle ID likelihood attributed to the most energetic ring. The recorded data is overlaid onto the Monte Carlo simulation.

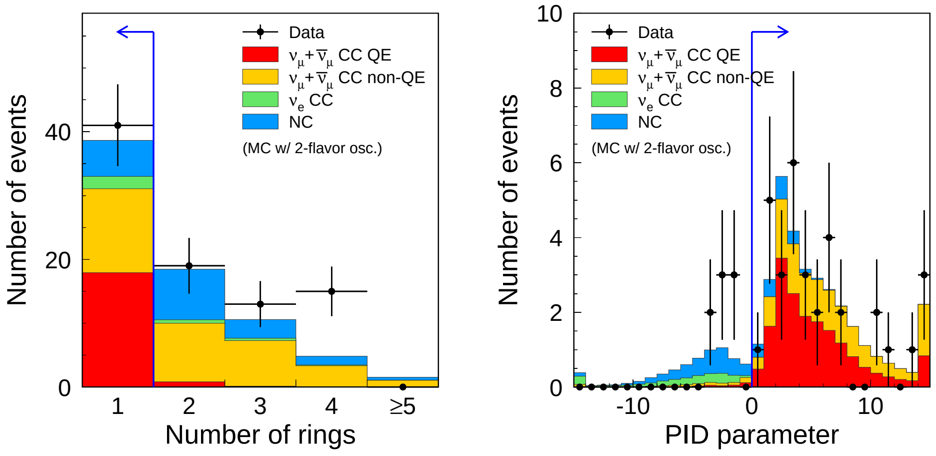

(a) **(b)**

Figure 6.1: *Data MC comparison of distributions used to make the 1Rμ selection. 6.1a shows the number of reconstructed rings for FCFV events while 6.1b shows the particle ID likelihood for FCFV1R events. Events with a positive likelihood are classified as muon-like; negative likelihood events are classified as electron-like. Plots are generated from oscillated 10a MC normalised to run 1-2 exposure* (1.43×10^{20} *POT) with observed data overlaid with black markers. The blue lines mark the cuts made on the distributions. Plots taken from [49].*

Two areas of disagreement can be seen between data and Monta Carlo for the cut distributions. A multi ring excess is observable in figure 6.1a. This is not presently understood and is under investigation. However, it does not impact the single-ring study. An excess is also observed for single electron-like ring events as shown in figure 6.1b. This excess is the signal for muon neutrino to electron neutrino oscillation as discussed in the T2K electron neutrino appearance paper [55].

Figure 6.2 shows the reconstructed energy spectrum of the surviving events for both data and Monte Carlo simulation.

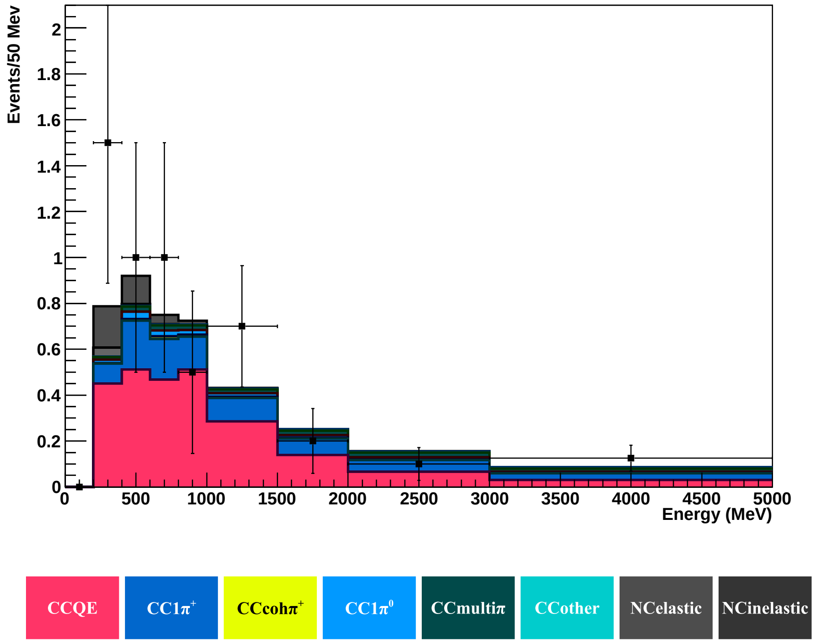

Figure 6.2: *Data MC comparison of reconstructed energy spectrum for 1Rμ events. The figure is generated using oscillated 10a MC normalised to run 1-2 exposure (1.43 × 10^{20} POT) with the observed data overlaid with black markers.*

6.1.2 Zero or One Decay-Electron Sub-Sample

Figure 6.3 shows the data Monte Carlo comparison of the decay-electron distribution of the single muon-like ring events from which the zero or one decay-electron sub-sample is selected. 31 events survive the cut. Figure 6.4 shows the number of events surviving each stage of this selection for both data and Monte Carlo expectation. Good agreement is observed with the exception of the initial fully contained fiducial volume (FCFV) selection where as discussed in section 6.1.1 the multi-ring excess and electron-neutrino appearance cause Monte Carlo expectation to be below observed statistics.

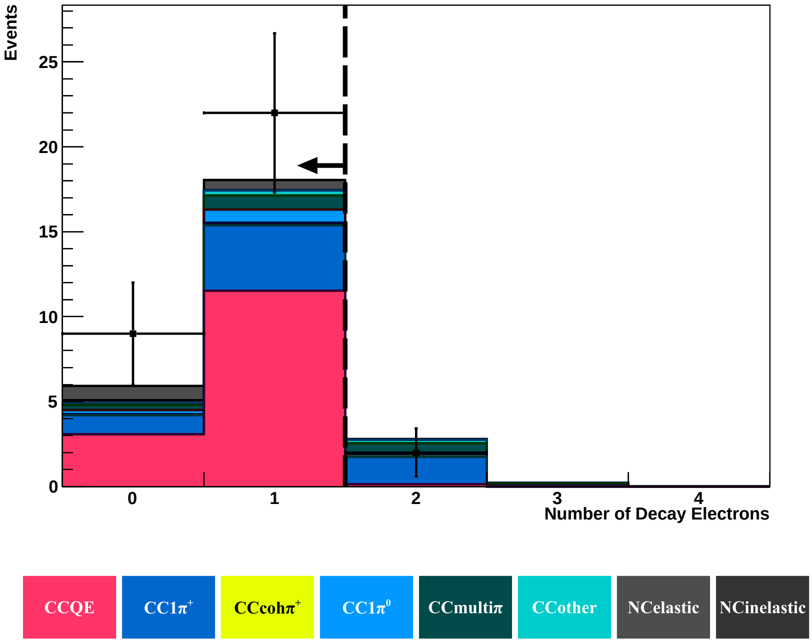

Figure 6.3: *Data MC comparison of number of observed decay electrons for 1Rμ events. The figure is generated using oscillated 10a MC normalised to run 1-2 exposure (1.43 $\times$ 10^{20} POT) with the actual data overlaid with black markers. Black dashed lines mark the cuts made on the distributions.*

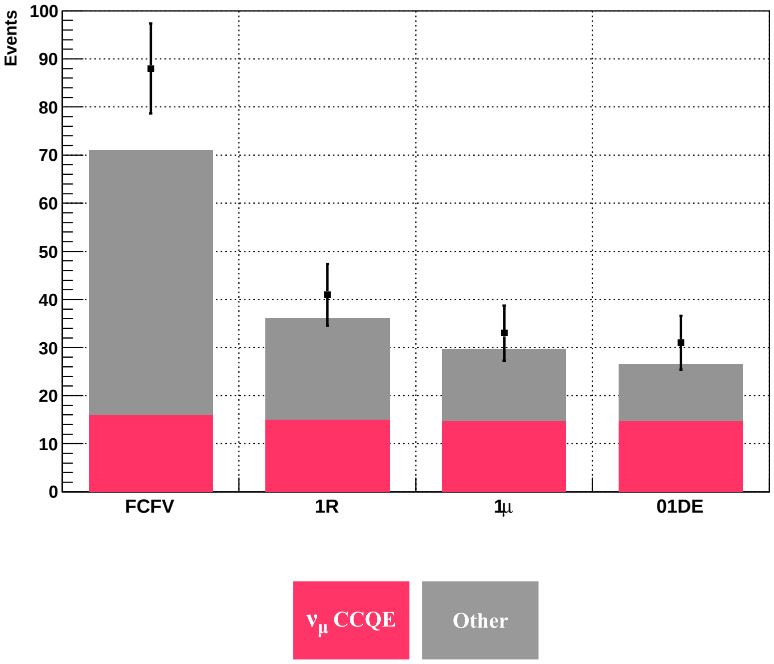

Figure 6.4: *Data MC comparison of number of events surviving each cut of the 1Rμ01DE selection separated into the signal muon neutrino CCQE events (pink) and non-CCQE muon neutrino events and events from other neutrino species (grey). Plot is generated from oscillated* ν_μ*,* $\bar{\nu}_\mu$ *and intrinsic* ν_e *10a MC normalised to run 1-2 exposure (1.43 ×* 10^{20} *POT) with observed data overlaid with black markers.*

Figure 6.5 shows the location of the reconstructed vertices of the surviving events in the inner detector. A uniform distribution is observed throughout the inner detector as expected.

The data to Monte Carlo comparison of the variables required for the energy reconstruction are shown in figure 6.6 along with the reconstructed energy itself. The distribution of data points is not inconsistent with Monte Carlo expectation.

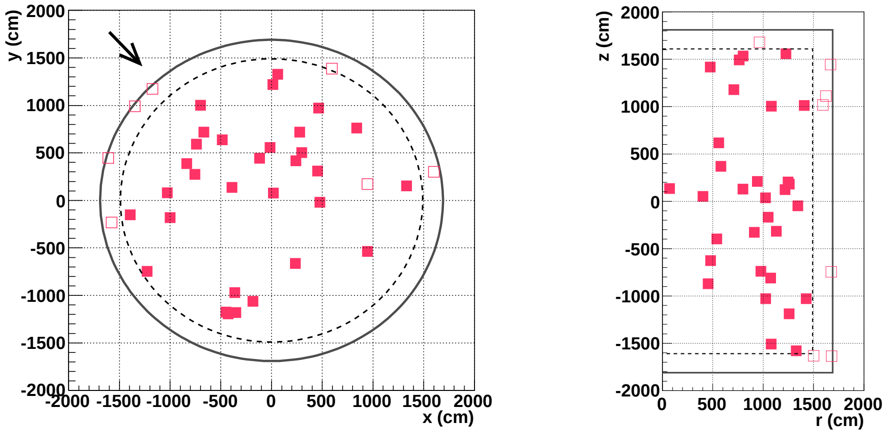

(a) *y-x projection* **(b)** *z-r projection*

Figure 6.5: *The vertex positions of run 1-2 1Rμ01DE events within the inner detector. Figure 6.5a shows the y-x projection of the tank while figure 6.5b shows the z-r projection where z is the vertical position and r the radial position in cylindrical co-ordinates. The hollow data points are for events which pass all selection cuts except the fiducial volume cut (shown as a dashed line). The arrow in figure 6.5a indicates the beam direction.*

6.1.3 Multivariate Analysis Enhancement

Figure 6.7 shows the data MC comparison for the distributions which are used as inputs for the MLP multivariate analysis, as discussed in section 5.4, while table 6.1 shows the Kolmogorov-Smirnov agreement between data and Monte Carlo for these distributions.

While most of the MLP input variables show good agreement with Monte

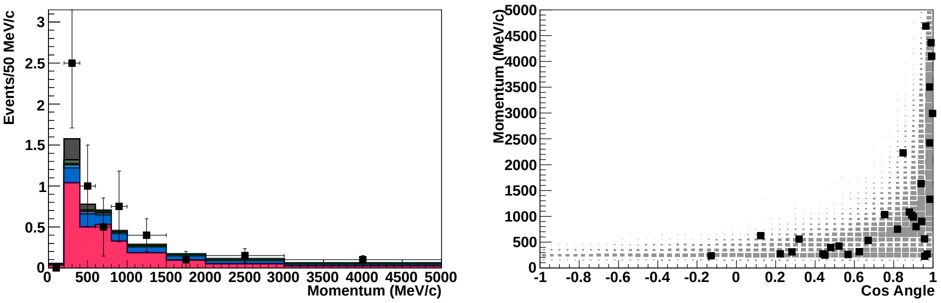

(a) P_{ring} **(b)** P_{ring} *vs.* $\cos\theta_{ring}$

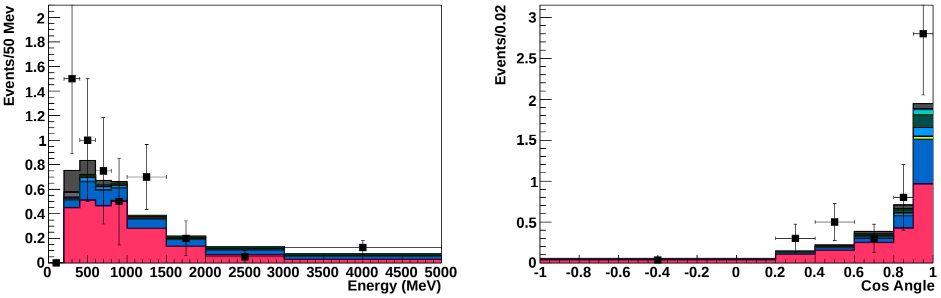

(c) E_ν **(d)** $\cos\theta_{ring}$

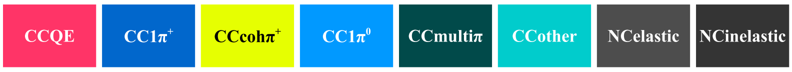

(e) *Interaction Mode Key*

Figure 6.6: *Data MC comparison of energy spectrum variables for 1Rμ01DE events. 6.6a and 6.6d show the reconstructed momentum and angle from the beam direction of the ring, while 6.6b shows the relationship bewteen them. The reconstructed energy spectrum is shown in 6.6c. Plots are generated from oscillated 10a MC normalised to run 1-2 exposure (1.43 × 10^{20} POT) with observed data overlaid with black markers.*

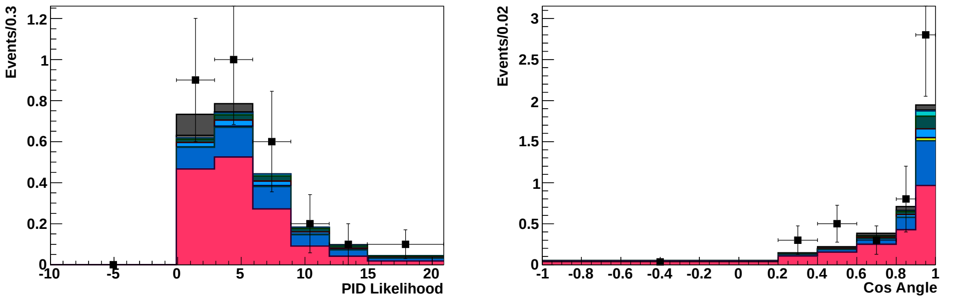

(a) *PID Likelihood* **(b)** $\cos\theta_{ring}$

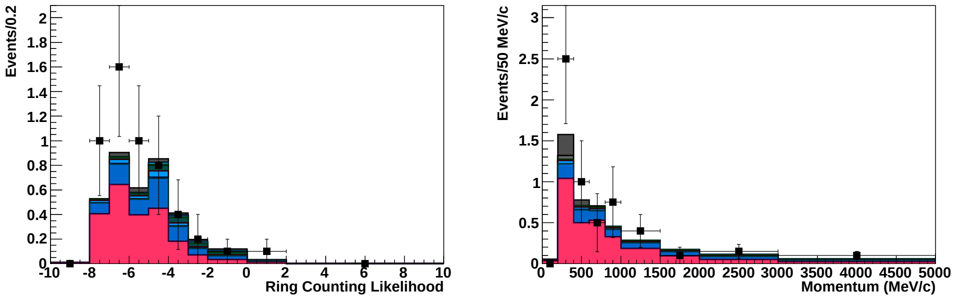

(c) *Ring counting likelihood* **(d)** P_{ring}

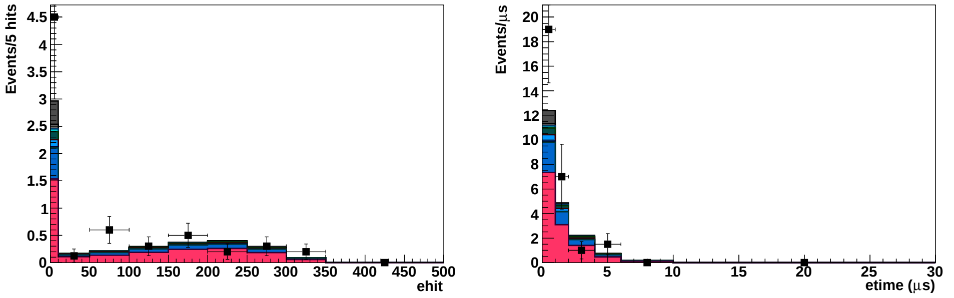

(e) *e hits* **(f)** *e time*

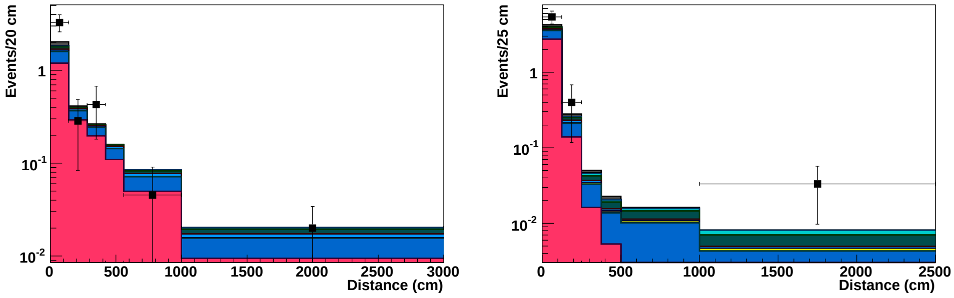

(g) $e \to \nu$ *distance* **(h)** $e \to \mu_{stop}$

Figure 6.7

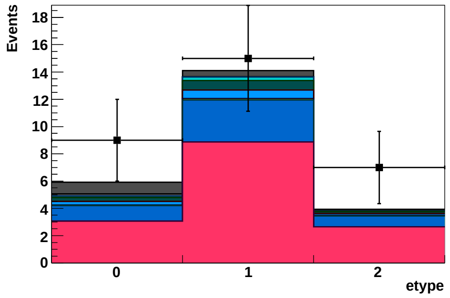

(i) *e type*

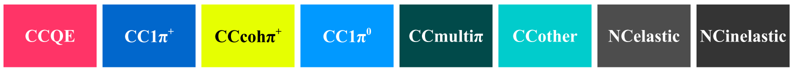

(j) *Interaction Mode Key*

Figure 6.7: *Data MC comparison of the 1Rμ01DE input distributions for the MLP neural network. Plots are generated from oscillated 10a MC normalised to run 1-2 exposure (1.43 $\times$ 10^{20} POT) with observed data overlaid with black markers.*

Variable	K-S Test P-values
1) PID	99.9%
2) Cosθ_{ring}	98.4%
3) Ring Counting	60.9%
4) P_{ring}	99.6%
5) e hits	35.0%
6) e time	77.3%
7) $e \to \nu$ distance	16.4%
8) $e \to \mu_{stop}$ distance	99.2%

Table 6.1: *Kolmogorov-Smirnov test results showing agreement between data and MC prediction for the continous MLP input distribiutions for 1Rμ01DE events, as shown in figure 6.7.*

Carlo expectation there are a few cases where agreement is not as good as expected, primarily concerning the variables based on reconstructed decay-electrons. Two distributions have apparent outlying events in their tails. These are the two decay-electron based distance variables. The distance of the decay-electron vertex to the interaction vertex (figure 6.7g) has 3 events with a distance of over 500 cm while the distance of the decay-electron from the outgoing muon stopping point (figure 6.7h) shows 2 events. Calculating the Monte Carlo expectation for these tails shows statistical consistency with data, with figures 6.7g and 6.7h having an expectation of 4.32 and 0.84 events respectively. For the Kolmogorov-Smirnov test two distributions have low P values. These are the e hits distribution and the again the decay-electron distance from the interaction vertex distribution. It is possible that these cases are due to the low statistics of the sample and, for the decay-electron distance from the interaction vertex, the tail events. However, it could also be indicative of a poor understanding of these distributions and consequently underestimated systematic error contributions.

Figure 6.8 shows the MLP response curve of the data with Monte Carlo comparison. Monte Carlo data agreement is poorer than expected for this distribution, again symptomatic of some of the input distributions being poorly understood. Resolution of this discrepancy can be achieved with a study using a non-signal high statistics neutrino interaction sample such as that used in the Super-Kamiokande atmospheric neutrino analyses [54]. If it is found that the discrepancies persist with higher statistics studies then the choice of variables will need to be reassessed with some of the distributions removed as inputs to the MLP if the systematic error cost becomes too high to justify their inclusion in the neural network.

A cut is made at 0.1 on the MLP output distribution. Of the 31 input events, 15 events survive this selection. Figure 6.9 shows the number of events surviving each stage of the selection for both data and Monte Carlo expectation while figure 6.10 shows the reconstructed vertex locations of the events passing the final selection. As with the zero or one decay electron enhanced selection, no biasing is seen in the vertex positions within the inner detector. Figure 6.11 shows an example of an event passing the MLP selection criteria on the Super-Kamiokande event display.

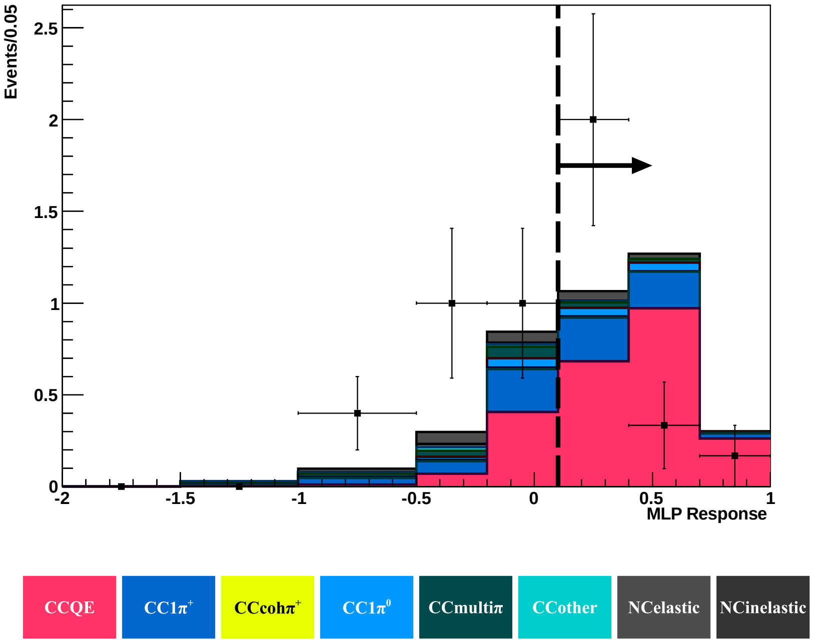

Figure 6.8: *Data MC comparison of MLP response for 1Rμ01DE events. The figure is generated using oscillated 10a MC normalised to run 1-2 exposure (1.43 × 10^{20} POT) with the actual data overlaid with black markers. The black dashed line marks the cut made on the distribution.*

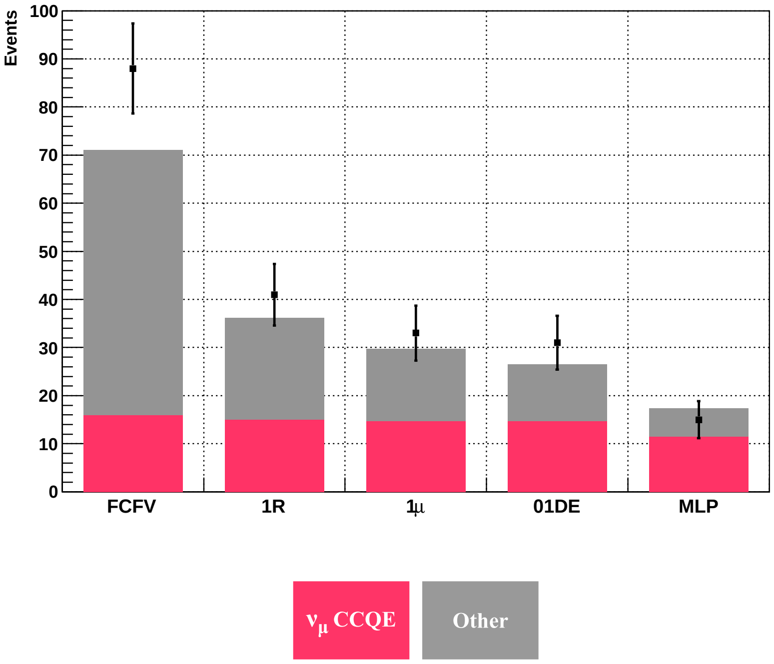

Figure 6.9: *Data MC comparison of number of events surviving each cut of the 1Rμ01DEMLP selection separated into the signal muon neutrino CCQE events (pink) and non-CCQE muon neutrino events and events from other neutrino species (grey). Plot is generated from oscillated* ν_μ*,* $\bar{\nu}_\mu$ *and intrinsic* ν_e *10a MC normalised to run 1-2 exposure (*1.43×10^{20} *POT) with observed data overlaid with black markers.*

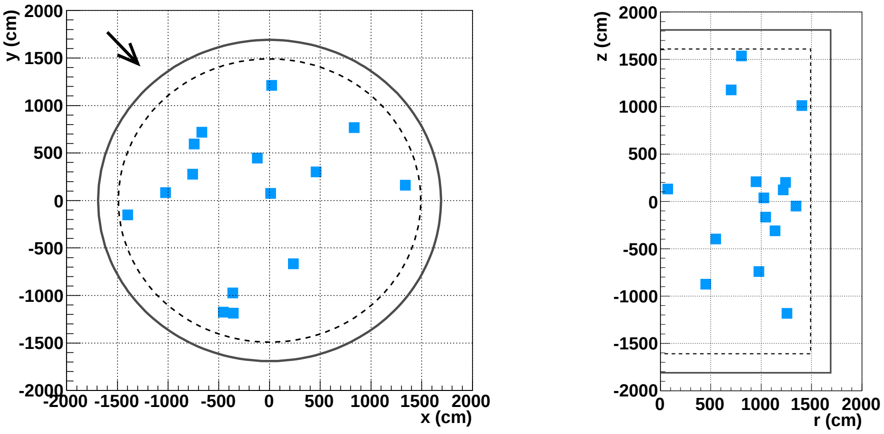

(a) *y-x projection* **(b)** *z-r projection*

Figure 6.10: *The vertex positions of run 1-2 1Rμ01DEMLP events within the inner detector. Figure 6.10a shows the y-x projection of the tank while figure 6.5b shows the z-r projection where z is the vertical position and r the radial position in cylindrical co-ordinates. The fiducial volume cut is shown as a dashed line. The arrow in figure 6.10a indicates the beam direction.*

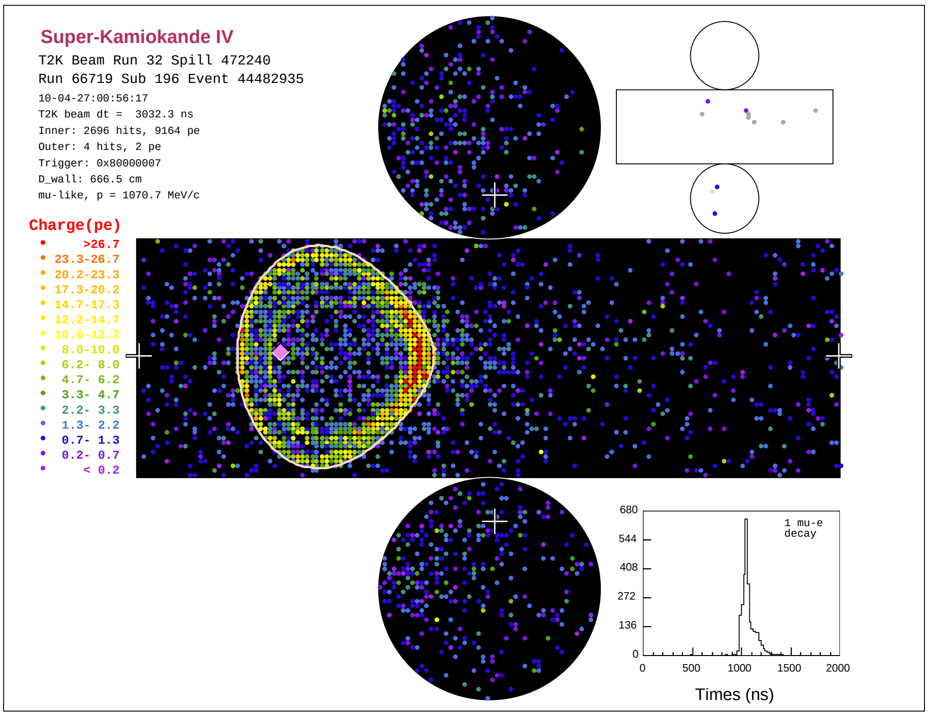

Figure 6.11: *An event display of a 1Rμ01DEMLP event with a reconstructed muon momentum of 1071 MeV/c. The bigger panel shows an unrolled view of the inner detector and the smaller one is that of the outer detector. Coloured points indicate location of the hit PMTs with the colour corresponding to their integrated charge (p.e.) ranges. Four white crosses represent vertex position. The left-right pair shows its height and the top-bottom pair shows its horizontal position. The circle line shows the fitted Cherenkov ring. The pink diamond is placed on the wall in the beam direction starting from the reconstructed vertex. The bottom-right figure is the hit timing distribution with information of the number of the tagged muon-decay electrons.*

The variables used for energy reconstruction and the energy spectrum itself for MLP selected events are shown compared to Monte Carlo expectation in figure 6.12. The agreement between Monte Carlo expectation and data is not as consistent as it is for the single moun-like ring selection. Again, this is likely due to the MLP cut distribution suffering from poorer than expected agreement between data and Monte Carlo prediction.

6.1.4 Summary

Table 6.2 shows a summary of the number of events surviving the cuts for the above discussed samples for runs 1-2 data and Monte Carlo expectation. Properties of the data events are consistent with expectations for samples up to the single muon-like ring selection. The MLP neural network output variable does not perform as well as expected, although the final sample size is consistent with expectation.

	MC Expectation	Observed
FCFV	71.2	88
1R	36.2	41
μ	29.7	33
01DE	26.6	31
MLP	17.4	15

Table 6.2: *Event numbers surviving each progressive cut for runs 1-2 data and corresponding MC prediction. MC statistics are generated from oscillated ν_μ, $\bar{\nu}_\mu$ and intrinsic ν_e 10a MC normalised to run 1-2 exposure (1.43×10^{20} POT).*

6.2 Oscillation Measurement with Run 1-2 Data

In this section results are presented for the oscillation parameter measurement performed with the newly introduced MLP enhanced selection comparing it to the zero or one decay electron enhanced selection and the parent single muon-like ring selection. Although not a full oscillation analysis, the results give a good expectation of what would be measured when used in a full treatment.

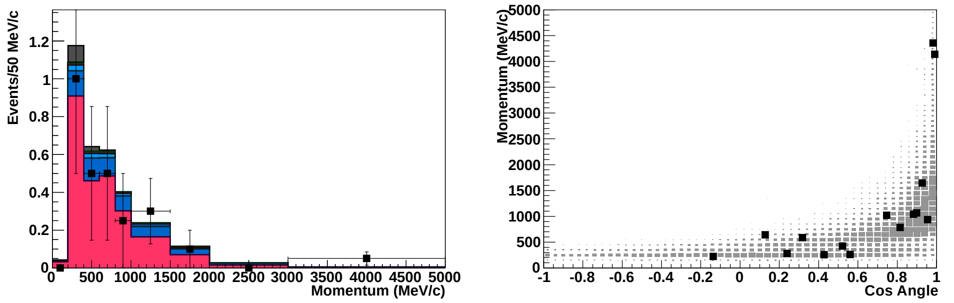

(a) P_{ring}

(b) P_{ring} *vs.* $\cos\theta_{ring}$

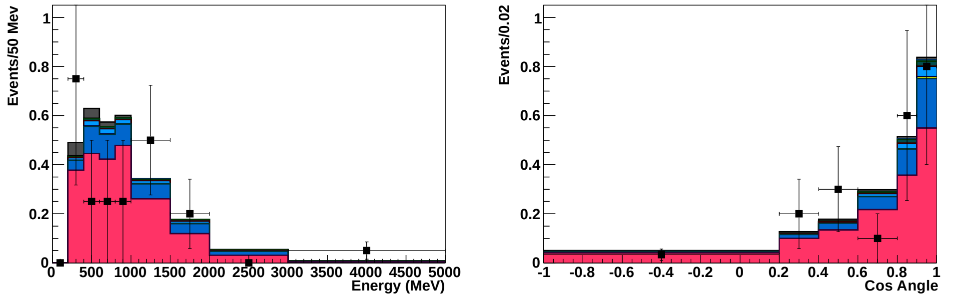

(c) E_{ν}

(d) $\cos\theta_{ring}$

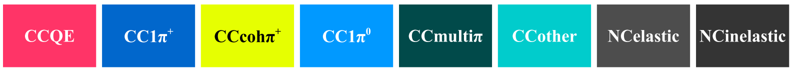

(e) *Interaction Mode Key*

Figure 6.12: *Data MC comparison of energy spectrum variables for 1Rμ01DEMLP events. 6.12a and 6.12d show the reconstructed momentum and angle from the beam direction for the ring, while 6.12b shows the relationship bewteen them. The reconstructed energy spectrum is shown in 6.12c. Plots are generated from oscillated 10a MC normalised to run 1-2 exposure (1.43×10^{20} POT) with observed data overlaid with black markers.*

This analysis is also presented in a T2K technical note [56].

The analysis is performed, as with the sensitivity expectations, using a χ^2 minimisation (equation 5.1). Here, n_{obs} becomes the data set and n_{exp} is again the Monte Carlo expectation for each point in parameter space. Systematic errors and cross-section uncertainties for Super-Kamiokande are again included. The selections have systematic errors of 11.3%, 11.1% and 8.7% for the single muon-like ring, zero or one decay-electron enhanced and MLP enhanced selections respectively (see table 5.5). The cross-section uncertainties are shown in table 5.2 and figure 5.3.

Figure 6.13 shows the energy bins used for the χ^2 sum for each sample. The binning was optimised on Monte Carlo simulation prior to examination of the data to ensure that no bin dropped too far below five events such that the χ^2 method remained valid, with the additional consideration that each bin should be sensitive to oscillation *i.e.* no very low energy or high energy bins were created.

The results from the oscillation fit are shown as a confidence plot in figure 6.14 with the extracted best fit values and errors presented in table 6.3.

Selection	$\Delta m^2_{23}[\times 10^{-3}\text{ eV}^2]$	$\sin^2 2\theta_{32}$
1Rμ	$2.68^{+0.42}_{-0.48}$	$0.957^{+0.043}_{-0.081}$
1Rμ01DE	$2.63^{+0.42}_{-0.43}$	$0.969^{+0.031}_{-0.075}$
1Rμ01DEMLP	$2.68^{+0.12}_{-0.18}$	$0.999^{+0.001}_{-0.009}$

Table 6.3: *Best-fit values of the run 1-2 oscillation parameter fit with* 1σ *errors for different selections.*

The confidence region of the three samples show a similar pattern to the expected sensitivity (figure 5.16b) with the exception of the MLP enhanced sample which shows a much tighter confidence region than expected. This tighter contour is due to the second bin of the MLP enhanced selection's energy spectrum containing only 1 event. This is caused either by a statistical fluctuation or poor understanding of the input variables to the MLP neural network leading to inappropriate energy binning. A bin entry of 1 means the validity of the χ^2 is reduced and the uncertainty underestimated. The use of

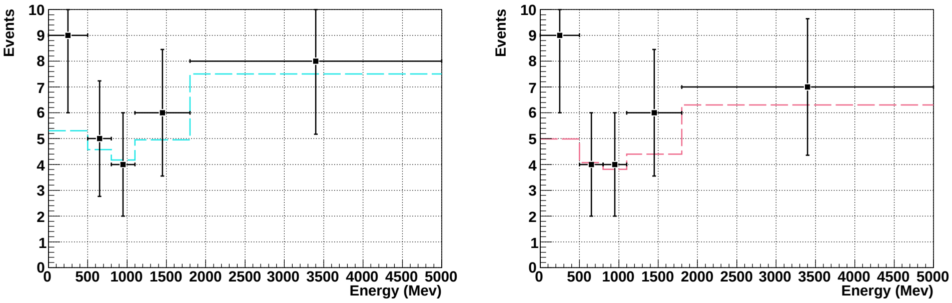

(a) *1Rμ*

(b) *1Rμ01DE*

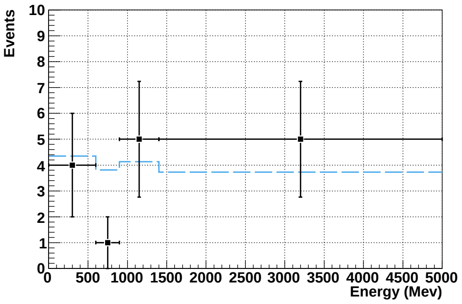

(c) *1Rμ01DEMLP*

Figure 6.13: *Energy spectra binning for the run 1-2 oscillation analysis selections. Plots show MC expectation with a continuous dashed line. Data is overlaid with black markers. Plots are generated with oscillated 10a MC data with run 1-2 normalisation (1.43 × 10^{20} POT).*

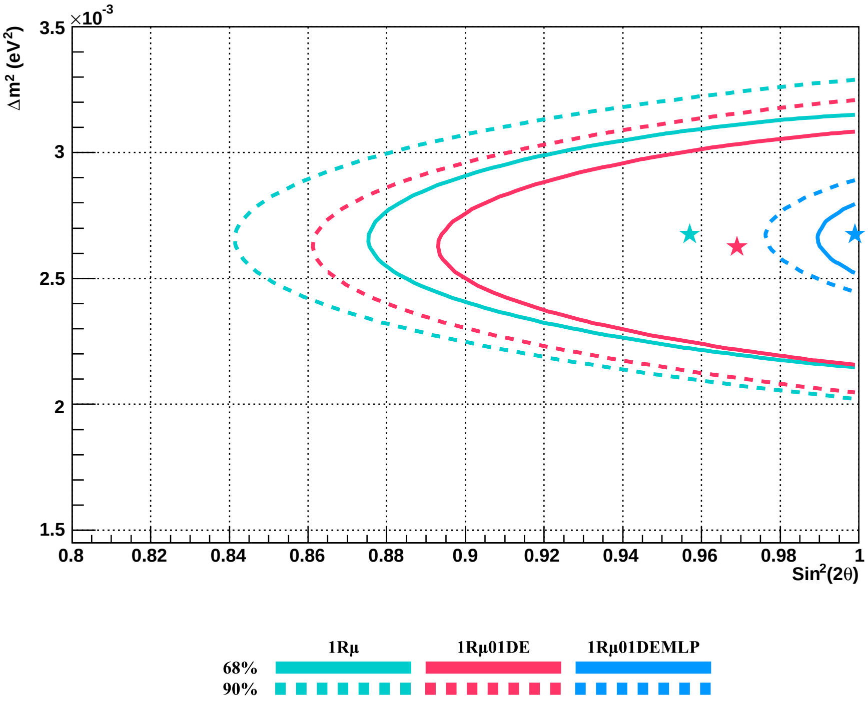

Figure 6.14: *Oscillation parameter best fit and confidence regions for run 1-2 (1.43×10^{20} POT). The stars mark the best fit point for each selection, with the lines marking regions of confidence.*

a likelihood method will remove this issue.

Comparison of these results with the March 2011 MINOS result (figure 2.1) reveals compatibility of the $\sin^2 2\theta_{23}$ 68% confidence regions, while the confidence range of the Δm^2_{32} values are only compatible at the 90% level. However, with the inclusion of all sources of systematic error and the use of a likelihood method the confidence contours of the T2K selections will likely grow and shift.

A full analysis of the run 1-2 data performed by Kameda and Otani for T2K places the best fit point of the 1Rμ01DE selection at $\Delta m^2_{32} = 2.6 \times 10^{-3}\mathrm{eV}^2$ and $\sin^2 2\theta_{23} = 0.99$ (figure 6.15). This is a shift of 0 in Δm^2_{32} and +0.02 in $\sin^2 2\theta_{23}$ when compared to the result measured by this study as listed in table 6.3 [57]. The change in the confidence limits of the measurement is an increase to > 0.85 for $\sin^2 2\theta_{23}$ and a reduction to a range of $(2.1 \rightarrow 3.1) \times 10^{-3}$ eV^2 for Δm^2_{32} at the 90% confidence level. This reduction can however be explained by the use of the Feldman-Cousins method [58] by Kameda and Otani to construct the allowed confidence regions. This method is used to account for the existence of a non-physical parameter space where $\sin^2 2\theta_{23} > 1$. It produces a characteristic taper in the contour close to the $\sin^2 2\theta_{23} = 1$ boundary, which reduces the Δm^2_{32} confidence range.

6.2.1 Further Improvements to the Measurement

This section discusses the main ways in which the measurement is envisaged to be improved as part of its future use by the T2K collaboration.

Of principal importance is a more detailed analysis of the systematic error associated with the MLP cut. The Cholesky decomposition provides a mechanism for accounting for the correlations between the input variables. However, the method described in section 5.4.5 suffers from two weaknesses: firstly that not all the variables have a data to Monte Carlo shape comparison to base their uncertainty on and that secondly the Cholesky decomposition method does not fully account for the nuanced non-linear relationship between the variables. It is possible that these problems have contributed to poorer than expected agreement between data and Monte Carlo prediction for the network output. The solution to these problems is to use Super-Kamiokande atmospheric neutrino

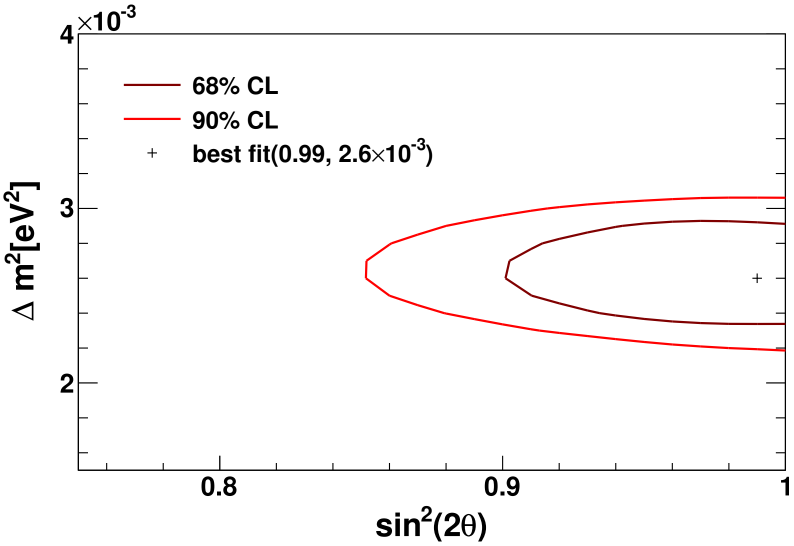

Figure 6.15: *T2K official oscillation parameter best fit and confidence regions for run 1-2 (1.43×10^{20} POT) using a 1Rμ01DE selection. The cross marks the best fit point for the selection, with the lines marking regions of confidence. A Feldman-Cousins method was used make the contours. Plot taken from [57].*

data applying the same selection and re-weighting it to match the T2K energy spectrum. In this case, uncertainty in the variables would not be considered independently, but the difference between Monte Carlo prediction and data of the final response would be used to evaluate the systematic uncertainty on the cut. If the uncertainty is found to be high then the more poorly understood input variables may need to be removed to improve performance. Access to Super-Kamiokande atmospheric data is restricted to Super-Kamiokande collaborators only. An official request is therefore required to use this data for the systematic error evaluation in which work from this study provides the main case.

In terms of the fit between data and Monte Carlo, a few improvements could be made, in particular, replacing the χ^2 method with a likelihood fit and using toy Monte Carlo to generate expected systematic contributions for each point in parameter space. Further systematic uncertainties could also be considered. These are primarily uncertainties in the incoming neutrino flux normalisation and in the energy spectrum shape of the flux as well as a systematic term relating to the energy reconstruction. Measurement of the flux by ND280 could also be incorporated (so far corresponding to a multiplactive factor). Finally, including the anti-muon neutrino beam flux in the Monte Carlo event expectations would create more accurate predictions for the neutrino energy spectrum shape and number of events, improving the fit.

Chapter 7

Conclusions

The study outlined in the preceding chapters has been concerned with evaluating enhancements to the standard muon-neutrino disappearance analysis by looking at alternative and original event selections in an attempt to increase the sensitivity of the analysis to the oscillation parameters Δm^2_{23} and $\sin^2 2\theta_{23}$ for both the short term running of the experiment (runs 1-2) and when considering long term prospects (8.33×10^{21} POT). Two main enhancements were discussed, namely a decay-electron based separation of the energy reconstruction into CCQE-like and CC1π^+-like of the single muon-like ring selection and the use of a neural network to improve the CCQE purity of the zero or one decay electron enhance selection. Out of these it was only the MLP neural network based selection which showed an improvement in performance over the standard selection, particularly in the near term where its aggressive removal of non-CCQE backgrounds drove down the cross-section systematics as well as the detector and reconstruction systematics when compared to its parent zero or one decay electron enhanced sample. In the long term running of the experiment this advantage was expected to decrease as ND280 provides better cross-section measurements and the extra systematic term coming from the MLP cut becomes more important. When run 1-2 data was used to test the performance of the MLP selection it was found that agreement with Monte Carlo prediction was poorer than expected. The MLP approach will therefore need further evaluation before it can be considered for official use within the T2K collaboration.

The two decay-electron sample, although showing potential with its energy resolution and low neutral current background, ultimately could not be used to enhance sensitivity to oscillation in both the near and long term running of the experiment, due primarily to the low cross-section coverage of the critical energy region, its high energy tail, and increased systematic error when compared to the principal sample.

Using the MLP enhanced selection a measurement was made using the first data collected by the T2K experiment. A value of $2.68^{+0.12}_{-0.18} \times 10^{-3}$ eV^2 was measured for Δm^2_{32} and $0.999^{+0.001}_{-0.009}$ for $\sin^2 2\theta_{23}$ including Super-Kamiokande systematic and cross-section errors . A measurement was also made using the standard zero or one decay-electron enhanced selection resulting in a value of $2.63^{+0.42}_{-0.43} \times 10^{-3}$ eV^2 for Δm^2_{32} and $0.969^{+0.031}_{-0.075}$ for $\sin^2 2\theta_{23}$. This analysis was presented to the collaboration in an internal T2K technical note [56].

Bibliography

[1] W. Pauli. Pauli letter collection letter to Lise Meitner. Available from the CERN Document Server `http://cdsweb.cern.ch/record/83282`, 1930.

[2] E. Fermi. *Z. Phys*, 88:161, 1934. In German.

[3] H. Bethe and R. Peierls. The neutrino. *Nature*, 133:532, 689–690, 1934.

[4] F.Reines and C. Cowan. The neutrino. *Nature*, 178:446, 1956.

[5] M. Goldhaber and L. Grodzins. Helicity of neutrinos. *Phys. Rev.*, 109:1015, 1958.

[6] G. Danby et al. Observation of high-energy neutrino reactions and the existence of two kinds of neutrinos. *Phys. Rev. Lett.*, 9:36, 1962.

[7] M. Perl et al. Evidence for anomalous lepton production in e^+-e^- annihilation. *Phys. Rev. Lett.*, 35:1489, 1975.

[8] K. Kodama et al. Observation of tau neutrino interactions. *Phys. Lett. B*, 504:218, 2001.

[9] F. Reines et al. Evidence for high-energy cosmic-ray neutrino interactions. *Phys. Rev. Lett.*, 15:429–433, Aug. 1965.

[10] R. Davis, D. S. Harmer, and K. C. Hoffman. *Phys. Rev. Lett.*, 20:1205, 1968.

[11] SAGE Collaboration: A. I. Abazov et al. *Phys. Rev. Lett.*, 67:3332, 1991.

[12] GALLEX Collaboration: P. Anselmann et al. *Phys. Lett.*, B285:376, 1992.

[13] Kamiokande-II Collaboration: K. S. Hirata et al. *Phys. Rev. Lett.*, 63:16, 1989.

[14] Kamiokande-II Collaboration: K. S. Hirata et al. *Phys. Lett.*, B205:416, 1988.

[15] IMB Collaboration: T. J. Haines et al. *Phys. Rev. Lett.*, 57:1986–1989, Oct. 1986.

[16] SNO Collaboration: Q. R. Ahmad et al. *Phys. Rev. Lett.*, 87:071301, 2001. nucl-ex/0106015.

[17] Super-Kamiokande Collaboration: S. Fukuda et al. *Phys. Rev. Lett.*, 86:5651, 2001. hep-ex/0103032.

[18] Z. Maki, M. Nakagawa, and S. Sakata. Remarks on the unified model of elementary particles. *Progress of Theoretical Physics*, 28:870, 1962.

[19] S. P. Mikheev and A. Y. Smirnov. *Sov. J. Nucl. Phys.*, 42:913, 1985.

[20] L. Wolfenstein. *Phys. Rev.*, D17:2369, 1978.

[21] KamLAND Collaboration: K. Eguchi et al. Evidence for reactor antineutrino disappearance. *Phys. Rev. Lett.*, 90:021802, 2003.

[22] MINOS Collaboration: P. Adamson et al. Measurement of neutrino oscillations with the minos detectors in the numi beam. *Phys. Rev. Lett.*, 101:131802. arXiv:0806.2237v1.

[23] KATRIN Collaboration. Katrin: A next generation tritium beta decay experiment with sub-ev sensitivity for the electron neutrino mass. 2001. arXiv.org:hep-ex/0109033.

[24] K. Zuber. Neutrinoless double beta decay experiments. 2006. nucl-ex/0610007.

[25] T. Kato. *Tau Neutrino Appearance via Neutrino Oscillations in Atmospheric Neutrinos.* PhD thesis, Stony Brook University, 2007.

[26] B. Pontecorvo. *Sov. Phys. JETP*, 26:984–988, 1968.

[27] L.-L. Chau and W.-Y Keung. *Phys. Rev. Lett.*, 53:1802, 1984.

[28] J. Rich. Quantum mechanics of neutrino oscillations. *Phys. Rev. D*, 48:4318–4325, Nov 1993.

[29] B. Kayser. On the quantum mechanics of neutrino oscillation. *Phys. Rev. D*, 24:110–116, Jul 1981.

[30] T. Schwetz et al. Three-flavour neutrino oscillation update. *New J. Phys.*, 10:113011, 2008. arXiv.org:hep-ph/0808.2016v3.

[31] P. Adamson et al. Measurement of the neutrino mass splitting and flavor mixing by minos. *Phys. Rev. Lett.*, 106:181801, May 2011.

[32] K. Abe et al. The T2K experiment. *Nuclear Instruments and Methods in Physics Research Section A: Accelerators, Spectrometers, Detectors and Associated Equipment*, In Press, Corrected Proof:–, 2011.

[33] T2K Collaboration. T2K ND280 Conceptual Design Report. T2K Internal Document, Nov 2005.

[34] Hamamatsu Photonics. MPPC Multi Pixel Photon Counter. `http://sales.hamamatsu.com/assets/pdf/parts_S/mppc_kapd0002e08.pdf`, 2010.

[35] The Super-Kamiokande Collaboration: S. Fukuda et al. The Super-Kamiokande detector. *Nucl. Inst. Meth.*, A501:418–462, 2003.

[36] CERN Application Software Group. Geant3. `http://wwwasd.web.cern.ch/wwwasd/geant/index.html`, 1993.

[37] G. Battistoni et al. Fluka: a multi-particle transport code. In M. Albrow and R. Raja, editors, *Proceedings of the Hadronic Shower Simulation Workshop*, Fermilab, 2006.

[38] N. Abgrall. Report from the NA61/SHINE experiment at the CERN SPS. Technical Report CERN-SPSC-2010-025. SPSC-SR-066, CERN, Geneva, Sep 2010.

[39] Y. Hayato. NEUT. *Nucl.Phys.Proc.Suppl.*, 112:171–176, 2002.

[40] C. Zeitnitz and T.A. Gabriel. The GEANT - CALOR interface and benchmark calculations of ZEUS test calorimeters. *Nucl.Instrum.Meth.*, A349:106–111, 1994.

[41] J. Albert and R. Terri. Super-Kamiokande 10a and 07a Event Expectation Calculations. Technical Report TN-012, T2K, July 2010.

[42] S. Nakayama. T2K ν_e event selection at Super-Kamiokande using the RUN1+RUN2 data. Technical Report TN-055, T2K, May 2011.

[43] K. Iyogi et al. T2K data acquisition and FC event selection at Super-Kamiokande. Technical Report TN-027, T2K, February 2011.

[44] P.V.C. Hough. Machine analysis of bubble-chamber pictures. In *Proceedings of the International Conference of High Energy Accelerators and Instrumentation*, 1959.

[45] R.O. Duda and P.E. Hart. Use of the hough transformation to detect lines and curves in pictures. *Comm. ACM*, 15:11–15, 1972.

[46] T. Barszczak. TScan - Trivial Scanner. `http://www.ps.uci.edu/~tomba/sk/tscan/`, 1999.

[47] M. H. Ahn et al. Measurement of neutrino oscillation by the k2k experiment. *Phys. Rev. D*, 74:072003, Oct 2006.

[48] J. Kameda and R. Wendell. Study on Super-K events and systematic errors relevant for the ν_μ disappearance analysis with T2K 3.23×10^{19} POT data. Technical Report TN-034, T2K, December 2010.

[49] M. Otani and J. Kameda. Super-K events and Updated systematic errors for ν_μ disappearance analysis with T2K 1.431×10^{20} POT. Technical Report TN-065, T2K, July 2011.

[50] P. Perio et al. NEUT systematic studies for 2010a analysis. Technical Report TN-032, T2K, January 2011.

[51] M. Besnier. The contribution of Near Detectors to the T2K neutrino measurements. In *Topics in Astroparticle and Underground Physics (TAUP 2009)*, Rome, Italy, July 2009.

[52] A. Hoecker et al. TMVA - Toolkit for Multivariate Data Analysis. *ArXiv Physics e-prints*, March 2007. arXiv:physics/0703039v5.

[53] W. H. Press et al. *Numerical Recipes: The art of scientific computing*, pages 100–102. Cambridge University Press, 3rd edition, 2007.

[54] Y. Obayashi. Status of Super-Kamiokande and early atmospheric neutrino data from SK-IV. In *Proceedings of the 31st ICRC*, LODZ, 2009.

[55] K. Abe et al. Indication of electron neutrino appearance from an accelerator-produced off-axis muon neutrino beam. *Phys. Rev. Lett.*, 107:041801, Jul 2011.

[56] A. Hyndman et al. MVA selection of ν_μ events at Super-Kamiokande. Technical Report TN-083, T2K, September 2011.

[57] J. Kameda and M. Otani. Muon neutrino disappearance analysis with T2K 1.431×10^{20} POT data. Technical Report TN-067, T2K, July 2011.

[58] G. Feldman and R. Cousins. Unified approach to the classical statistical analysis of small signals. *Phys. Rev. D*, 57:3873–3889, Apr 1998.